Theoretical and Computational Generalizations of Magnetic Nanoparticle Hyperthermia Including Optimization, Control, and Aggregation

Caleb Maxwell Koch

Thesis submitted to the faculty of the Virginia Polytechnic Institute and State University in partial fulfillment of the requirements for the degree of

Master of Science
In
Engineering Mechanics

Leigh Winfrey, Chair
Carla V. Finkielstein
Raffaella De Vita

2014 June 30th

Blacksburg, VA

Keywords: Hyperthermia, Nanoparticles, Aggregation Theory

Theoretical and Computational Generalizations of Magnetic Nanoparticle Hyperthermia Including Optimization, Control, and Aggregation

Caleb Maxwell Koch

ABSTRACT

Iron Oxide Nanoparticles (IONPs) are a multifunctional nano-material that allows for MRI imaging, intravenous-controlled drug movement, and hyperthermia. The objective of this study is to optimize and control IONP hyperthermia and cope with aggregation using Finite Element (FE) Modeling and statistical physics.

The FE model is first used to demonstrate the advantages of changing IONP heat dissipation in time, which can increase energy density inside tumors while decreasing the energy delivered in healthy tissue. Here, this is defined as target-specificity. Second, this model is used to demonstrate that time-dependent IONP heat dissipation allows for control of temperature distributions inside the body. Third, the FE model is used to solve the temperature distributions resulting from capillary diffusion of IONPs. This study shows that capillary diffusion combined with direct injection results in improved homogeneity of temperature distributions. Fourth, using a square-difference scheme, non-time domain parameters including the number of IONP injections, the location of injections, IONP distribution width, and heating intensity are optimized to improve target-specificity and temperature homogeneity. Collectively, this study contributes to hyperthermia by optimizing time- and non-time- domain parameters, controlling hyperthermia, and quantifying aggregation with a new theory.

ACKNOWLEDGEMENTS

I would like to express my fullest gratitude to my advisor, Dr. Leigh Winfrey. Thank you for believing in me and helping me believe in myself. I will cherish the lessons you taught me and look forward to passing them to my own students someday. Thank you to Dr. De Vita and Dr. Finkielstein for supporting my studies and challenging me to think deeper. Thank you to my Father and Mother for loving me and supporting me through my best and worst times. Thank you to my four younger siblings, Ari, Ethan, Grant, and Carlson for being an inspiration. Without you all I would not be where I am today. Lastly, thank you God for the strength and confidence to finish, saving me personally, and showing me the only thing worth striving toward.

ATTRIBUTION

Several colleagues aided in the writing and research behind several of my chapters presented as part of this thesis. Another colleague also aided with data collection in several chapters. A brief description of their contributions is included here.

Chapter 3: FEM Optimization of Energy Density in Tumor Hyperthermia using Time-Dependent Magnetic Nanoparticle Power Dissipation

Chapter 3 was published in IEEE Transactions on Magnetics.

Chapter 4: FEM Analysis of Controlling Hyperthermia States using Magnetically Induced Iron Oxide Nanoparticle Heat Dissipation

Chapter 4 was submitted to IEEE Transactions on Magnetics for review.

Chapter 5: FEM Analysis of Magnetic Nanoparticle Hyperthermia Resulting from Intravenous Diffusion and Radial-Modal Distributions

Chapter 5 is in preparation for submission to IEEE Transactions on Magnetics.

Chapter 6: Improving Nanoparticle Hyperthermia by Optimizing Location, Number of Injection Sites, Heating Intensity, and Heating Distribution; Computational Study

Chapter 6 was submitted to International Journal for Hyperthermia for review.

Chapter 7: Theoretical Analysis of Magnetically Induced Iron Oxide Hyperthermia and Variability due to Aggregation

Chapter 7 is in preparation for submission to the International Journal for Hyperthermia.

Leigh Winfrey, PhD, Virginia Tech Plasma Science Lab, is currently a professor in Nuclear Engineering at Virginia Tech. Dr. Winfrey greatly is a co-author on Chapters 3-7 and greatly helped in the concept phase of each project, and revising the completed work.

Abigail Casey, PhD candidate, Virginia Tech Plasma Science Lab, is currently a PhD candidate in Material Science and Engineering at Virginia Tech. Ms. Casey is a co-author for Chapters 4, 5, and 7, conducted data collection for Chapters 4-5, and contributed to the thought development of Chapter 7.

TABLE OF CONTENTS

LIST OF FIGURES

LIST OF TABLES

Chapter 1: Introduction

Koch, Caleb[1]

[1]Engineering Science and Mechanics, Virginia Tech, Blacksburg, VA 24061

Corresponding Author Email: caleb.koch@vt.edu

Iron Oxide Nanoparticles (IONP) and their multi-functionality have progressed the field of medicine in several ways. The first application IONPs were used for was imaging. By externally applying an approximately 3 Tesla and a 1-3MHz alternating magnetic field IONPs relax the oscillatory magnetic-moment energy in the form of light. Researchers have built detectors to capture this light, and coined this technology as MRI. In the field of medicine, MRI is used routinely to take non-invasive yet *in vivo* images of internal tissues [1, 2]. Secondly, IONPs function in the traditional manner, i.e. we think about iron being attracted to static magnetic fields. In the same way scientists have conjugated IONPs to chemotherapeutics and used static magnetic fields to increase its accumulation in the tumor [3, 4].

The third application, the particular application of interest for this study, is using IONPs to induce tumor hyperthermia. Decreasing the MRI magnetic fields to about 0.2 Tesla and 500kHz alternating results in the relaxation energy being released in the form of heat rather than light, a process also known as Néel relaxation [5, 6]. Scientists have worked for the past 30 years to fine-tune this heat release mechanism to achieve target-specific cancer treatments.

Studying IONP hyperthermia reaches farther than simply heat treatments. Rather, scientists have found ways of using target-specific heat dosage to increase chemotherapeutic efficacy. As early as 1978 Yatvin and et al. [7] introduced the idea of liposomes with the prospects of temperature-mediated drug release. More recently, McDaniel et al. in 2014 [8] at Duke University published a fabrication method for an elastic like polypeptide coating that would release its drug contents depending on the therapeutic temperature range, 42-43°C. Hayashi and et al. also in 2014 [9] published a

study where they used a nanoparticle construct of IONPs conjugated to doxorubicin all coated with a temperature sensitive polymeric coating. At 44°C, the coating would undergo a glass-transition, degrade, and release its chemical contents. Xu and Neckers [10] used IONP hyperthermia to increase Heat-Shock Protein expression in the tumor area and targeted that protein to increase drug selectivity. Studying the thermodynamics of IONP hyperthermia reaches farther than a heat treatment for cancer, rather it cut across cross-disciplines from medicine, to chemistry, to engineering theory.

Computer simulations offer many advantages investigating the viability of IONP hyperthermia. In computer models, medical experiments can be simulated that otherwise would not be experimentally feasible because of time, finances, or regulatory restrictions. Furthermore, computer models help guide experiments and there is synergy in combining the two research methods.

Several studies in the past 10 years have published methods of effectively combining computational modelling and experiments. Xu and et al. in 2009 [11] directly injected IONPs into the tumor then used MRI imaging to determine local IONP densities. Next, the imaging data was uploaded into a program that subsequently determined the heating inside resulting from the *in vivo* IONP distribution. Other researchers have used similar methods to link modeling and experiments [12].

For correctly modeling the thermodynamics of IONP hyperthermia, important steps have been taken in the past 10 years. Hergt and Andra [6] outlined the physical limits of IONPs and optimized parameters such as particle diameter and concentration. Solloum and et al. in 2008 [13] analyzed the IONP distribution for different injection rates. He confirmed that with slow injection rates a spherical Gaussian distribution was

achievable, which has been a foundational assumption for modeling IONP hyperthermia. In the same year Solloum [14] published details of how the blood perfusion cooling rate is dependent on its local temperature; as IONP heating intensity increases the blood perfusion cooling increases and Candeo and Dughiero later in 2009 [12] modeled the implications of this non-linearity. This is important for accurately simulating the thermodynamics of tissue.

Even with recent large strides in modeling the thermodynamics of IONP hyperthermia, many challenges still remain in exploring its full potential. For example, in all models of IONP hyperthermia only constant heat dissipation is considered [11, 12]. This sets up the foundation for Chapter 3 of this work. Chapter 3 observes the consequences of time-varying heat dissipation. More importantly, this study explains how time-varying heat dissipation schemes can be used to increase hyperthermia target-specificity. It begins with the premise that thermodynamics is a non-linear process which it then follows that a nonlinear scheme would result in different temperature results for each variable non-linear application of energy. The study looks at three parameters involved in designing heat dissipation time schemes: maximum intensity, order of maximum intensity, and duration of maximum intensity, and how these three parameters should be organized to achieve increased target-specificity.

Hyperthermia maturing as a discipline is leading researchers to ask more advanced questions, moving from how to achieve desired temperature profiles to how to control the temperature profile through time. Target-specificity can be achieved. Scientists want to develop more complex ways of controlling the temperature inside the body. Lupu [15] in 2014 published a method for constructing complex IONPs with low

curie temperatures (the heat needed to degauss a magnetic system thermally) which means that as the tumor approached the therapeutic temperature of 43C, the less heat was dissipated by the nanoparticles. Astefanoaei [16] quickly followed Lupu's report with a computational study of the details of using this type of IONP, and found the center of the tumor was still an area of concern in reaching therapeutic range temperatures. However, even with the new method of controlling hyperthermia temperature profiles, there is still concern regarding the toxicity of this new IONP construct. Chapter 4 takes a step back and posits that rather than using the IONPs to control temperature profiles, the magnetic fields can be used to control temperature profiles in the therapeutic range. The time to reach the therapeutic range is observed, and defined by a regression line. This gives doctors a method to optimize treatment times. Next, knowing tissue response to heating intensities allows one to "freeze" an optimal hyperthermia temperature profile through time. From Chapter 3 and 4 one may understand how magnetic field which control heat dissipation of IONPs can be used to both optimize and control hyperthermia.

All simulations thus far assume a Gaussian IONP distribution derived from direct injection. However, Wong and et al. [17] studied IONP diffusion from capillaries that ran along the boundary between tumorous and healthy tissue. Wong found that diffusion from the capillary resulted in an error complimentary function with the peak at the boundary and the tail toward the tumor. However, in a real system, IONPs leak on both the tumor and healthy tissue side. Chapter 5 explores the type of temperature profiles that result in IONP diffusion from a boundary capillary. Furthermore, this study discusses the feasibility of capillary diffusion hyperthermia and how this can be used synergistically with direct injection.

Time-dependent parameters in IONP heat dissipation are not the only parameters that can be optimized. Bagaria & Johnson in 2005 attempted to optimize several non-time domain parameters including the number of injections, the location of injections, the distribution spread of each injection, and the IONP heating intensity. However, as Solloum critiqued in 2009 [18], the study made several broad assumptions. First Bagaria & Johnson in 2005 [19] assumed an IONP direct injection would result in a quadratic decaying heating function, when other studies suggest otherwise. Solloum [18] attempted his own optimization scheme, also with limitations. Only irregularly shaped tumors were considered, and the results were not generalized around arbitrary tumor shapes. Solloum assumed the optimal number of injection sites that worked with his irregularly shaped tumors as opposed to deducing the optimal number. Additionally, he did not explicate the interdependencies between each of the four parameters. Here, Chapter 6 addresses the shortcomings of the previous studies by relating the four parameters to tumor shape classifications and determining the interdependencies between all parameters. This study also determines what the optimal conditions for improving target-specificity and temperature homogeneity.

One of the natural yet difficult problems to deal with in IONP hyperthermia is aggregation. Magnetic fields of opposite polarity attract. Each IONP is a single magnetic dipole domain. From stochastic thermal perturbations these single domains from local IONPs will fluctuate in a manner that results in IONPs becoming attracted to each other which leads to aggregating. Nanoparticles that were originally 2nm can build into aggregates of diameters from 20nm to 3microns [20]. In order to cope with this problem chemists have designed IONP fabrication methods to coat iron oxide with polymeric

coatings to keep magnetic domains from getting too close and aggregating. Chan in 1993 [21] used lengthy polymer chains to keep IONPs from aggregating. However, he observed that any deficiencies resulted in aggregation, given that aggregates have intensified magnetic field attractions, which enhances the problem. More recently, Yallup and et al. [22] were interested in reducing the effects of aggregation. After IONPs were constructed they put them under hyperthermia conditions, allowed IONPs to aggregate, then centrifuged them to get the larger aggregates out, and siphoned off the good IONPs. Even by undergoing that process the system aggregation still occurred.

The IONP construct is not the only variable in aggregation. Lundqvist in 2008 [23] and Safi in 2010 [24] noticed that when citric acid molecules and poly(acrytic acid) polymer coatings around iron oxide and cerium oxide nanoparticles when serum proteins was present aggregation occurred tenfold from the original hydrodynamic diameter.

Recently, Sadhukha in 2014 [25] studied what resulted if aggregation could be used despite the inhomogeneous temperature distributions. They were not able to quantify the unpredictability aggregation introduced to the system and proceeded with the hyperthermia treatment. Chapter 7 tackles the problem of aggregation by building a theoretical framework for how to understand it. From this this theoretical framework, details are provided for the amount of variability aggregation introduces into the hyperthermia system.

References

[1] J. Bulte and D. Kraitchman, "Iron Oxide MR Contrast Agents for Molecular and Cellular Imaging.," *NMR in Biomedicine,* vol. 17, 2004.

[2] R. Weissleder, A. Bogdanov, E. Neuwelt and M. Papisov, "Long-Circulating Iron Oxides for MR Imaging," *Advanced Drug Delivery Reviews,* vol. 16, no. 2, pp. 321-334, 1995.

[3] T. Yoon, J. Kim, B. Kim, K. Yu, M. Cho and J. Lee, "Multifunctional Nanoparticles Possessing a "Magnetic Motor Effect" for Drug or Gene Delivery," *Angewandte Chemie,* vol. 117, no. 7, pp. 1092-1095, 2005.

[4] V. Kalambur, B. Han, B. Hammer, T. Shield and J. Bischof, "In vitro characterization of movement, heating, and visualization of magnetic nanoparticles for biomedical applications," *Nanotechnology,* vol. 16, no. 1221, 2005.

[5] R. Hergt, S. Dutz and M. Zeisberger, "Validity limits of the Neel relaxation model of magnetic nanoparticles for hyperthermia," *Nanotechnology,* vol. 21, no. 1, 2010.

[6] R. Hergt and W. Andra, "Physical Limits of Hyperthermia using Magnetic Fine Nanoparticles," *IEEE Transactions on Magnetics,* vol. 34, no. 5, pp. 3745-3754, 1998.

[7] M. Yatvin, J. Weinstein, W. Dennis and R. Blumenthal, "Design of Liopsomes for Enhanced Local Release of Drugs by Hyperthermia," vol. 202, pp. 1290-1293, 1978.

[8] J. McDaniel, S. MacEwan, X. Li, D. Radford, C. Landon, M. Dewhirst and A. Chilkoti, "Rational Design of "Heat Seeking" Drug Loaded Polypeptide Nanoparticles That Thermally Target Solid Tumors," *NanoLetters,* vol. 14, pp. 2890-2895, 2014.

[9] K. Hayashi, M. Nakamura, H. Miki, S. Ozaki, M. Abe, T. Matsumoto, T. Sakamoto, T. Yogo and K. Ishimura, "Magnetically Responsive Smart Nanoparticles for Cancer Treatment with a Combination of Magnetic Hyperthermia and Remote-Control Drug Release," *Theranostics,* vol. 4, no. 8, pp. 834-844, 2014.

[10] W. Xu and L. Neckers, "Targeting the Molecular Chaperone Heat Shock Protein 90 Provides a Multifaceted Effect on Diverse Cell Signaling Pathways of Cancer Cells," *Clinical Cancer Research,* vol. 13, no. 6, pp. 1625-1629, 2007.

[11] R. Xu, H. Yu, Y. Zhang, M. Ma, Z. Chen, C. Wang, G. Teng, J. Ma, X. Sun and N. Gu, "Three-Dimensional Model for Determining Inhomogeneous Thermal Dosage in a Liver Tumor During Arterial Embolization Hyperthermia Incorporating Magnetic Nanoparticles," *IEEE Transactions on Magnetics,* vol. 45, no. 8, 2009.

[12] A. Candeo and F. Dughiero, "Numerical FEM Models for the Planning of Magnetic Induction Hyperthermia Treatments with Nanoparticles," *IEEE Transactions on Magnetics,* vol. 45, no. 3, 2009.

[13] M. Salloum, R. Ma, D. Weeks and L. Zhu, "Controlling nanoparticle delivery in hyperthermia for cancer treatment: Experimental study in agarose gel," *International Journal of Hyperthermia,* vol. 24, no. 4, pp. 337-345, 2008.

[14] M. Salloum, M. R. and L. Zhu, "An in-vivo experimental study of temperature elevations in animal tissue during magnetic nanoparticle hyperthermia,"

International Journal of Hyperthermia, vol. 24, no. 7, pp. 589-601, 2008.

[15] N. Lupu, I. R. Nat. Inst. of R&D for Tech. Phys., H. Chiriac, S. Corodeanu and G. Ababei, "Development of Fe-Nb-Cr-B Glassy Alloys with Low Curie Temperature and Enhanced Soft Magnetic Properties," *IEEE Transactions on Magnetics,* vol. 47, no. 10, pp. 3791-3794, 2011.

[16] I. Astefanoaei, I. Dumitru, H. Chiriac and A. Stancu, "Controlling Temperature in Magnetic Hyperthermia with Low Curie Temperature Particles," *Journal of Applied Physics,* p. 115, 2014.

[17] C. Wong, T. Stylianopoulos, J. Cui, J. Martin, V. Chauhan, W. Jiang, Z. Popovic, R. Jain, M. Bawendi and D. Fukumura, "Multistage nanoparticle delivery system for deep penetration into tumor tissue," *PNAS,* vol. 108, no. 6, pp. 2426-2431, 2011.

[18] M. Salloum, R. Ma and L. Zhu, "Enhancement in treatment planning for magnetic nanoparticle hyperthermia: Optimization of the heat absorption patter," *International Journal of Hyperthermia,* vol. 25, no. 4, pp. 309-321, 2009.

[19] H. Bagaria and D. Johnson, "Transient solution to the bioheat equation and optimization for magnetic fluid hyperthermia treatment," *International Journal of Hyperthermia,* vol. 21, no. 1, pp. 57-75, 2005.

[20] M. Baalousha, "Aggregation and disaggregation of iron oxide nanoparticles: Influence of particle concentration, ph and natural organic matter," *Science of the Total Environment,* vol. 407, no. 6, pp. 2093-2101, 2009.

[21] D. Chan, D. Kirpotin and P. Bunn, "Synthesis and evaluation of colloidal magnetic iron oxides for the site-specific radiofrequency-induced hyperthermia of cancer," *Journal of Magnetism and Magnetic Materials,* vol. 122, pp. 374-378, 1993.

[22] M. Yallapu, S. Othman, E. Curtis, G. Gupta, M. Jaggi and S. Chauhan, "Multi-functional magnetic nanoparticles for magnetic resonance imaging and cancer therapy," *Biomaterials,* vol. 32, pp. 1890-1905, 2011.

[23] M. Lundqvist, J. Stigler, G. Elia, I. Lynch, T. Cedervall and K. Dawson, "Nanoparticle Size and Surface Properties Determine the Protein Corona with Possible Implications for Biological Impacts," *PNAS,* vol. 105, no. 38, pp. 14265-14270, 2008.

[24] M. Safi, H. Sarrouj, N. Mignet and J. Berret, "Interactions between sub- 10- nm Iron and Cerium Oxide Nanoparticles and 3T3 Fibroblasts: the Role of the Coating and Aggregation State," *Nanotechnology,* vol. 21, 2010.

[25] T. Sadhukha, T. Wiedmann and J. Panyam, "Enhancing Therapeutic Efficacy through Designed Aggregation of Nanoparticles," *Biomaterials,* vol. 35, pp. 7860-7869, 2014.

[26] N. Siauve, L. Nicolas, C. Vollaire and C. Marchal, "Optimization of the Sources in Local Hyperthermia using a Combined Finite Element-Genetic Algorithm Method," *International Journal of Hyperthermia,* vol. 20, no. 8, pp. 815-833, 2004.

[27] M. Latorre and C. Rinaldi, "Hyperthermia, Applications of Magnetic Nanoparticles in Medicine: Magnetic Fluid," *Puerto Health Sciences Journal,* vol. 28, no. 3, 2009.

[28] U. Tromsdorf, N. Bigall, M. Kaul, O. Bruns, M. Nikolic, B. Mollwitz, R. Sperling, R. Reimer, H. Hohenberg, W. Parak, S. Forster, U. Beisiegel, A. G. and H. Weller,

"Size and Surface Effects on the MRI Relaxivity of Manganese Ferrite Nanoparticle Contrast Agents," *NanoLetters,* vol. 7, no. 8, pp. 2422-2427, 2007.

[29] F. Sonvico, S. Mornet, S. Vasseur, C. Dubernet, D. Jaillard, J. Degrouard, J. Hoebeke, E. Duguet, P. Colombo and P. Couvreur, "Folate-Conjugated Iron Oxide Nanoparticles for Solid Tumor Targeting Potential Specific Magnetic Hyperthermia Mediators: Synthesis, Physicochemical Characterization, and in Vitro Experiments," *Bioconjugate Chemistry,* vol. 16, no. 5, pp. 1181-1188, 2005.

[30] R. Hergt, R. Hiergeist, M. Zeisberger, G. Glockl, W. Weitschies, L. Ramirez, I. Hilger and W. Kaiser, "Enhancement of AC-losses of magnetic nanoparticles for heating applications," *Journal of Magnetic Materials,* vol. 280, pp. 358-368, 2004.

Chapter 2: Derivation of the Finite Element (FE) Model Implemented to Solve Thermodynamic Equations

Koch, Caleb[1]

[1]Engineering Science and Mechanics, Virginia Tech, Blacksburg, VA 24061

Corresponding Author Email: caleb.koch@vt.edu

Table 1: List of terms used during derivation of FE model.

$T =$	Temperature ($°C$)
$T_0 =$	Initial temperature ($°C$)
$t =$	Time (s)
$\vec{x} =$	Simulation space coordinates (m)
$\theta =$	Normalized temperature ($°C$)
$\nabla =$	Del Operator ($1/m$)
$\omega =$	Weight function
$\partial =$	Partial derivative
$c_b =$	Specific heat of blood ($J/\text{kg}\,°C$)
$W_b =$	Blood perfusion rate (kg/m^3)
$k =$	Thermal conductivity of tissue ($W/m\,°C$)
$\alpha =$	Thermal Constant, $k/\rho\, c$
$c =$	Specific heat of tissue ($J/\text{kg}\,°C$)
$\rho =$	Density of tissue (kg/m^3)
$\beta =$	Convective coefficient
$H_{\text{NP}} =$	Heating due to nanoparticles (W/m^2)
$\Phi =$	Domain of entire simulation space
$\Omega =$	Domain of individual elements
$\Gamma =$	Boundary of individual elements
$e =$	e^{th} element
$R =$	Number of nodes in simulation domain

I. From Penne's Bioheat Equation to Weak Form

This section outlines the Finite Element (FE) Model that was used to solve the thermodynamic equations that describe heat transfer inside human tissue. This model began with the Penne's Bioheat equation [1], as shown below in

(1). This equation has been widely used in studying thermodynamic inside the human body, and though some variations have been introduced, the original form suite the purposes of this study.

$$\frac{1}{\alpha}\frac{\partial}{\partial t}T\left(\vec{x},t\right)-\nabla^2 T\left(\vec{x},t\right)+\frac{c_b W_b}{k}T\left(\vec{x},t\right)=H_{\mathrm{NP}}\left(\vec{x},t\right) \tag{1}$$

The added term to this equation is $H_{\mathrm{NP}}\left(\vec{x},t\right)$, which is heating due to nanoparticles. To begin the derivation of the FE scheme multiply

(1) by a weight function and integrate the entire equation over the domain of the simulation space, which produces (2).

$$\int_{\Phi}\omega\left(\frac{1}{\alpha}\frac{\partial T}{\partial t}+\nabla^2 T+\frac{c_b W_b}{k}T-H_{\mathrm{NP}}\right)dx\,dy=0 \tag{2}$$

At this point the weight function is left arbitrary, but will be specified later. The next step in the development of the FE scheme is arguing that the above expression, (2), holds not only for the entire simulation space but also the domain of discretized subspaces. Thus, consider a discretized domain into N subspaces such that the addition of all the subspaces results in an equivalent simulation space, Φ. This is pictorially demonstrated below in Fig. 1. In this figure, the temperature is the third dimension while *x* and *y* are the spatial dimensions.

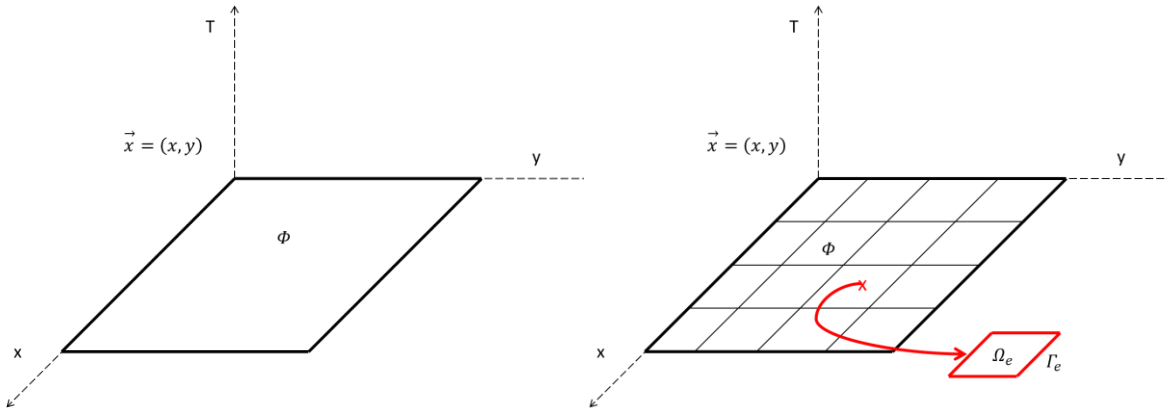

(a) (b)

Fig. 1. Demonstration of discretization process for FE modeling. (a) Simulation domain before discretization. (b) Domain after discretization, and an element extracted to demonstrate its elemental domain and boundary.

Equation (2) is changed so that it represents e^{th} equations for each subspace. Each equation is also integrated over its own e^{th} domain, defined here as Ω_e. The result is shown below in (3).

$$\int_{\Omega_e} \omega_e \left(\frac{1}{\alpha} \frac{\partial T}{\partial t} + \nabla^2 T + \frac{c_b W_b}{k} T - H_{\text{NP}} \right) dx\, dy = 0 \tag{3}$$

The above equation, (3), represents e equations for each element subspace. Next integrate the term $\omega_e \nabla^2 T$ by parts to explore terms that are buried inside (3), which results in (4).

$$\int_{\Omega_e} \left(\omega_e \left(\frac{1}{\alpha} \frac{\partial T}{\partial t} - H_{\text{NP}} \right) + \nabla \omega_e \cdot \nabla T + \frac{c_b W_b}{k} T \right) dx\, dy - \oint_{\Gamma_e} \omega_e \left(\vec{n} \cdot \nabla T \right) ds = 0 \tag{4}$$

The first integral term, which integrates over the domain of each element, captures the thermodynamics that happens within the element. This includes the time

change in temperature, $\partial T/\partial t$, the spatial conduction of heat transfer, $\nabla \omega_e \cdot \nabla T$, and the cooling due to blood perfusion, $\frac{c_b W_b}{k} T$. The line integral that integrates over the boundary of the e^{th} element captures the thermodynamic interactions between the e^{th} element and its surroundings. To further understand this term introduce the convective boundary condition equation, shown below in (5).

$$k\left(\vec{n} \cdot \nabla T\right) + \beta(T - T_0) = 0 \tag{5}$$

This equation states that heat will transfer at the boundary in the direction of lowest temperature, both by conduction and convection. This equation is used commonly in thermodynamics of human tissue [1] [2]. Substitute (5) into the boundary integral term of (4) to produce (6).

$$\int_{\Omega_e} \left(\omega_e \left(\frac{1}{\alpha}\frac{\partial T}{\partial t} - H_{\text{NP}}\right) + \nabla \omega_e \cdot \nabla T + \frac{c_b W_b}{k} T\right) dx\, dy + \oint_{\Gamma_e} \omega_e(\beta(T - T_0))\, ds = 0 \tag{6}$$

This derived equation is the scaffold that provides the setup for the FE scheme. Up to this point no approximations have been introduces. However, the next step will be introducing approximation functions for $T\left(\vec{x}, t\right)$ and specially selected functions for ω_e that will allow this equation to be solved computationally.

II. Deriving Interpolation Functions

The next step in discussing the FE scheme is introducing interpolation functions. However, it would be first advantageous to provide an approachable discussion that outlines the ideology of the FE model before its details are discussed.

The FE scheme began by discretizing the domain into subspaces that, when totaled, is still representative of the original domain. Next, rather than attempting to solve for the temperature inside the subspaces explicitly, or analytically, we choose polynomial functions that closely resemble, or approximate, the solution for that small region of subspace. The reason this works is the smaller the subspace, or the finer the discretized mesh of the domain, then the more polynomial functions are describing the solution over the entire domain. The more piecewise polynomial functions describing a space, therefore, the more accurate the approximated solution becomes.

As a simple example: how would one go about approximating a circle with only straight lines? With three lines the closes one can get is an equilateral triangle. Adding another line, *i.e.* 4 lines, a square is certainly better at depicting the smooth nature of the circle. The more lines that are included in the approximation the more accurate the circle can be represented. A pictorial demonstration of this example is shown below in Fig. 2. This example shows that an increasingly finer line-mesh is capable of approximating a smooth circle, even though the lines are straight.

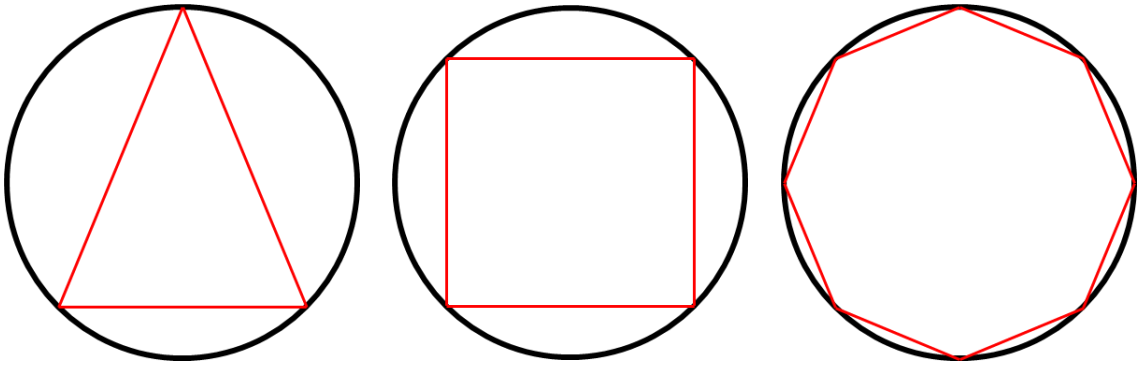

(a) (b) (c)

Fig. 2. Pictorial demonstration of how the FE model works. (a) Circle approximated with only 3 lines. (b) Circle approximated with 4 lines. (c) Circle approximated with more lines. The finer the line-mesh the more accurate the approximation.

An important variation of the above example is important to mention before it is later introduced. Only straight lines are considered in the above example. However, with curved lines, a 3-lines approximation could be formulated to be much more accurate. Curved lines have the advantage of accounting for inner-element variations, in this case the curvature of the circle. Later in this study the phenomenon of aggregation will be discussed, which presents the problem of variations inside elements that cause problems for studying computationally. However, the details will be discussed later.

Next, introduce an approximated form of the solution of $T^e\left(\vec{x},t\right)$, shown below in (7),

$$T^e\left(\vec{x},t\right) \simeq \sum_{j=1}^{M} T_j^e(t)\ \varphi_j^e\left(\vec{x}\right) \tag{7}$$

where M is the number of interpolation functions. The approximated temperature function is a summation of M polynomial functions, $\varphi_j^e\left(\vec{x}\right)$, and their influence on approximated solution varies with time, $T_j^e(t)$. An important assumption is built into (7), namely that the time component of temperature function can be separated from the spatial component of temperature. This assumption is validated with two assumptions from the construct of the initial problem: 1. the nanoparticles do not move during magnetic heating, and 2. no non-linear terms are present in the initial equation,

(1).

The interpolation functions will be selected, however, in a manner that proves advantageous to the development of our FE model. Consider an arbitrary subspace, element, from the domain. Based on this element, assume each of the j^{th} interpolation functions has the property of equaling one at its assigned node and zero at all other nodes. In other words, the function has the following property shown in (8).

$$\varphi_j^e(\vec{x}) = \begin{pmatrix} 1 \ \text{ if } (x_{i=j}, y_{i=j}) \\ 0 \ \text{ if } (x_{i\neq j}, y_{i\neq j}) \end{pmatrix} \tag{8}$$

Thus, the 1^{st} interpolation function equals 1 at the 1^{st} node and zero at all others, and this is true for the other $(M-1)$ nodes. More explicitly, consider a rectangle with dimensions as $\{(\text{length}, \text{width}) = (a,b)\}$. Let the rectangle-element have four nodes, one at each of the vertices. Furthermore, consider a frame of reference that places the 1^{st}

node at the origin. In order for (8) to hold true the four corresponding interpolation functions must equal (9), shown below.

$$\varphi^e\left(\vec{x}\right) = \begin{pmatrix} \varphi_1^e(\bar{x},\bar{y}) = (1-\bar{x}/a)(1-\bar{y}/b) \\ \varphi_2^e(\bar{x},\bar{y}) = (\bar{x}/a)(1-\bar{y}/b) \\ \varphi_3^e(\bar{x},\bar{y}) = (\bar{x}/a)(\bar{y}/b) \\ \varphi_4^e(\bar{x},\bar{y}) = (1-\bar{x}/a)(\bar{y}/b) \end{pmatrix} \tag{9}$$

Two functions from (9) are selected and plotted in Fig. to help demonstrate the nature of these interpolation functions. The most important feature in Fig. 3 is that the each interpolation function equals one at its assigned node and zero at all the others.

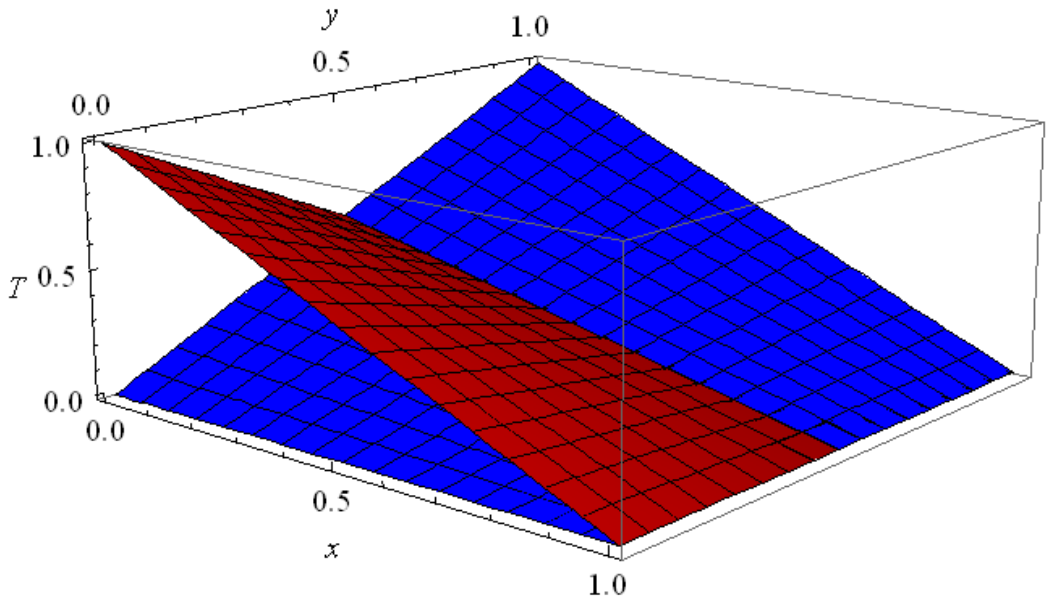

Fig. 3. Two different interpolation functions plotted together.

The higher-order interpolation function follows the same ideology however requires much more details to fully derive. Rather than the nodes being at the vertices, nodes are also placed inside the element. In essence, sixteen interpolations are derived that still maintain the property from (8). More details are provided when the aggregation study is further discussed.

III. Incorporating Interpolation Functions into Thermodynamic Equations

The next step is introducing these interpolation functions into the derived thermodynamic equation thus far, (6).

Begin finishing the FE derivation by substituting the approximated solution, (7), into (6).

$$\int_{\Omega_e}\left(\omega_e\left(\frac{1}{\alpha}\frac{\partial T}{\partial t}-H_{\mathrm{NP}}\right)+\nabla\omega_e\cdot\nabla T+\frac{c_b W_b}{k}T\right)dx\,dy+\oint_{\Gamma_e}\omega_e(\beta(T-T_0))\,ds=0 \qquad (10)$$

Next write (10) in terms of (x, y) coordinates.

$$\int_{\Omega_e}\left(\omega_e\left(\frac{1}{\alpha}\frac{\partial T}{\partial t}-H_{\mathrm{NP}}\right)+\frac{\partial\omega_e}{\partial x}\frac{\partial T}{\partial x}+\frac{\partial\omega_e}{\partial y}\frac{\partial T}{\partial y}+\frac{c_b W_b}{k}T\right)dx\,dy \qquad (11)$$
$$+\oint_{\Gamma_e}\omega_e(\beta(T-T_0))\,ds=0$$

Lastly, plug the approximated solution into (11).

$$\int_{\Omega_e}\left(\omega_e\left(\frac{1}{\alpha}\frac{\partial}{\partial t}\left(\sum_{j=1}^{M}T_j^e(t)\varphi_j^e\left(\vec{x}\right)\right)-H_{\mathrm{NP}}\right)+\frac{\partial\omega_e}{\partial x}\frac{\partial}{\partial x}\left(\sum_{j=1}^{M}T_j^e(t)\varphi_j^e\left(\vec{x}\right)\right)\right.$$

$$+\frac{\partial\omega_e}{\partial y}\frac{\partial}{\partial y}\left(\sum_{j=1}^{M}T_j^e(t)\varphi_j^e\left(\vec{x}\right)\right)$$

$$\left.+\frac{c_bW_b}{k}\left(\sum_{j=1}^{M}T_j^e(t)\varphi_j^e\left(\vec{x}\right)\right)\right)dx\,dy$$

$$+\oint_{\Gamma_e}\omega_e\left(\beta\left(\left(\sum_{j=1}^{M}T_j^e(t)\varphi_j^e\left(\vec{x}\right)\right)-T_0\right)\right)ds=0 \tag{12}$$

$$\sum_{j=1}^{M}\int_{\Omega_e}\left(\omega_e\left(\frac{1}{\alpha}\varphi_j^e\frac{\partial T_j^e}{\partial t}-H_{\mathrm{NP}}\right)\right.$$

$$\left.+\left(\frac{\partial\omega_e}{\partial x}\frac{\partial\varphi_j^e}{\partial x}+\frac{\partial\omega_e}{\partial y}\frac{\partial\varphi_j^e}{\partial y}+\frac{c_bW_b}{k}\varphi_j^e\right)T_j^e\right)dx\,dy$$

$$+\oint_{\Gamma_e}\omega_e(\beta\varphi_j^eT_j^e-T_0)\,ds=0 \tag{13}$$

The next important step is determining the form of the weight function. Until this point the weight function has not been specified but left arbitrary. However, enough information in the derivation is available to select a weight function that will prove advantageous for reasons that will be demonstrated later. Thus, following the Galerkin

scheme, define the weight function as equal to the approximation function specified for temperature, shown below in (14).

$$\omega_e = \sum_{j=1}^{M} \varphi_j^e \left(\vec{x}\right) \tag{14}$$

Plug the defined weight function, (14), into the derived thermodynamic equation thus far, (13).

$$\sum_{j=1}^{M} \int_{\Omega_e} \left(\left(\frac{1}{\alpha} \varphi_i^e \varphi_j^e \frac{\partial T_j^e}{\partial t} - \varphi_i^e H_{\mathrm{NP}} \right) + \left(\frac{\partial \varphi_i^e}{\partial x} \frac{\partial \varphi_j^e}{\partial x} + \frac{\partial \varphi_i^e}{\partial y} \frac{\partial \varphi_j^e}{\partial y} + \frac{c_b W_b}{k} \varphi_i^e \varphi_j^e \right) T_j^e \right) dx\, dy + \oint_{\Gamma_e} \varphi_i^e (\beta \varphi_j^e T_j^e - T_0)\, ds = 0 \tag{15}$$

(15) can be further simplified and understood by introducing the following definitions:

$$\sum_{j=i}^{M} \left(M_{\mathrm{ij}}^e \frac{\partial T_j^e}{\partial t} + K_{\mathrm{ij}}^e T_j^e \right) = f_i^e + Q_i^e \tag{16}$$

where M_{ij}^e, K_{ij}^e, and f_i^e are defined below in (17), (18), and (19), respectively, and Q_i^e is the boundary term for each e^{th} element.

$$M_{\mathrm{ij}}^{e} = \int_{\Omega_e} \left(\frac{1}{\alpha} \varphi_i^e \varphi_j^e \right) dx\, dy \tag{17}$$

$$K_{\mathrm{ij}}^{e} = \int_{\Omega_e} \left(\frac{\partial \varphi_i^e}{\partial x} \frac{\partial \varphi_j^e}{\partial x} + \frac{\partial \varphi_i^e}{\partial y} \frac{\partial \varphi_j^e}{\partial y} + \frac{c_b W_b}{k} \varphi_i^e \varphi_j^e \right) dx\, dy \tag{18}$$

$$f_i^e = \int_{\Omega_e} (\varphi_i^e H_{\mathrm{NP}})\, dx\, dy \tag{19}$$

The final derived equation, (16), is a concise written form of a series of ordinary differential equations that approximate the solution of the original partial differential thermodynamic equation. The i^{th} index of M_{ij}^{e}, K_{ij}^{e}, f_i^e, and Q_i^e represents each ordinary differential equation for each node in the entire simulation domain. The j^{th} index represents the node associated with each e^{th} element. In the final compilation, M_{ij}^{e} and K_{ij}^{e} are R x R matricies, where R is the number of nodes in the simulation domain. The external heating applied to the system is represented by f_i^e, with an i^{th} index per e^{th} element. All components of (16) are known including the interpolation function, φ_i^e, and external heating due to nanoparticles, H_{NP}, except for the unknown to be solved: $T\left(\vec{x}, t\right)$.

The α-family time approximation scheme was utilized to solve (16) where for this case $\alpha = 1/2$, the Crank-Nickolson [2] scheme. The scheme is shown below in (20).

$$\{T_{s+1}\} = \{T_s\} + \Delta \mathrm{t}[(1-\alpha)\{\dot{T}_s\} + \alpha\{\dot{T}_{s+1}\}] \tag{20}$$

After the code was written to solve the above FE scheme, it was validated against Candeo [3] with the same simulation setup as presented in his paper.

V. References

[1] R. Xu, H. Yu, Y. Zhang, M. Ma, Z. Chen, C. Wang, G. Teng, J. Ma, X. Sun and N. Gu, "Three-Dimensional Model for Determining Inhomogeneous Thermal Dosage in a Liver Tumor During Arterial Embolization Hyperthermia Incorporating Magnetic Nanoparticles," *IEEE Transactions on Magnetics,* vol. 45, no. 8, 2009.

[2] J. Reddy, An Introduction to the Finite Element Method, 2nd ed., McGraw-Hill, 1993.

[3] A. Candeo and F. Dughiero, "Numerical FEM Models for the Planning of Magnetic Induction Hyperthermia Treatments with Nanoparticles," *IEEE Transactions on Magnetics*, vol. 45, no. 3, 2009.

Chapter 3: FEM Optimization of Energy Density in Tumor Hyperthermia using Time-Dependent Magnetic Nanoparticle Power Dissipation

Koch, Caleb[1]**; Winfrey, Leigh**[2]

[1]Engineering Science and Mechanics, Virginia Tech, Blacksburg, VA 24061
[2]Nuclear Engineering, Virginia Tech, Blacksburg, VA 24061

Corresponding Author Email: caleb.koch@vt.edu

Chapter 3 was published in IEEE Transactions on Magnetics.

Koch, C.; Winfrey, L. FEM Optimization of Energy Density in Tumor Hyperthermia using Time-Dependent Magnetic Nanoparticle Power Dissipation. IEEE Transactions on Magnetics. DOI: 10.1109/TMAG.2014.2331031

FEM Optimization of Energy Density in Tumor Hyperthermia using Time-Dependent Magnetic Nanoparticle Power Dissipation

Caleb M. Koch[1], A. L. Winfrey[2], *Member, IEEE*

[1]Engineering Science and Mechanics, Virginia Polytechnic Institute and State University, Blacksburg, VA 24061 USA
[2]Nuclear Engineering, Virginia Polytechnic Institute and State University, Blacksburg, VA 24061 USA

General principles are developed using a Finite Element Model (FEM) regarding how time-dependent power dissipation of magnetic nanoparticles can be utilized to optimize hyperthermia selectivity. In order to make the simulation more realistic the finite size and spatial location of each individual nanoparticle is taken into consideration. When energy input into the system and duration of treatment is held constant, increasing the maximum power dissipation of nanoparticles increases concentrations of energy in the tumor. Furthermore, when the power dissipation of magnetic nanoparticles rises linearly, the temperature gradient on the edge of the tumor increases exponentially. With energy input held constant, the location and duration of maximum power dissipation in the treatment time scheme will affect the final energy concentration inside the tumor. Finally, connections are made between simulation results and optimization of the design of nanoparticle power dissipation time-schemes for hyperthermia.

***Index Terms*—Magnetic Nanoparticles, Hyperthermia Optimization, Finite-Element Modeling, Treatment Planning**

I. Introduction

Optimizing iron oxide nanoparticles (IONPs) with respect to cancer drug delivery and selectivity is one of the most promising fields of nanomedicine. Mitigating the negative consequences of traditional chemotherapy can be achieved by spatially and temporally controlling the distribution of Iron Oxide Nanoparticles conjugated with chemotherapy drugs in the body.

IONP's low cytotoxicity compared to other nanoparticles, such as gold, silver and titanium, allow higher concentrations of IONPs to be used safely in treatment. These higher concentrations will result in greater heat dissipation in the tumor leading to more effective cancer treatments [1] [2] [3]. IONPs are extraordinarily versatile; the application of high frequency and intensity magnetic field via Magnetic Resonance Imaging has become a mature and reliable technology [4] [5]. Decreasing the magnetic field's frequency a few orders of magnitude causes IONPs to dissipate energy and induce hyperthermia, causing localized heating, that can be fine-tuned to lie within the required therapeutic range. Furthermore, when conjugated with other biochemicals controlled drug targeting can be achieved [6] [7] [8].

More specifically, hyperthermia is achieved by applying an alternating magnetic field to IONPs and power dissipation occurs due to hysteresis loss, induced eddy currents, and Néel Relaxation [9]. Experimental studies have laid much of the foundation for understanding physiological responses to IONP induced hyperthermia. Particles composed of Fe_3O_4 were loaded into human breast cancer xenografts in immunodeficient mice at 7.7% weight concentration. Applying AC magnetic fields with an intensity of 6.5 kA/m and frequency of 400 kHz for 4 min. resulted in elevated temperatures of ΔT= 18-55˚C. However, IONPs were found to be heavily unevenly distributed in the form of agglomerates, which resulted in heterogeneous temperature distributions [10] [11].

Manuscript received January 1, 2014. Corresponding author: C. Koch (email: caleb.koch@vt.edu).
Digital Object Identifier inserted by IEEE

More powerful than hyperthermia alone is combining heat treatment with chemical therapeutics. One example of a carrier widely accepted for drug transportation is Liposomes [12] with polyethylene glycol (PEG) surface modifications [13]. In an experimental study, PEG-coated Liposomes in combination with IONP hyperthermia ablation resulted in increased intratumoral doxorubicin accumulation and increased mean tumor coagulation diameter (13.1 mm) compared to IONP hyperthermia treatment alone (6.7 mm) [14]. Several other studies in different animal models published similar results [15] [16]. Hyperthermia is an important IONP phenomenon to study because of its applications in the field of nanomedicine.

Numerical studies, in contrast to experimental studies, have not been as extensively utilized to study IONP hyperthermia. Analyzing the problem utilizing computer simulations offers the opportunity to study problems that experiments cannot because of regulations and financial restrictions. Xu in 2009 used experimental IONP imaging to replicate the 3D structure of a tumor, transferred this image to a Finite Element Model (FEM) program, assumed homogenous particle concentration, and compared experimental with numerical results [17]. Candeo in 2009 studied how to optimize hyperthermia with respect to particle concentration, diameter, and magnetic field intensity [18]. Several other simulations have studied hyperthermia through different perspectives [19] [20] [21]. This computational study contributes to current literature by understanding how time-dependence of iron oxide heat dissipation can be utilized to optimize hyperthermia. Furthermore, this FEM model offers a method of how to take into consideration the physical size and spatial location of each nanoparticle. The specifics of this method are discussed in the next section.

Optimizing current hyperthermia treatment is important for both clinical and research purposes. Less nanoparticles will be necessary for treatment if the process is optimized; this means lower levels of cytotoxic risk for the patient. Furthermore, parameters from computational studies may guide future experiments and make the process of research more efficient.

This FEM model is unique because it considers the finite size and spatial location of each individual IONP. By not approximating their heating capabilities, any asymmetry in temperature distribution becomes observable, further the FEM presented here considers time dependent IONP power distribution.

The objective of this research is to study how the time-dependent IONP power dissipation can be utilized to optimize hyperthermia by increasing energy density in tumors while decreasing energy density in surrounding healthy tissue.

II. METHODS

FEM Governing Equations

A finite element method was developed to solve the Penne's bio-heat transfer equation in the rectangular coordinate system [17], which is shown below in (1),

$$\frac{1}{\alpha}\frac{\partial}{\partial t}\theta(x,y,t) = \frac{\partial^2}{\partial x^2}\theta(x,y,t) + \frac{\partial^2}{\partial y^2}\theta(x,y,t) - \frac{c_b W_b}{k}\theta(x,y,t) + P_{\text{input}}(x,y,t) \quad (1)$$

Where $\alpha = \frac{k}{\rho c}$, k is the thermal conductivity of tissue (W/m˚C), ρ is the density of the tissue (kg/m^3), c is the specific heat of tissue (J/kg˚C), $\theta(x,y,t)$ describes the difference in temperature from the initial temperature, i.e. $\theta(x,y,t) = T(x,y,t) - T_0(x,y,0)$, c_b is the specific heat of blood (J/kg˚C), W_b is the blood perfusion rate (kg/m^3), and $P_{\text{input}}(x,y,t)$ is heating due to IONP power dissipation (W/m^2). The noteworthy portion in (1) for this paper is the time varying component of $P_{\text{input}}(x,y,t)$. Whereas other simulations provide constant power input, in this model the IOPN power dissipation is allowed to vary with time. The weak form of the finite element method is shown below in (2),

$$\int_{\Omega^e}\left(\omega\left(\frac{1}{\alpha}\frac{\partial\theta}{\partial t} - P_{\text{input}}\right) + k\left(\frac{\partial\omega}{\partial x}\frac{\partial\theta}{\partial y} + \frac{\partial\omega}{\partial y}\frac{\partial\theta}{\partial y}\right)\right)dx\,dy - \frac{1}{k}\oint_{\Gamma^e}\left(\omega\left(k\frac{\partial\theta}{\partial x}n_x + k\frac{\partial\theta}{\partial y}n_y\right)\right) = 0 \quad (2)$$

where Ω^e represents the area domain of each element, Γ^e represents the boundary of each element, $\omega(x,y)$ represents the interpolation function, and (n_x, n_y) equals unit x and y vectors on the boundary, respectively. Newton's law of cooling is introduced as the boundary condition, shown below in (3),

$$k_x\frac{\partial\theta}{\partial x}n_x + k_y\frac{\partial\theta}{\partial y}n_y - \beta\theta = \hat{q}_n \quad (3)$$

where $\hat{q}_n$ is the external heat flux and β is the convective constant. Equation (3) can be substituted into the boundary integral term of (2) producing (4):

$$\int_{\Omega^e}\left(\omega\left(\frac{1}{\alpha}\frac{\partial\theta}{\partial t} - P_{\text{input}}\right) + k\left(\frac{\partial\omega}{\partial x}\frac{\partial\theta}{\partial y} + \frac{\partial\omega}{\partial y}\frac{\partial\theta}{\partial y}\right)\right)dx\,dy - \frac{1}{k}\oint_{\Gamma^e}\left(\omega\left(\beta\theta + \hat{q}_n\right)\right) = 0 \quad (4)$$

According to the FEM scheme, the above equation is applied to each element of the discretized simulation space.

FEM Simulation Setup

Throughout the paper the IONP power dissipation resulting from f = 300 kHz, H_0 = 3300 A/m, and 3% particle concentration will be referred to as P_{norm}. Variations of IONP power dissipation will be in reference to P_{norm}, for example 1/2 P_{norm}.

The finite element method developed for this study solves the above weak form of the Bioheat equation for generalized time-varying power input. The Crank-Nicolson scheme [44] is utilized to solve this equation. 6400 elements were found to provide a sufficiently fine mesh grid to capture the temperature distribution. The code was validated against Candeo & Dughiero, 2009 [18] for the simulation setup of constant P_{norm} applied for 1800 s with a time step of 18 s.

The physical size and spatial location of each nanoparticle in the simulation was incorporated in the FE model. Each IONP was placed onto the simulation space dictated by a Gaussian probability function, with the center of the Gaussian at the center of the tumor. This profile models general diffusion resulting from direct injection of IONPs into the center of the tumor. Next, the IONP is weighted into the heating function of the element the IONP resides in. This is done for each IONP in the simulation. By the end a piecewise heating function is developed that is characterized by the specific size and location of each IONP.

The temperature gradient was utilized as the characterizing parameter of hyperthermia selectivity. A greater temperature gradient indicates a greater temperature difference between the tumor and the surrounding healthy tissue. This increase in temperature difference is indicative of a greater disparity between the high energy in the tumor and low energy in surrounding tissue.

III. Results and Discussion

Several simulation studies were designed in order to develop general conclusions concerning the optimal time-dependent power dissipation from IONPs for hyperthermia selectivity. First, while the energy input is held constant, the maximum power dissipation (P_{max}) of IOPNs changes. Second, observing the power dissipation as a linear function further develops the understanding of time-dependent IONPs power dissipation. Third, principles are developed concerning how to design power dissipation time schemes in order to optimize energy concentrations in tumors. Finally, maintaining constant energy input is studied to understand the relationship between P_{max} and the temperature gradient.

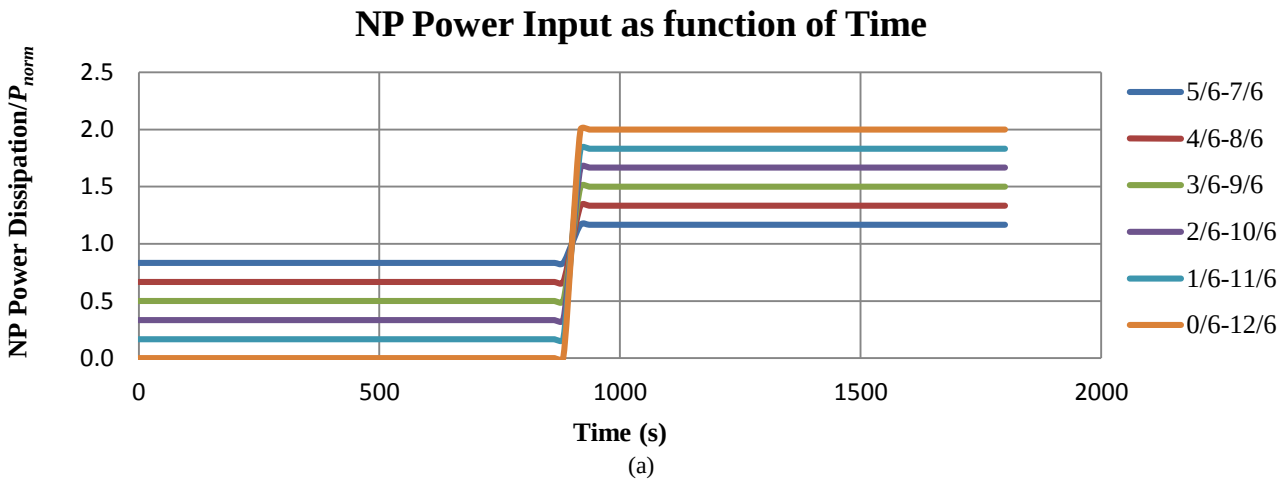

(a)

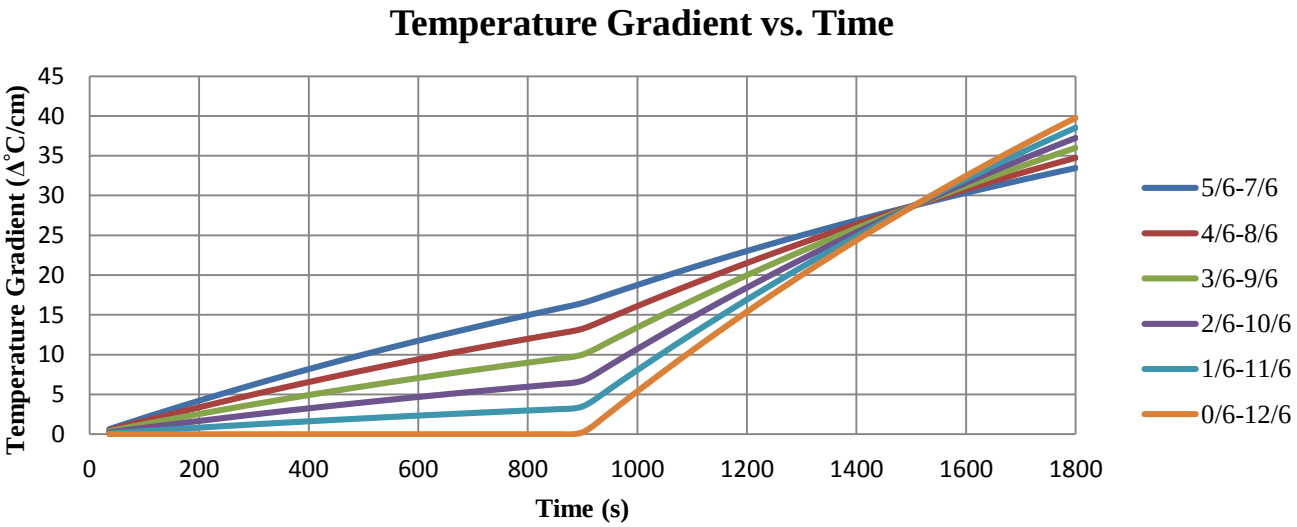

(b)

Fig. 1 (a) Power input for each simulation run as a function of time. For example: 5/6-7/6 means first stage of power input = 5/6 P_{in} and second stage of power input = 7/6P_{in}, averaging to P_{in} over 1800 s. (b) Average temperature gradient corresponding to each power scheme as a function of time

A. Importance of Maximum Power Increase

The first simulation experiment is designed to understand how the maximum power input affects the final temperature gradient. To compare the results of each time-varying power scheme, the average energy input and the duration of each simulation is held constant at 1800 s. In order to observe the relationship between maximum power input and final temperature gradient, simulations were designed as follows: first a fraction of P_{norm} lasts for 900 seconds and second the power is increased to maintain a constant average IONP power dissipation. For each simulation, the phrase "5/6-7/6" in Fig.1.a indicates the first 900s was 5/6 of P_{norm}, and the second 900s was 7/6 of P_{norm}. Fig 1.a shows the power dissipation of IONPs for each power scheme as a function of time, and Fig. 1.b shows the resulting average temperature gradient from the edge of the tumor to 1cm away from the tumor. As shown in Fig. 1.b, though the average power input is equal, the final temperature gradient in each case is not. Specifically, the 5/6-7/6 case, with the lowest maximum power dissipation, had a 33.5Δ^0C/cm temperature gradient while the 0/6-12/6 case, with the highest maximum power dissipation, had a temperature gradient of 41.0Δ^0C/cm, a 21% increase.

The difference in temperature gradient, even though the energy input remained constant, is derived from the nonlinear nature of the solution to the Bioheat equation in (1). Systems undergoing constant heat input will exponentially asymptote toward equilibrium. Therefore, the most significant changes in temperature occur during the beginning stages of heating. A factor in the rate of temperature growth is heating intensity. Increasing heating intensity will increase the rate of temperature grown. As demonstrated by these simulations, the increased heating intensity, as demonstrated by the "0/6-12/6" case, and keeping energy input into the system constant with respect to each simulation, is significant enough to overcome the lower heating intensities with longer time scales. Again, this is due to the nonlinear increase in temperature resulting from constant IONP heating. In conclusion, while maintaining energy input constant, as the maximum power dissipation increases the final temperature gradient will also increase.

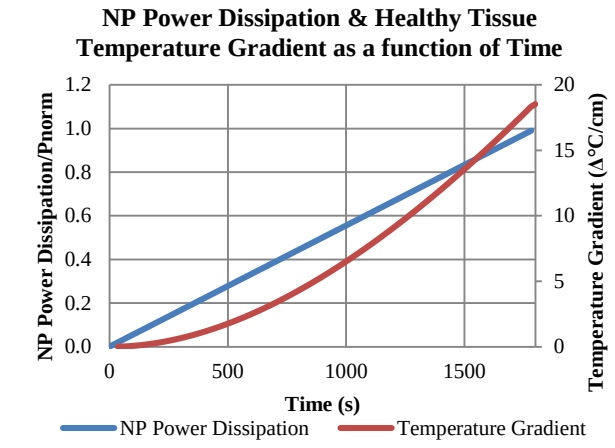

(a)

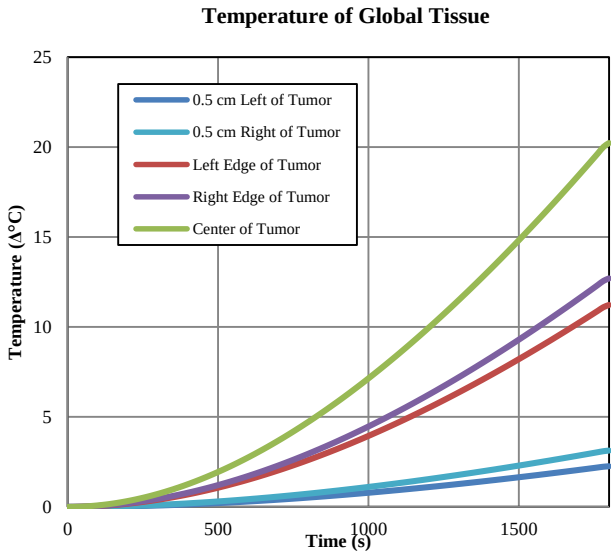

(b)

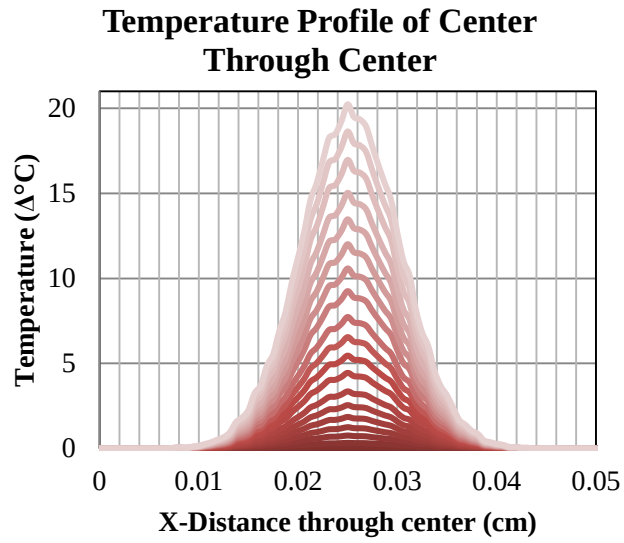

(c)

Fig. 2:(a)NP power dissipation and temperature gradient of healthy tissue as function of time (b) Temperature of important locations in simulation (c)150 second equal increments time slices of the temperature distribution across the X-axis and through the peak NP concentration

B. Power Input as a Linear Function of Time

To further illustrate the role of maximum power dissipation in optimizing the temperature gradient inside the body, a simulation was run with the power dissipation of IONPs as a linearly increasing function, as is illustrated in Fig. 2.a. In Fig. 2.c, the temperature is plotted from the center y-line of the simulation. This has the highest temperature profile because it passes through the highest concentration of IONPs. Furthermore, each curve in Fig. 2.c represents temperature profiles of equal 150 s increments. Important points in the simulation, including the center of the tumor, both edges of the tumor, and 0.5cm on either side of the tumor, are plotted as a function of time in Fig. 2.b. Note in both Fig. 2.b and 2.c that asymmetry and non-uniformity exists. This arises from the IONPs in the FE model having finite sizes and uneven distributions inside the tumor. Also in Fig. 2.c, by 2 cm away from the edge of the tumor, the temperature ceases to increase. This is important for ensuring consistency with experimental results.

Note the temperature gradient in Fig. 2.a rises exponentially as the power dissipation of IONPs rise linearly. This is indicative of the benefit derived from increasing maximum power input. Furthermore, the temperature gradient increases more during the last 900s than in the first 900s. This leads to the conclusion that exponential benefit is obtained from greater increases in maximum power.

C. Different Power Scheme with Equal P_{max} Affects Final Temperature Gradient

Having developed an argument for the role of maximum power input, the next simulations describe how to optimize time-schemes while maintaining constant average energy input and maximum power input. The simulations are as follows: the first 600 s is $1/2P_{norm}$, the second 600 s is P_{norm}, and the final 600 s is $3/2P_{norm}$. The second simulation has the reverse order of the first simulation. Lastly, the results are compared to constant P_{norm} over 1800 s. Each power time-scheme is plotted in Fig. 3.a. The resulting temperature gradient for each power time-scheme is shown in Figure 3.b.

Note, the scheme with P_{max} in the last 600 s has a lower temperature gradient than constant power input. In fact, in the last 600s the temperature gradient of the 3/2-1-1/2 scheme decreased. This indicates that a power scheme with P_{max} in the first portion of IONP power dissipation does not increase energy concentration inside tumors. This is understood by further analyzing Fig. 3.b. During highest IONP heat dissipation the run with $3/2P_{norm}$ increased 19.8˚C while the run with $3/2P_{norm}$ last increased 16.0˚C. This is a small difference, especially when considering each started at different initial temperatures. The reason a large discrepancy in final temperature was due to the lower heating operation, $1/2P_{norm}$. The run with 3/2 P_{norm} in the beginning decreased temperature by 0.53˚C. This occurred because the system was converging to thermal equilibrium, which for lower heating results in a smaller temperature profile. However, the run with 3/2 P_{norm} at the end increased in temperature by 6.98˚C during

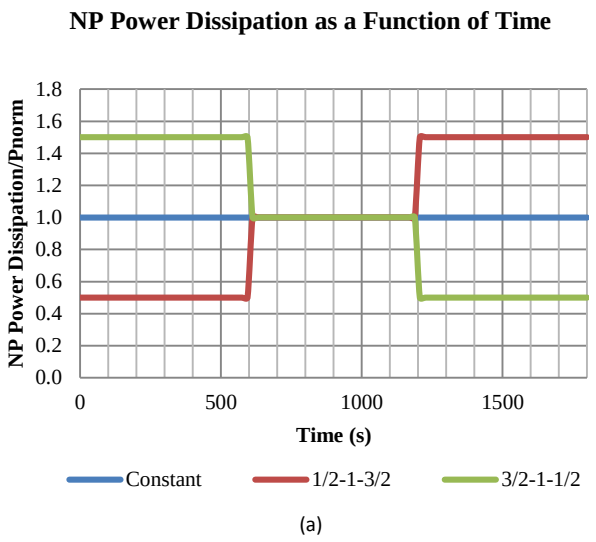

Fig 3: (a) Power dissipation as a function of time. Normalized to 300 kHz and 1.2 A/m. (b) Averaged temperature gradient from edge of tumor to 0.5 cm away.

lower heating intensity. The IONP heating scheme that allowed heating functions to build from previous lower heating operations is advantageous because this allows, as discussed in the previous section, the nonlinear nature of thermal heating to be employed for optimized final temperatures.

Second, the power time-scheme with P_{max} in the last 600 seconds has ~$\Delta 5^{\circ}$C/cm greater final temperature gradient, which indicates a higher energy density inside the tumor. In conclusion, it is important to design P_{max} toward the end of the power time-schemes in order to maximize the final temperature gradient.

D. Role of P_{max} Duration in Temperature Gradient

The last computational hyperthermia study conducted was designed to understand how the length of P_{max} affects the final temperature gradient. To compare each simulation P_{max} was held constant as well as average energy input, during which the duration of P_{max} changes. Fig. 4.a shows the power input as a function of time. To clarify, the phrase "2/6-1028" means the first stage has 2/6 P_{norm} and the second stage has P_{max} for 1028 seconds. The 1028s, and all other time values, are calculated to ensure average energy input into the system remains constant across all simulations.

Fig. 4.b shows the temperature gradient for each power time-scheme as a function of time. The greatest temperature gradient, $\Delta 37^{\circ}$C, was generated from the 0/6-1200 scheme; the lowest temperature gradient, $\Delta 34^{\circ}$C, was generated from the 5/6-450 case. As shown from the data, even though energy input was held constant, there was an increase in temperature gradient as the duration of P_{max} increased. However, the increase was not as significant compared to the results from the previous three sections. While the duration of P_{max} input increased 167%, the temperature gradient increased only 8.8%. Previously found the magnitude of P_{max} is important for increasing hyperthermia selectivity. However, the duration of P_{max} is not as strong of a contributing factor, shown by the small increase in temperature gradient when P_{max} is dramatically increased. This is because of the nature of the solution to the Bioheat equation, which was also the reason for Systems undergoing constant heat input will exponentially asymptote toward equilibrium. The most significant changes in temperature occurs during the beginning stages of heating. In this scenario of changing the duration of P_{max}, capturing the beginning stages of heating, and the time when temperature changes most quickly, is sufficient. Further heating contributes little to increased hyperthermia selectivity.

IV. Conclusions

The conclusions from the preceding computational study will be directed toward hyperthermia treatment planning. Though constant power dissipation from IONPs is an obvious option, it is not the optimal option when attempting to concentrate energy inside tumors. From the general principles derived in this paper, time varying power dissipations from IONPs increase tumor temperature while decreasing surrounding healthy tissue temperature by three methods, which in each case was shown by increasing the temperature gradient at the edge of the tumor. First and most important, the maximum power dissipation of IONPs plays a pivotal role in hyperthermia selectivity. Increasing the maximum IONP power dissipation creates a sharper temperature gradient between cancerous and healthy tissues, which is desired when attempting to mitigate local hyperthermia damage. Secondly, when planning the time-scheme of hyperthermia treatments, P_{max} should be placed toward the end of the treatment. Allowing temperature gradients to build off one another due to different dissipation powers optimizes the localization of energy. Lastly, increasing the time of P_{max} being applied to the

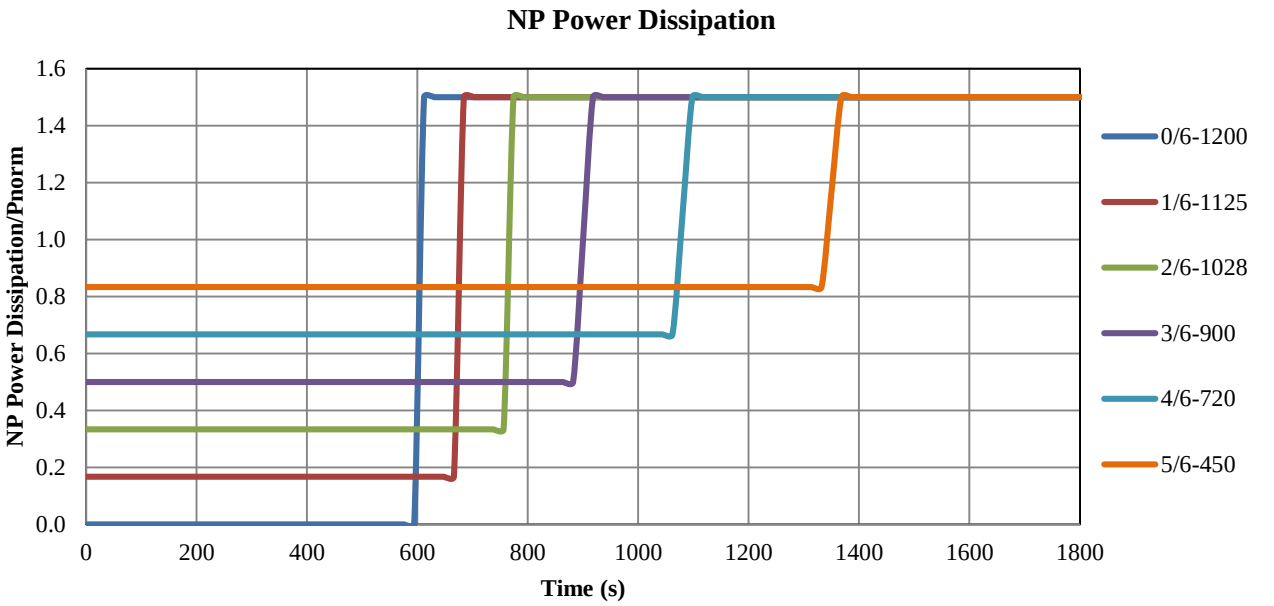

(a)

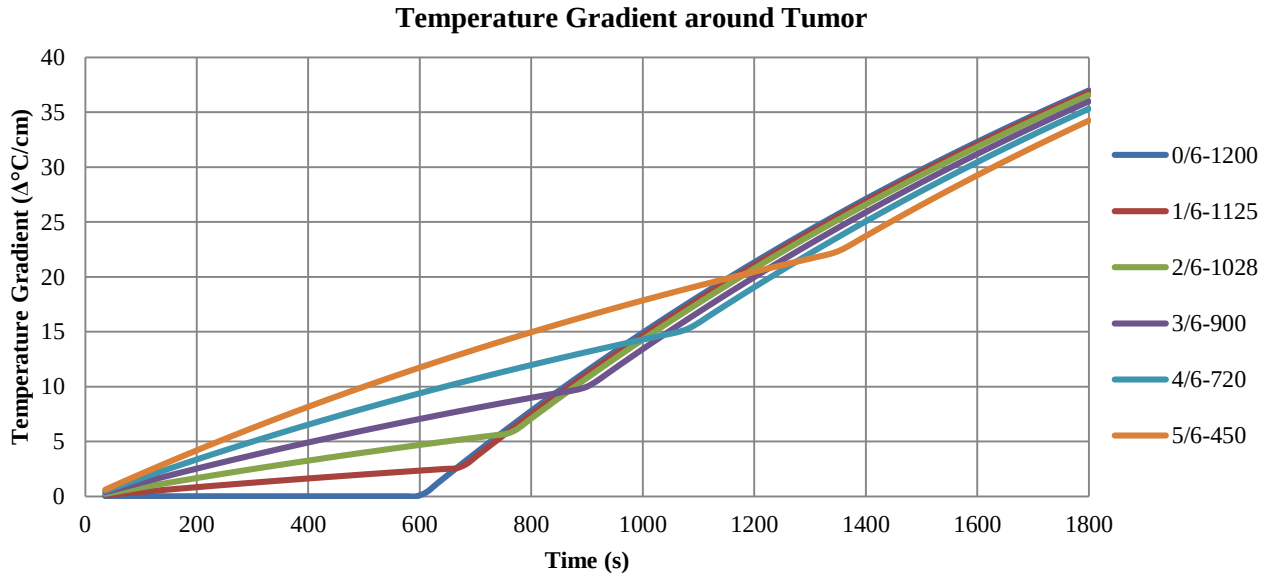

(b)

Fig 4. (a) Power-time scheme of simulations. "1/6-1125" means the first power input is 1/6th of normal power operations, and 1125 is the duration of 3/2 increase of normal power operations. (b) Temperature gradient of each power scheme.

system certainly increases localization of energy. However, when compared to the first two points, it benefits only slightly.

The more important aspect is the value of P_{max} regardless of how long IONP power dissipation is at that value.

ACKNOWLEDGMENT

This work was supported by the Mechanical Engineering department at Virginia Tech. Special thanks to Dr. Finkielstein in the Biology Department for the insightful discussions.

V. REFERENCES

[1] A. Sabuncu, J. Grubbs, S. Qian, T. Abdel-Fattah, M. Stacey and A. Beskok, "Probing Nanoparticle Interactions in Cell Culture Media," *Colloids and Surfaces B: Biointerfaces*, vol. 95, 2012.

[2] A. Gupta, R. Naregalker, V. Vaidya and M. Gupta, "Recent Advancements on Surface Engineering of Magnetic Iron Oxide Nanoparticles and their Biomedical Applications," *Nanomedicine*, vol. 2, 2007.

[3] A. Gupta and A. Curtis, "Surface Modified Superparamagnetic Nanoparticles for Drug Delivery: Interaction Studies with Human Fibroblasts in Culture," *Journal of Materials Science: Materials in*

Medicine, vol. 15, no. 4, pp. 493-496, 2004.

[4] R. Weissleder, A. Bogdanov, E. Neuwelt and M. Papisov, "Long-Circulating Iron Oxides for MR Imaging," *Advanced Drug Delivery Reviews,* vol. 16, no. 2, pp. 321-334, 1995.

[5] J. Bulte and D. Kraitchman, "Iron Oxide MR Contrast Agents for Molecular and Cellular Imaging.," *NMR in Biomedicine,* vol. 17, 2004.

[6] S. Moghimi, A. Hunter and J. Murray, "Long-Circulating and target-Specific Nanoparticles: Theory and Practice," *Pharmacological Reviews,* vol. 53, 2001.

[7] D. Emerich and C. Thanos, "The Pinpoing Promise of Nanoparticle-Based Drug Delivery and Molecular Diagonsis," *Biomolecular Engineering,* vol. 23, 2006.

[8] M. Takeda, H. Tada, H. Higuchi and e. al., "In Vivo Single Molecular Imaging and Sentinel Node Navigation by Nanotechnology for Molecular Targeting Drug-Delivery Systems and Tailor-made Medicine," *Breast Cancer,* vol. 15, no. 2, pp. 145-152, 2008.

[9] E. Adair, D. Blick, S. Allen, K. Mylacraine, J. Ziriax and D. Scholl, "Thermophysiological Responses of Human Volunteers to Whole Body RF Exposure at 220 MHz," *Bioelectromagnetics,* vol. 26, no. 6, 2005.

[10] I. Hilger, R. Hiergeist, R. Hergt, K. Winnefeld, H. Schubert and W. Kaiser, "Thermal Ablation of Tumors Using Magnetic Nanoparticles: An In Vivo Feasibility Study," *Investigative Radiology,* vol. 37, no. 10, pp. 580-586, 2002.

[11] J. Sakamoto and e. al., "Enabling individualized therapy through nanotechnology," *Pharmacological Research,* vol. 62, no. 2, pp. 57-89, 2010.

[12] A. Gordon, C. Granai, P. Rose, J. Hainsworth, A. Lopez, C. Weissman and e. al., "Phase II Study of Liposomal Doxorubicin in Platinum- and Paclitaxelrefractory Epithelial Ovarian Cancer," *Oncology,* vol. 18, 2000.

[13] H. Zhao, G. Li, R. Wang, S. Li, J. Wei, M. Feng and e. al., "A Comparative Study of Transfection Efficiency between Liposomes, Immunoliposomes, and Brain-specific Immunoliposomes," *The Journal of International Medical Research,* vol. 38, no. 3, pp. 957-966, 2010.

[14] M. Ahmed, W. Monsky, G. Girnun, A. Lukyanov, G. D'Ippolito, J. Kruskal and e. al., "Radiofrequency Thermal Ablation Sharply Increases Intratumoral Liposomal Doxorubicin Accumulation and Tumor Coagulation," *Cancer Research,* vol. 63, 2003.

[15] M. Ahmed and S. Goldberg, "Combination Radiofrequency Thermal Ablation and Adjuvant IV Liposomal Doxorubicin Increases Tissue Coagulation and Intratumoural Drug Accumulation," *International Journal of Hyperthermia,* vol. 20, no. 7, pp. 781-802, 2004.

[16] M. Ahmed, A. Lukyanov, V. Torchilin, H. Tournier, A. Schneider and A. Godlberg, "Combined Radiofrequency Ablation and Adjuvant Liposomal Chemotherapy: Effect of Chemotherapeutic Agent, Nanoparticle Size, and Circulation Time.," *Journal of Vascular and Interventional Radiology,* vol. 16, no. 10, pp. 1365-1371, 2005.

[17] R. Xu, H. Yu, Y. Zhang, M. Ma, Z. Chen, C. Wang, G. Teng, J. Ma, X. Sun and N. Gu, "Three-Dimensional Model for Determining Inhomogeneous Thermal Dosage in a Liver Tumor During Arterial Embolization Hyperthermia Incorporating Magnetic Nanoparticles," *IEEE Transactions on Magnetics,* vol. 45, no. 8, 2009.

[18] A. Candeo and F. Dughiero, "Numerical FEM Models for the Planning of Magnetic Induction Hyperthermia Treatments with Nanoparticles," *IEEE Transactions on Magnetics,* vol. 45, no. 3, 2009.

[19] W. Andra, C. d'Ambly, R. Hergt, I. Hilger and W. Kaiser, "Temperature Disbribution as Function of Time Around a Small Spherical Heat Source of Local Hyperthermia," *Journal of Magnetism and Magnetic Materials,* vol. 194, 1999.

[20] S. Maenosono and S. Saita, "Theoretical Assessment of FePt Nanoparticles as Heating Elements for Magnetic Hyperthermia," *IEEE Transactions on Magnetics,* vol. 42, no. 6, 2006.

[21] N. Tsafnat, G. Tsafnat, T. Lambert and S. Jones, "Modelling Heating of Liver Tumours with Heterogeneous magnetic microsphere deposition," *Physics in Medicine and Biology,* vol. 50, no. 12, 2005.

[22] J. Reddy, An Introduction to the Finite Element Method, 2nd ed., McGraw-Hill, Inc., 1993.

Chapter 4: FEM Analysis of Controlling Hyperthermia States using Magnetically Induced Iron Oxide Nanoparticle Heat Dissipation

Casey, Abigail[1]**; Koch, Caleb**[2]**; Winfrey, Leigh**[3]

[1]Material Science and Engineering, Virginia Tech, Blacksburg, VA 24061
[2]Engineering Science and Mechanics, Virginia Tech, Blacksburg, VA 24061
[3]Nuclear Engineering, Virginia Tech, Blacksburg, VA 24061

Corresponding Author Email: caleb.koch@vt.edu

Submitted to IEEE Transactions on Magnetics for review

FEM Analysis of Controlling Hyperthermia States using Magnetically Induced Iron Oxide Nanoparticle Heat Dissipation

Abigail H.M. Casey[1], Caleb M. Koch[2], and A. Leigh Winfrey[3], *Member, IEEE*

[1]Chemical Engineering Department, Virginia Tech, Blacksburg, VA 24060 USA
[2]Engineering Science and Mechanics Department, Virginia Tech, Blacksburg, VA 24060 USA
[3]Nulclear Engineering Department, Virginia Tech, Blacksburg, VA 24060 USA

This work utilizes a Finite Element Model (FEM) to develop parameters about how to control temperature profiles during Iron Oxide Nanoparticle Magnetic Hyperthermia. Previous work has looked at how time-dependent heat dissipation of nanoparticles can be utilized to optimize the selectivity of hyperthermia. As a next step, this paper builds from previously developed optimization principles and understands how time-dependent heat dissipation can be utilized to control desired temperature hyperthermia states. During constant heat dissipation the time it takes for tumors to reach optimal hyperthermia states follows a power law of the order -1.15. When the nanoparticle heat dissipation is increased from x0.25 to x1 normal operation time decreases by a factor of 5. However, when nanoparticle heat dissipation is increased from x1 to x2 normal operations, the time benefit gained is only a factor of 2. In the case considered here, with 3% nanoparticle concentration, when the tumor's temperature was selectively increased to 42°C or above a 86% reduction of heat dissipation resulted in the temperature profile to effectively freeze in time. The value of power reduction value to freeze hyperthermia states is dependent on the desired hyperthermia states. The results provide insight into how to reach optimal hyperthermia states, cost-benefits to different nanoparticle heat dissipation intensities, and how to control tumor-selective hyperthermia states.

***Index Terms*— Finite Element Modeling; Hyperthermia Control; Iron Oxide Nanoparticles**

I. Introduction

The control of Iron Oxide Nanoparticles (IONPs) in their use for chemical therapeutics in cancer drug delivery is an important study in the field of nanomedicine [1]. The combination of chemical therapeutics and IONP heat treatment is a powerful tool in selective elimination of tumor cells [2] [3] [4]. Experimentally, researchers are finding novel methods to deeply seed nanoparticles inside tumors [5]. For example, Wong has found that physiological barriers that hinder delivery of the nanotherapeutics tumor can be overcome by utilizing a multistage deliver system that uses smaller NPs to diffuse through the boundary, and later builds together to complete the nanotheraputic objective [6].

Theoretical and computational studies have also been effective in advancing the field of IONPs, for it provides a powerful means to study a variety of case studies without balancing ethics. Candeo developed parameters determining the effects of changing IONP concentration in hyperthermia treatments [7]. Aggregation is one of the most difficult challenges to overcome in IONP delivery methods, and recently probability theory has elucidated the variability IONP aggregation introduces to final temperature profiles [8]. Computational studies have also demonstrated how time-dependent IONP heat dissipation can be functionalized to increase the selectivity of tumors [9]. However, much work has yet to be done in the maturation of IONP as a viable treatment option for cancer patients.

As a next step in understanding the thermodynamics associated with IONP heat dissipation, parameters need to be developed on how to use time-dependent IONP heat dissipation to control hyperthermia states. The study uses an FEM model that considered the size and location of each nanoparticle in the simulation.

II. Methods

Finite Element Model

A general 2D Finite Element Model (FEM) was developed specialized to study discretized heating sources, in this case finite-sized IONP heating sources. The model begins with the heat conduction equation, shown below in (1)

$$\frac{1}{\alpha}\frac{\partial}{\partial t}\theta(x,y,t) = \frac{\partial^2}{\partial x^2}\theta(x,y,t) + \frac{\partial^2}{\partial y^2}\theta(x,y,t) + H_{\mathrm{NP}}(x,y,t) \quad (1)$$

where $\alpha = \frac{k}{\rho c}$, k is the thermal conductivity of tissue (W/m^{0}C), ρ is the density of the tissue (kg/m^3), c is the specific heat of tissue (J/kg^{0}C), $\theta(x,y,t)$ describes the difference in temperature from the initial temperature, i.e. $\theta(x,y,t) = T(x,y,t) - T_0(x,y,0)$, c_b is the specific heat of blood (J/kg^{0}C), and W_b is the blood perfusion rate (kg/m^3). The elemental weak form of (1) is obtained by multiplying by a test function, $\omega(x,y)$, and integrating over each j^{th} element, which results in

$$\int_{\mathcal{E}_j} (\omega(\frac{1}{\alpha}\frac{\partial\theta}{\partial t} - H_{\mathrm{i}}^{\mathcal{E}}) + k(\frac{\partial\omega}{\partial x}\frac{\partial\theta}{\partial y} + \frac{\partial\omega}{\partial y}\frac{\partial\theta}{\partial y}))\, dx\, dy - \frac{1}{k}\oint_{\Gamma^e} (\omega(\beta\theta + \hat{q_n})) = 0 \quad (2)$$

where $\mathcal{E}_j$ represents the area domain of each element and Γ^e represents the boundary of each element. The IONP heat function can be written explicitly, shown in (3)

$$H_{\mathrm{NP}}^{\mathcal{E}}(\vec{x},t)=\sum_{i=1}^{N}\int_{\mathcal{E}}A_i(t)\mathcal{X}_i(\vec{x})\omega(x,y)\,d\vec{x} \quad (3)$$

In other words, the total heat in element $\mathcal{E}$ is the sum of all $i \rightarrow N$ NPs in the domain of $\mathcal{E}$. The reason the heating intensity, $A_i(t)$, can be removed from the spatial location information of each i^{th} NP, $\mathcal{X}_i(\vec{x})$, is the assumption that the magnetic field is uniform in the simulation space. This method of considering each individual IONP allows the spatial nonlinearities of nonhomogeneous distributions to be understood, as will be seen in the results section.

Throughout this paper P_{norm} refers to the heat dissipation from IONPs resulting from f = 300 kHz, H_0 = 3300 A/m, and 3% particle concentration. This parameter is used to non-dimensionalize the time-varying heat dissipation of IONPs. The spatial location of each IONP in the simulation was weighted based off a Gaussian probability function. This models general diffusion that would result from direct needle injection of the nanoparticles in a tumor. Temperature Gradient is utilized as a parameter to relate to energy density inside the tumor. The greater the temperature gradient, the greater the energy density inside the tumor and consequently the more selective hyperthermia was.

III. Results and Discussion

Several IONP heat dissipation-time schemes were designed in order to understand the relationship between IONP heat dissipation intensity and time to reach optimal hyperthermia state. In each IONP heat intensity case, once the edge of the tumor, on average, reached a temperature increase of 5˚C, P_{norm} was reduced to control and maintain the tumor temperature profile. Lastly, general principles are developed concerning the cost-benefits to increasing IONP heat dissipation in hyperthermia treatments.

A. Temperature Profiles of Hyperthermia States

A temperature contour map of optimal hyperthermia state, as defined by the average temperature on the boundary between the tumor and healthy tissue being Δ5°C, is shown below in Fig. 1. Note that though the global IONP distribution is weighted by a Gaussian function, the final temperature is not a smooth Gaussian function. This is the result the discretized nature of equation (3), and each IONP's spatial position being considered in the simulation. The higher the IONP count then the smoother the IONP distribution function equals and, consequently, the smoother, and more predictable, the final temperature profile is.

B. Time Required to reach Optimal Hyperthermia States

Eight different IONP initial heat dissipation intensities, ranging from 0.25P_{norm} to 2P_{norm}, were analyzed to understand how it will change the time to reach the optimal hyperthermia state. Table 1 records the time it takes for each IONP heat dissipation intensity to reach the optimal hyperthermia state. The last column of Table 1 calculates the percent difference between the previous time and the current time. As evident, the percent difference with each increment of power becomes less and less, meaning the time-benefit gained from increasing the IONP heat dissipating intensity exponentially decreases.

TABLE I
TIME TO REACH OPTIMAL HYPERTHERMIA STATE

Power/P_{norm} (W/m^3)	Time (s)	Time (min)	Percent Difference (%)
0.25	1535.22	25.59	
0.50	617.07	10.28	59.8
0.75	388.84	6.48	37.0
1.00	284.30	4.74	26.9
1.25	224.24	3.74	21.1
1.50	185.24	3.09	17.4
1.75	157.87	2.63	14.8
2.00	137.10	2.29	13.2

The results from Table 1 are plotted in Fig. 1 and a power function is fitted to the curve. Shown in (4) the time to reach the optimal hyperthermia state decreases by a power of -1.149, with an R^2 value of 0.9976. The fitted equation is shown below in (4).

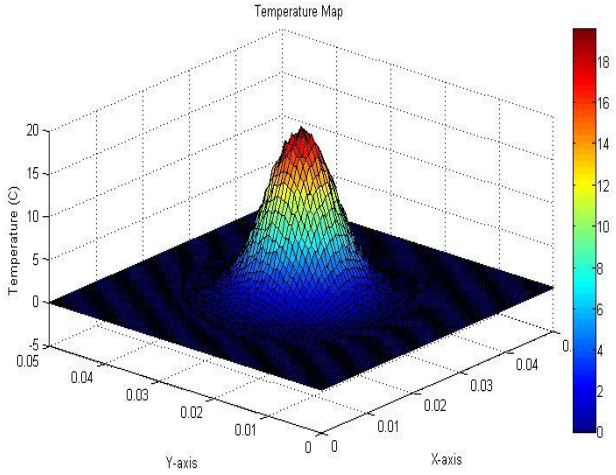

Fig. 1. Temperature contour map

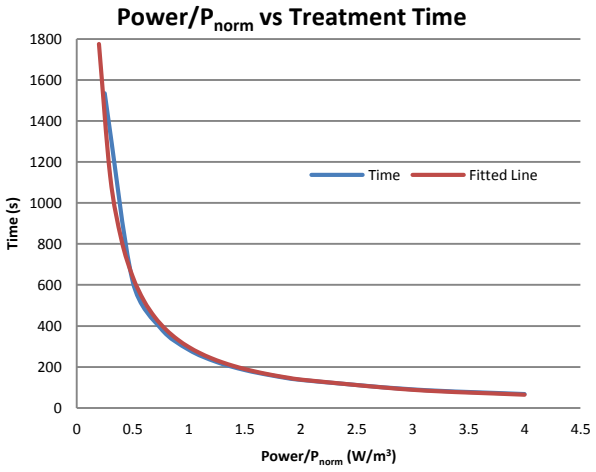

Fig 2. Power/P_{norm} vs treatment time to achieve optimal hyperthermia conditions.

$$\text{Time} = 292.7 * (H_{\text{NP}})^{-1.149} \quad (4)$$

The exponent being less than -1 is expected because as the power is increased to infinity the time it takes to reach optimal state should approach zero.

When the IONP heat dissipation is increased from 0.25 P_{norm} to P_{norm} the time decreases by a factor of 5. However, when IONP heat dissipation is increased from P_{norm} to $2P_{norm}$ the time decreases only a factor of two. As demonstrated by Fig. 2, if the IONP heat dissipation is increased beyond $1.25P_{norm}$ the time to reach optimal state plateaus. There is little savings in time by increasing the power beyond $1.25P_{norm}$. Increased power beyond $1.25P_{norm}$ would simply require additional energy while only minimally increasing damage to the tumor cells. The power-time relationship derived here and in Fig. 2 can be useful when the treatment time may need to be monitored and the predicted power input needs to be chosen.

C. Comparing Controlled Hyperthermia States

The next step is to compare the final controlled hyperthermia state with respect to global temperature and tumor selectivity. Fig. 3 is the IONP heat dissipation plotted against time during the simulation. When each of the eight different power inputs reach their respective optimal states they drop to the appropriate power to maintain a temperature rise of 5°C on the right edge of the tumor. Fig. 3 shows that the data fits the same power model as in Fig. 2.

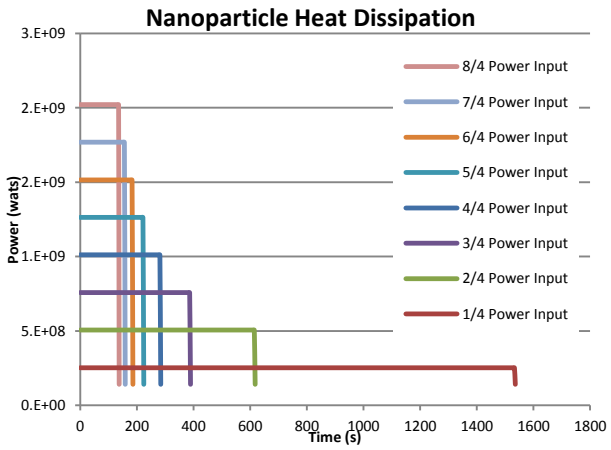

Fig 3. Nanoparticle Heat Dissipation for eight different power inputs ranging from $0.25P_{norm}$ to $2P_{norm}$.

Also of interest is the temperature of the center and average temperature at the edges of the tumor over the time it takes to reach optimal state. Fig. 4 shows the temperatures of the center and the boundary between the tumor and the healthy tissue as a function of time. Here only the $0.25P_{norm}$, $1P_{norm}$, and $2P_{norm}$ cases were chosen to be representative of heating behavior. The plateau of each plot is the point at which the run has reached optimal state. It can be seen that the time to reach optimal state for the $2P_{norm}$ is much shorter than for the $0.25P_{norm}$, yet the difference between the center and average edge temperatures are the same. There is no change when the power input is changed, which is indicative that the temperature profile effectively freezes during this second phase of IONP heat dissipation.

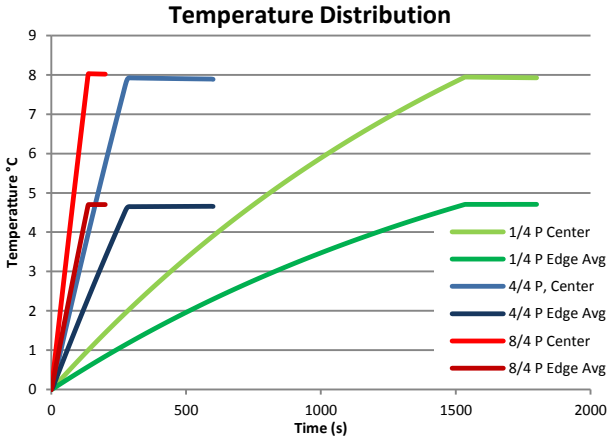

Fig 4. Nanoparticle Temperature Distribution over the tumor.

Another parameter that is important to note is the temperature gradient at the boundary of the tumor. A higher temperature gradient will indicate a higher energy difference between the tumor and the healthy tissue, which means an increase in selectivity. Fig. 4 shows the temperature gradient for each of the 8 IONP heat dissipation intensities.

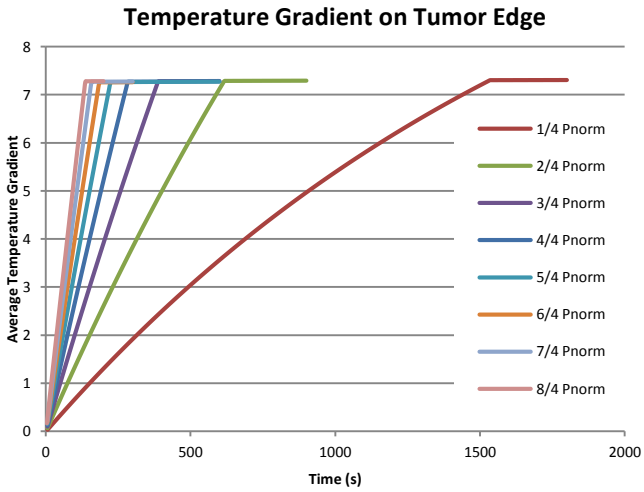

Fig 5. Average Temperature Gradient at the edges of the tumor until optimal state is achieved.

It can be seen in Fig. 4 that the final temperature gradients for each run after optimal state is achieved do not vary greatly. There is not a significant gain between the $0.25P_{norm}$ and the $2P_{norm}$ power inputs. The gain is 0.02 over a time change of approximately 1400 s. This increase is not considered significant. Therefore, although the temperature gradient achieved at $0.25P_{norm}$ was higher than the rest it is not a large enough increase to justify a treatment time over 1500 seconds.

The reason the temperature gradient does not change over each simulation run is because only constant power input is utilized. Had IONP heat dissipation varied with time previous

to the second controlling-phase of the hyperthermia treatment, as explained by Koch 2014 [9], a greater temperature gradient would have been achieved.

IV. Conclusions

The results in this study provide two main results: a computational proof of principle that hyperthermia states can be controlled and cost-benefits are associated with different IONP heat dissipation intensities. A significant amount of time, ~25 min, is required to reach the optimal hyperthermia state when IONP heat dissipation equals $0.25P_{norm}$. In real treatment applications this might be beneficial for more fragile patients that require a temperate treatment. However, for more aggressive hyperthermia treatments the optimal hyperthermia state can be reached in less than 45 seconds. However, with the greater rate of temperature growth more risk is associated with the patient. At the doctor's discretion, these results can provide information to design the best magnetic hyperthermia treatment plan for patients.

When IONP heat dissipation is constant, between each case of different IONP heat dissipation intensities, which are associated with different treatment options, center-tumor o temperature or boundary temperature gradients do not change significantly. Constant IONP heat dissipation results in the same energy density and tumor selectivity.

Future work includes conducting a sensitivity analysis on how aggregation affects treatment time, and the degree to which it introduces variability. Furthermore, a theoretical assessment relating the concentration of IONPs, IONP distribution, and tumor size needs to be developed in order to further generalize the concept of controlling hyperthermia states inside tumors.

V. References

[1] J. Sakamoto and e. al., "Enabling individualized therapy through nanotechnology," *Pharmacological Research,* vol. 62, no. 2, pp. 57-89, 2010.

[2] M. Ahmed, W. Monsky, G. Girnun, A. Lukyanov, G. D'Ippolito, J. Kruskal and e. al., "Radiofrequency Thermal Ablation Sharply Increases Intratumoral Liposomal Doxorubicin Accumulation and Tumor Coagulation," *Cancer Research,* vol. 63, 2003.

[3] Wahajuddin and A. Sumit, "Superparamagnetic Iron Oxide Nanoparticles: Magnetic Paltforms as Drug Carriers," *International Journal of Nanomedicine,* vol. 7, pp. 344-3471, 2012.

[4] M. Barati, K. Suziki, C. Selomulya and J. Garitaonandia, "New Tc-Tuned Manganese Ferrite-Based Magnetic Implant for Hyperthermia Therapy Application," *IEEE Transactions on Magnetics,* vol. 49, no. 7, 2014.

[5] R. Jain and T. Stylianopoulos, "Delivering nanomedicine to solid tumors," *Nat. Rev. Clin. Oncol.,* vol. 7, no. 11, pp. 653-664, 2010.

[6] C. Wong, T. Stylianopoulos, J. Cui, J. Martin, V. Chauhan, W. Jiang, Z. Popovic, R. Jain, M. Bawendi and D. Fukumura, "Multistage nanoparticle delivery system for deep penetration into tumor tissue," *PNAS,* vol. 108, no. 6, pp. 2426-2431, 2011.

[7] A. Candeo and F. Dughiero, "Numerical FEM Models for the Planning of Magnetic Induction Hyperthermia Treatments with Nanoparticles," *IEEE Transactions on Magnetics,* vol. 45, no. 3, 2009.

[8] C. Koch, A. Casey and A. Winfrey, "Theoretical Analysis of Magnetically Induced Iron Oxide Hyperthermia and Variability due to Aggregation," *Journal of Physics D,* p. Submitted for Review, 2014.

[9] C. Koch and A. Winfrey, "FEM Optimization of Energy Density in Tumor by using Time-Dependent Magnetic Nanoparticle Power Dissipation," *IEEE Transactions on Magnetics,* vol. Submitted for Review, 2014.

Chapter 5: FEM Analysis of Nanoparticle Magnetic Hyperthermia Resulting from Intravenous Diffusing and Radial-Modal Distributions

Koch, Caleb[1]**; Casey, Abigail**[2]**; Winfrey, Leigh**[3]

[1]Engineering Science and Mechanics, Virginia Tech, Blacksburg, VA 24061
[2]Material Science and Engineering, Virginia Tech, Blacksburg, VA 24061
[3]Nuclear Engineering, Virginia Tech, Blacksburg, VA 24061

Corresponding Author Email: caleb.koch@vt.edu

Chapter 5 is in preparation for submission to IEEE Transactions on Magnetics.

FEM Analysis of Nanoparticle Magnetic Hyperthermia Resulting from Intravenous Diffusion and Radial-Modal Distributions

Caleb M. Koch, *Fellow, IEEE*; Abigail H. M. Casey, *Fellow, IEEE*; A. L. Winfrey, Jr., *Member, IEEE*

***Abstract*—The distribution of Iron Oxide Nanoparticles greatly affects the resultant temperature profiles from magnetically induced hyperthermia. Two common methods of introducing nanoparticles are studied in this paper: first direct needle injection, which results in Gaussian profiles from general diffusion, and second intravenous diffusion through the tumor edge. A finite number of nanoparticles are considered in order to understand temperature asymmetry. Direct injection is an effective method of heating and selectively heats tumors rather than local healthy tissue. Only later stages of intravenous diffusion does effective hyperthermia become a viable option because of homogenized heating. Early stages of intravenous diffusion produce precarious heating on the tumor-healthy tissue boundary. These results provide a way to utilize MRI data to understand the temperature profiles particular nanoparticle distributions produces.**

***Index Terms*—Iron Oxide Nanoparticles; Magnetic Hyperthermia; Intravenous Diffusion**

I. INTRODUCTION

IRON Oxide Nanoparticle (IONP) offer two advantages in cancer treatments: magnetic resonance imaging (MRI) and hyperthermia. Either is induced by IONPs depending on the magnetic field frequency and intensity regime. Experiments have extensively studied and optimized the process of hyperthermia [1-3]. However, it is important to augment experiments with theory and computational results, for such studies help elucidate unforeseen advantages [4-7]. Already simulations have provided a manner to effectively study scenarios that might otherwise be restricted financially and legally [8-11]. However, theory and simulations have yet to catch up to rate that experiments provide new information. It is important to augment experiments with theory and computational analysis.

This paper continues to build theory of IONP magnetically induced hyperthermia by studying how IONP distribution affects final temperature profiles. Two common methods of cancer drug and IONP penetration are compared: direct needle injection and intravenous diffusion. MRI gives doctors information regarding IONP distribution. The results from this study will then give doctors an understanding of what temperatures would result from inducing magnetic hyperthermia.

C. K. Koch is with the Engineering Science and Mechanics Department at Virginia Tech, Blacksburg, VA 24060 USA (e-mail: caleb.koch@vt.edu).

A. H. M. Casey is with the Chemical Engineering Department at Virginia Tech, Blacksburg, VA 24060 USA (e-mail: ahmc29vt.edu).

A. L. Winfrey is with the Nuclear Engineering Department at Virginia Tech, Blacksburg, VA 24060 USA (e-mail: leigh.winfrey@vt.edu).

II. METHODS

A general 2D method was developed in order to utilize a Finite Element Model (FEM) to discretize the consideration of IONP magnetic heating and study temperature profiles. Shown in (1) is the weak form, in rectangular coordinates, of the Heat Conduction Equation with the IONP heating term included,

$$\int_{\Omega^e}\left(\omega\left(\frac{1}{\alpha}\frac{\partial\theta}{\partial t}-P_{\text{input}}\right)+k\left(\frac{\partial\omega}{\partial x}\frac{\partial\theta}{\partial y}+\frac{\partial\omega}{\partial y}\frac{\partial\theta}{\partial y}+\right)\right)dx\,dy \\ -\frac{1}{k}\oint_{\Gamma^e}\left(\omega\left(\beta\theta+\hat{q}_n\right)\right)=0 \tag{1}$$

where $\alpha=\frac{k}{\rho c}$, k is the thermal conductivity of tissue (W/m^{0}C), ρ is the density of the tissue (kg/m^3), c is the specific heat of tissue (J/kg^{0}C), $\theta(x,y,t)$ describes the difference in temperature from the initial temperature, i.e. $\theta(x,y,t)=T(x,y,t)-T_0(x,y,0)$, c_b is the specific heat of blood (J/kg^{0}C), W_b is the blood perfusion rate (kg/m^3), and $P_{\text{input}}(x,y,t)$, Ω^e represents the area domain of each element, Γ^e represents the boundary of each element, and $\omega(x,y)$ represents the interpolation function. A full derivation and discussion of this model can be obtained in [1].

Two methods of introducing IONPs are modeled and considered in this paper: direct needle injection and intravenous diffusion. Direct needle injection is assumed to be diffused from the center of the tumor. General diffusion would result in a Gaussian IONP distribution profile, with the standard deviation growing as a function of time. The x and y position of each IONP is determined by a Gaussian probability function. As the number of IONPs approaches infinity, the heating function becomes a smooth Gaussian function.

Intravenous diffusion is modeled as IONPs diffusing into the tumor with equal weighting in radial directions. Once a random theta is determined, the radial position is determined by a normal distribution function with the mean located at the edge of the tumor. The increasing standard deviation values provide a way to model increasing time progressions of IONP

distribution. Early intravenous diffusion has the highest concentration at the edge, and as diffusion proceeds more IONPs enter the tumorous area.

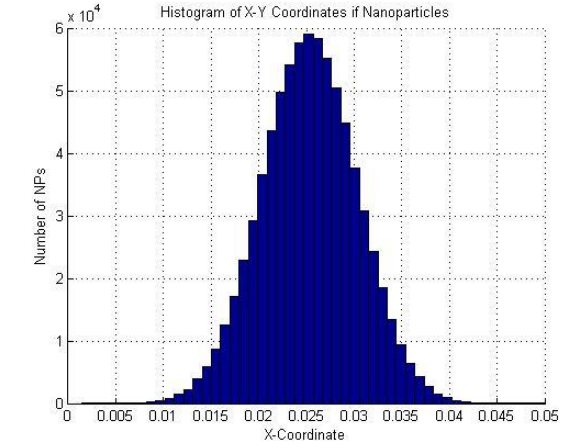

(a)

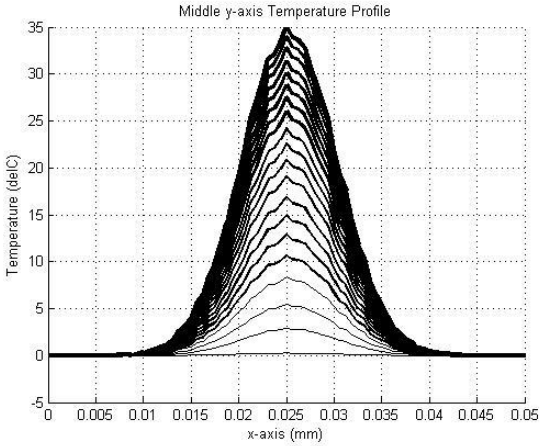

(b)

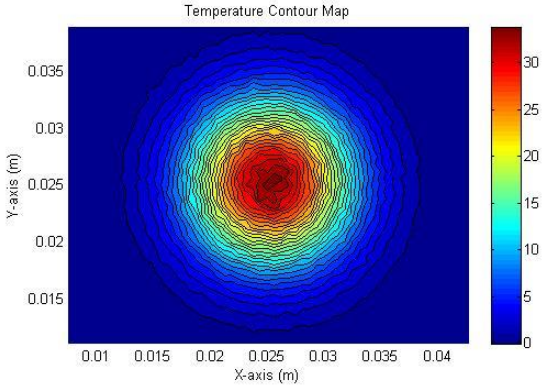

(c)

Fig. 1: IONP distributions and temperature contours resulting from direct-injection of IONPs into the tumor. (a) Histogram of IONP Gaussian distribution. (b) 150s increment time slices of temperature distribution. (c) Temperature contour plot.

III. Results and Discussion

Four cases were considered for this experiment. First magnetic hyperthermia is applied to a direction injection, Gaussian distribution, with 1σ equaling the radius of the tumor.

The discussion continues then with three cases of 4σ, 3.5σ, and 3σ to understand the results from hyperthermia due to intravenous diffusion, and to determine the most efficient manner in selectively heating tumors.

Gaussian Profile Temperature Profile

Direct needle injection of IONPs, released at the center of the tumor, results in diffusion that develops a Gaussian distribution profile from the release point. The deviation, or width of the Gaussian distribution is dependent on the time of injection. For this simulation assume a 1cm diameter spherical tumor, and the Gaussian distribution of IONPs is such that one standard deviation equals the radius of the tumor. Shown in Fig. 1.a a histogram of the distribution of IONPs is plotted. Note the tumor ranges between 0.02m and 0.03m. Fig. 1.b shows the temperature profile of the P_{norm} for consecutive 150s time slices. The distribution of IONPs is highly related to the final temperature profile distribution, for the temperature profile closely follows the shape of the distribution histogram. Lastly, Fig. 1.c is a contour plot of the simulation space.

This simulation is equivalent to Candeo 2009, with the only difference being a Gaussian IONP distribution was considered in the tumor rather than a homogeneous distribution. Asymmetry is present in this hyperthermia example, seem in the "hot spots" from Fig. 1.c and the only approximate Gaussian shape of Fig. 1.b. This result occurs because a finite number of IONPs is present rather than a heating function.

Known from Koch 2014 Gaussian IONP distributions are effective in efficiently and selectively heating tumors and not imposing long-lasting effects on healthy tissue. From these results a better foundation is established for understanding the consequences of radial-Gaussian IONP distribution functions.

Intravenous Diffusion Hyperthermia

For the next three cases intravenous diffusion is modeled for the IONP nanoparticle distribution. The three cases simulated were 4σ, 3.5σ, and 3σ all run with the same duration and time steps as the initial Gaussian distribution case.

The 4σ case represents very early stages of Intravenous Diffusion occurring. As modeled the highest IONP concentration occurs at the edge of the 1cm diameter tumor, depicted in the histogram in Fig. 2.a. Equal 150s time slices of the tumor temperature is shown in Fig. 2.b. Fig. 2.c plots the global temperature in the form of a contour plot. With the IONP count being 10 times larger on the tumor edge than the center, the temperature was 58 times larger on the edge than the center. The peak final temperature is 1.7 times larger than the peak temperature of the Gaussian profile distribution from Fig. 1. This results from a higher IONP concentration at the points of maximum temperature, but also the local density of these regions being higher. With the density of IONPs being so localized and focused on the edge little energy has time to dissipate during the 30min simulated magnetic treatment. During early stages of IONPs penetrating into the tumor, hyperthermia treatment would result in a radial-modal temperature profile, and follow the trend of the density of IONPs in the system. In this case, little heating occurred in the center, and certainly not enough to damage the center of the

tumor. Such heating also puts local healthy tissue at risk by having the temperature increased above 5^0C.

The next case is 3.5σ, which represents IONP penetration several time stages after the 4σ case. Again the histogram of IONP distribution, 150s equal time slices temperature profiles, and a global contour plot are plotted in Fig. 3.a, b, and c, respectively. Important to note is that in Fig. 3.c temperature asymmetry exists. "Hot spots" can be seen in dark red at different theta values.

This is because a finite number of IONPs were considered in order to make the simulation more realistic. In the middle of the tumor, or 0.025m on the x-axis of Fig. 3.a, the intravenous diffusion begins to develop another peak of concentration in the center of the tumor. In this case, the IONP count is 5.5 times larger on the edge than the center and only 10 times larger in final temperature. As the local density of IONPs decreases at the edge and diffuses into the enclosed tumor

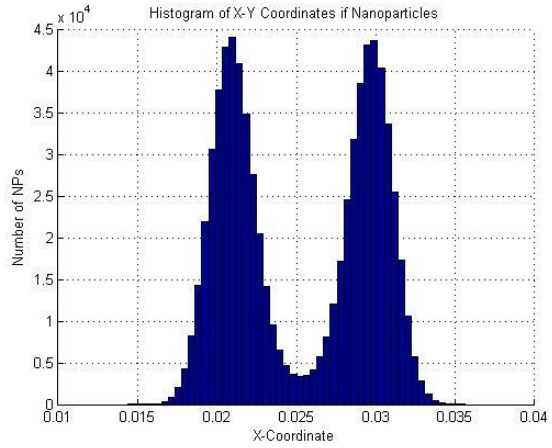

(a)

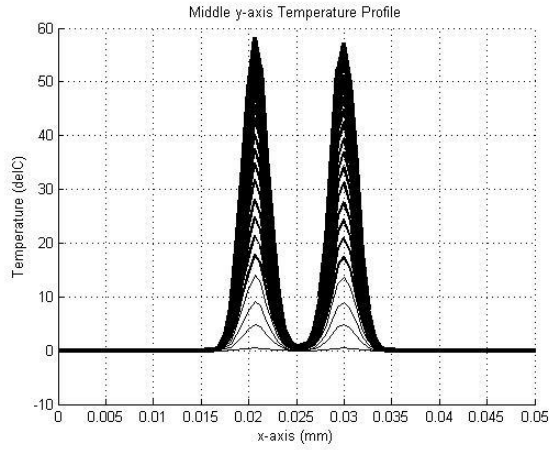

(b)

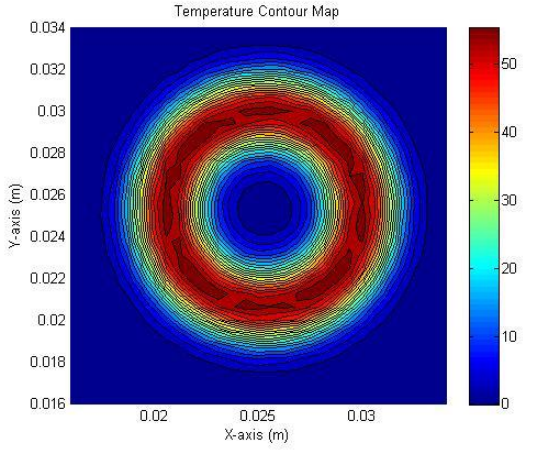

(c)

Fig. 2: Temperature distributions from beginning time steps of intravenous diffusion, σ=4. Results from early stages of intravenous diffusing of IONPs penetrating into tumor. (a) Histogram of IONP radial-modal distribution. (b) 150s increment time slices of temperature. (c) Temperature contour plot.

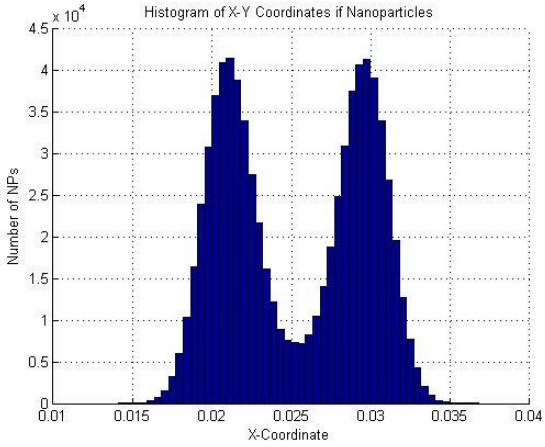

(a)

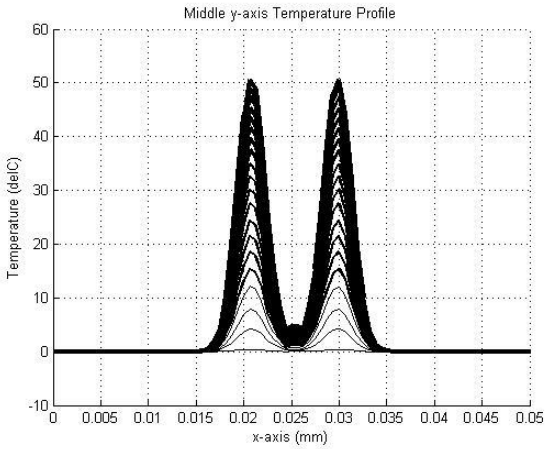

(b)

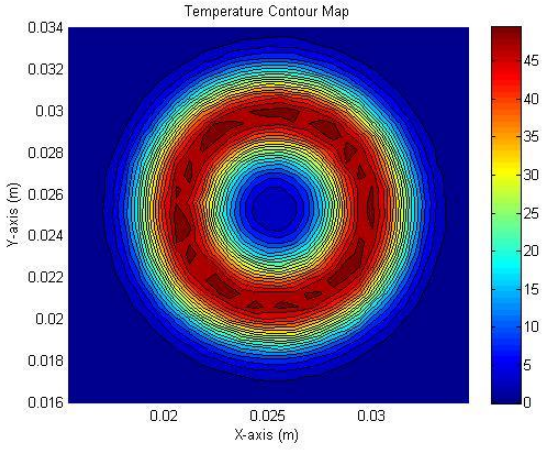

(c)

Fig. 3: Temperature distribution from intermediate time step of intravenous diffusion, σ=3.5. (a) Histogram of IONP radial-modal distribution. (b) 150s increment time slices of temperature. (c) Temperature contour plot.

region the temperature becomes further homogenized. The final temperature in the center of the tumor in this 3.5σ increased by 4^0C from the 4σ case. This is also seen in Fig. 3.b by the center of the tumor becoming a lighter blue.

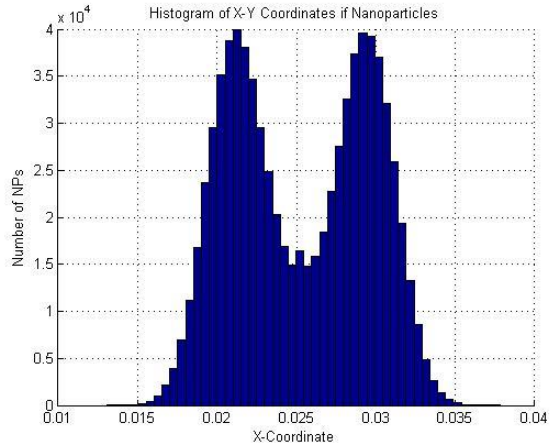

(a)

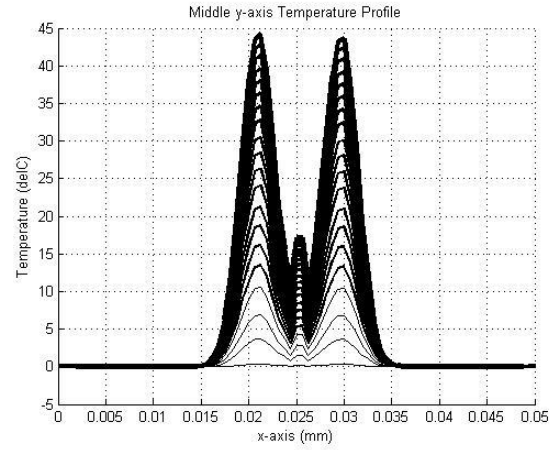

(b)

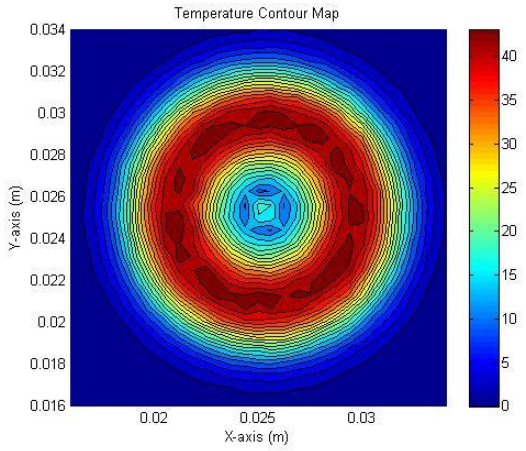

(c)

Fig. 4: Final time step of intravenous diffusion and the resulting temperature distributions, σ=3. (a) Histogram of IONP radial-modal distribution. (b) 150s increment time slices of temperature. (c) Temperature contour plot.

The 3σ results including the IONP histogram distribution, temperature time-slice profiles, and final temperature contour plot is shown in Fig. 4.a, b, and c, respectively. In this case the IONP concentration on the edge was only 2.5 times larger than the IONP concentration in the center of the tumor. The final temperature was 2.6 times larger than on the edge than the tumor. In order to keep healthy tissue from having its temperature increased by more than 5^0C the magnetic hyperthermia treatment would have needed to been stopped at 450s. However, 25% of the tumor would not have reached sufficient temperature in order to incur irreparable damage.

IV. Conclusion

Gaussian profiles provide the most effective manner to introduce selective heating to tumors. Such IONP distribution ensures heating selectivity in the tumor. Intravenous diffusion leads to doubt whether all intratumoral regions reach irreparable temperature damage. This FEM method provides doctors a method for relating IONP distribution data, obtained from MRI imaging, to temperature profiles from magnetic hyperthermia.

Much future works is still to be done in order to understand how distribution affects final hyperthermia states. For example, a sensitivity analysis needs to be done on how the concentration affects intravenous diffusion hyperthermia, and on how aggregation affects variability and intratumoral heating. Furthermore, superposition distribution functions, such as combined direct injection and intravenous diffusion, could lead to improved heating profiles.

V. References

[1] C. Koch, A. Casey and A. Winfrey, "FEM Theory for Finite Optimization," *IEEE Transactions on Magnetics*, vol. (Submitted for Review), 2014.

[2] C. Koch and A. Winfrey, "FEM Optimization of Energy Density in Tumor by using Time-Dependent Magnetic Nanoparticle Power Dissipation," *IEEE Transactions on Magnetics*, vol. Submitted for Review, 2014.

[3] C. Koch, A. Casey and L. Winfrey, "FEM Control," *IEEE Transactions on Magnetics*, p. Submitted for Review, 2014.

[4] C. Koch and A. Winfrey, "Theory on Aggregation Critical Variability," *IEEE Transactions on Magnetics*, p. Submitted for Review, 2014.

[5] A. Candeo and F. Dughiero, "Numerical FEM Models for the Planning of Magnetic Induction Hyperthermia Treatments with Nanoparticles," *IEEE Transactions on Magnetics*, vol. 45, no. 3, 2009.

[6] R. Xu, H. Yu, Y. Zhang, M. Ma, Z. Chen, C. Wang, G. Teng, J. Ma, X. Sun and N. Gu, "Three-Dimensional Model for Determining Inhomogeneous Thermal Dosage in a Liver Tumor During Arterial Embolization Hyperthermia Incorporating Magnetic Nanoparticles," *IEEE Transactions on Magnetics*, vol. 45, no. 8, 2009.

[7] W. Andra, C. d'Ambly, R. Hergt, I. Hilger and W. Kaiser, "Temperature Disbribution as Function of Time Around a Small Spherical Heat Source of Local Hyperthermia," *Journal of Magnetism and Magnetic Materials*, vol. 194, 1999.

[8] I. Hilger, R. Hiergeist, R. Hergt, K. Winnefeld, H. Schubert and W. Kaiser, "Thermal Ablation of Tumors Using Magnetic Nanoparticles: An In Vivo Feasibility Study," *Investigative Radiology*, vol. 37, no. 10, pp. 580-586, 2002.

[9] L. Lacroix, J. Carrey and M. Respaud, "A frequency-adjustable electromagnet for hyperthermia measurements on magnetic nanoparticles," vol. 79, 29 September 2008.

[10] M. Takeda, H. Tada, H. Higuchi and e. al., "In Vivo Single Molecular Imaging and Sentinel Node Navigation by Nanotechnology for Molecular Targeting Drug-Delivery Systems and Tailor-made Medicine," *Breast Cancer*, vol. 15, no. 2, pp. 145-152, 2008.

[11] S. Maenosono and S. Saita, "Theoretical Assessment of FePt Nanoparticles as Heating Elements for Magnetic Hyperthermia," *IEEE Transactions on Magnetics*, vol. 42, no. 6, 2006.

Chapter 6: Improving Nanoparticle Hyperthermia by Optimizing Location, Number of Injections, Heating Intensity, and Heating Distribution; Computational Study

Koch, Caleb[1]**; Winfrey, Leigh**[2]

[1]Engineering Science and Mechanics, Virginia Tech, Blacksburg, VA 24061
[2]Nuclear Engineering Program, Virginia Tech, Blacksburg, VA 24061

Corresponding Author Email: caleb.koch@vt.edu

Chapter 6 was submitted to the International Journal for Hyperthermia for review.

Abstract. Basic parameters of magnetic nanoparticle hyperthermia, including the number of nanoparticle injection sites, the location of each injection site, the heating intensity, and nanoparticle distribution can be used to improve the efficiency, effectiveness, and location-specificity, defined as minimizing heating energy leaking into surrounding healthy tissue while maximizing heating uniformity inside the tumor, in cancer treatment. These parameters are experimentally controllable and, therefore, may be used to optimize treatment. A major dilemma, however, lies in understanding the impact of each parameter given that they are all highly interdependent. This study examines the parameter of tumor shape classification, measured here by eccentricity, and relates it to optimizing the efficiency of hyperthermia. The results of the study show that the optimal injection location was 0.55-0.65 of the transverse diameter, where 0 is the center and 1 is the boundary of the tumor. This range of injection location optimizes all the eccentricity values considered in this study. Furthermore, when the number of injection sites was increased the heating efficiency eventually reaches a plateau where increasing injection sites beyond 5-8 injections does not improve heating efficiency. Additionally, the results presented here show that a nanoparticle distribution of 0.08 times the tumor transverse diameter optimizes the heating efficiency. The parameters outlined in this study, coupled with results from other work, can be used to optimize magnetic nanoparticle hyperthermia and guide experimental research studies on developing the feasibility of this cancer treatment option.

I. Introduction

Nanoparticles have been instrumental in taking the next step forward in modern cancer solutions. As early as the 1950's, scientists have been studying the self-inductive properties of magnetic nanoparticles [1] and continue to realize their potential for selective tumor hyperthermia treatments. Using magnetic nanoparticle hyperthermia alone successful treatments have been used for liver [2], breast [3, 4], and prostate cancer [5, 6]. In the past two decades, hyperthermia has become a more attractive treatment option because anti-cancer effects are enhanced when combined with chemical therapeutics. For example, tumors have been found to be more susceptible to cancer drugs after a mild hyperthermia treatment [7], drugs have been designed to be activated by heat release from magnetic nanoparticles [8], and drugs have been designed to target the heat shock protein 90 released by tumors after hyperthermia [9].

A great deal of effort has been invested into optimizing and controlling the hyperthermia process. Scientists found that heating intensity can be controlled through particle size, particle coating, magnetic field strength, and frequency [10, 11, 12, 13]. Furthermore, Koch et al. have shown that by relaxing the assumption of constant nanoparticle heat dissipation and allowing it to be time-dependent, hyperthermia treatment energy was better contained inside the tumor boundary and leakage energy to healthy tissue was minimized [62]. An important assumption made in most nanoparticle heating models is that a direct injection results in a Gaussian heating distribution. Experimentally, this was verified with the only prerequisite being a slow nanoparticle injection rate into the tumor [15, 16].

More parameters involved in the hyperthermia process, however, have yet to be optimized. Bagaria and Johnson [17] utilized a square error optimization scheme between tumor and neurosis temperature, and surrounding tissue and normal temperature to develop an optimization

scheme. The goal of their study was to optimize nanoparticle heating distributions and generate temperature profiles closely resembling ideal temperature profiles. However, as noticed by Salloum et al. [18], the heating function was modeled as a quadratic decaying function. The heating distribution obtained in this study was not ideal because the entire tumor region did not reach neurosis temperature. As a response, Salloum et al. [18] proposed a new optimization scheme that utilized multiple injections. He was able to accomplish minimal damage to healthy tissue while maximizing damage to tumors. In this study the number of injection sites was assumed; here we attempt to expand on the research of Salloum et al. and allow for a varying number of injection sites. Additionally, we investigate a variety of tumor shapes in order to provide new insight as to how injection sites relates to tumor shapes in general.

The objective of this study is to extend previous work and further generalize hyperthermia parameters including nanoparticle heating intensity, heating distribution, number of injection sites, and location of injection sites. The behavior of these parameters are taken into consideration and presented alongside a discussion of how they change with various tumor shapes.

A widely accepted method used by clinicians to classify tumor shape is eccentricity [19]; a number of examples of this classification in practice include esophageal cancer [20], breast cancer [21], colon cancer [22], and brain cancer [23]. A L^2-norm, similar to the optimization scheme used by Bagaria and Johnson [17], is the parameter defined in this study to determine if a heating distribution is optimal or not. Heating energy is considered through the duration of this study rather than temperature as it provided a better lens for gaining insight into the interplay of parameters than temperature. For example, from the energy perspective, the problem of containing nanoparticle heating energy inside the tumor boundary is more easily seen and

understood. For a series of heating distributions built from changing the four hyperthermia parameters, and continuing this for several eccentricity values, all results are compared against the ideal case of uniform heating energy in the tumor and no applied nanoparticle heat inputted into healthy tissue. From these results, a general understanding is discussed of how hyperthermia can be more location-specific and reliable by optimizing heating intensity, heating distribution, the number nanoparticle injection sites, and the location of each injection site.

II. Methods

Here we outline the problem analytically and provide a framework for how the problem was solved computationally. Definitions are provided regarding heating efficiency, tumor eccentricity, and theoretical optimal heating efficiency, and actual heating efficiency.

Analytical Description of Heating Efficiency

Theoretical Heating Function. Consider a two dimensional elliptical tumor area, Ω, with all cancerous tissue contained inside the tumor boundary, Γ. Further, define a theoretical optimal heating function, i.e. a heating shape over the area of the tumor that, as defined by hyperthermia practitioners, would be considered as optimal in eliminating the cancerous tissue. In the development of this function both heating intensity and shape must be considered. For the purposes of this study assumptions are made to define an optimal hyperthermia heating function. First, optimally, no heating should be allowed to spill into surrounding healthy tissue and all heating energy is contained within Γ. Second, heating should be uniform to ensure the treatment is homogenous, consistent, and predictable over the area of the tumor. Third, a heating threshold should be defined because too intense of a heating intensity would be disallowed by regulations. Given these requirements, a theoretical heating function is defined as (21),

$$\Pi\left(\vec{x}\right) = \begin{cases} \mathcal{H} & \text{if } x \in \Omega \\ 0 & \text{if } x \notin \Omega \end{cases} \tag{21}$$

where $\mathcal{H}$ is the desired heating intensity. A graphical depiction of this function is shown in Fig. 1. All the characteristics defined above as optimal are included in the function $\Pi\left(\vec{x}\right)$.

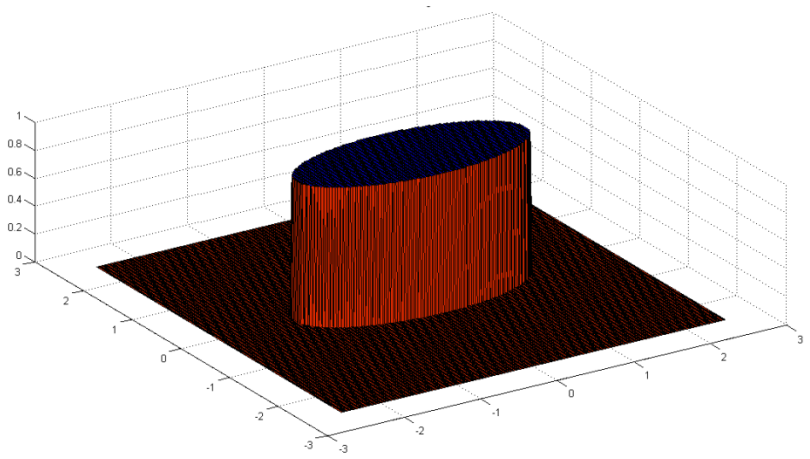

Fig. 1. Theoretical Optimal Heating Function, $\Pi(x,t)$

Realistic Heating Function. A realistic heating function must be built to define the heating functions associated with experimental nanoparticle injections inside a tumor. From literature and general diffusion principles it is known that after release from the needle tip location, nanoparticles will diffuse as a Gaussian function *[15]*. Each i^{th} injection will contribute a Gaussian heating profile. Therefore, the actual heating function, $\mathcal{A}(x,t)$, resulting from N injection sites equals the sum of all contributing heating profiles, as shown in (22),

$$\mathcal{A}(x,t) = \sum_{i=1}^{N} A_i(t)\text{Exp}\left(\frac{(x-x_{0_i})^2}{2{\sigma_i}^2} + \frac{(y-y_{0_i})^2}{2{\sigma_i}^2}\right) \tag{22}$$

where (x_{0_i}, y_{0_i}) is the center of the i^{th} injection site and σ_i is the standard deviation. A few assumptions are included in (22) that are important to mention. First, the heating intensity peak, $A_i(t)$, is not dependent on location, (x,y). This means each nanoparticle is modelled as contributing equal heating energy. Further, not allowing $A_i(t)$ to vary with location assumes a uniform magnetic field, which again reflects equal heating contribution from each nanoparticle.

The second assumption adds that $\sigma_{x_i} = \sigma_{y_i} = \sigma_i$. This employs the idea of spatial density homogeneity, such that when nanoparticles diffuse there are no deterrents in the x or y direction. The third assumption introduced is each injection site diffuses independently of each other and, therefore, linear superposition of Gaussian profiles allows for the construction of $\mathcal{A}(x,t)$ as shown in (22).

Heating Efficiency. The next step is to define heating efficiency and establish an infrastructure to compare different magnetic nanoparticle heating profiles. For the purposes of this study, utilizing the L^2-norm, which is the integral of the square difference between the theoretical and the actual heating function, was a useful means of comparing examples. L^2 is defined explicitly below in (23).

$$L^2 = \int_{\Omega} (\Pi(x,t) - \mathcal{A}(x,t))^2 \, d\Omega \tag{23}$$

This norm-parameter quantifies the excess/deficient energy in the system as related to the optimal energy distribution profile. The problem can be further formalized and understood through an analytical minimization process. Mathematically, minimizing means taking the partial derivative with respect to each parameter, c_j, and setting each j^{th} equation equal to zero. The process is shown below in (24).

$$\frac{\partial}{\partial c_j} \int_{\Omega} (\Pi(x,t) - \mathcal{A}(x,t))^2 \, d\Omega = 0 \tag{24}$$

Define Ξ as the healthy tissue area surrounding the tumorous tissue. Expand (24) by separating the contribution of the tumor and healthy tissue, which results in (25).

$$\int_{\Omega} \frac{\partial \mathcal{A}}{\partial c_j} (\Pi - \mathcal{A})\, d\Omega - \int_{\Xi} \frac{\partial \mathcal{A}}{\partial c_j} \mathcal{A}\, d\Xi = 0 \tag{25}$$

Equation (25) demonstrates the two factors affecting the minimization process conducted in this paper. First, shown in the second integral of (25), in the healthy tissue both the heating intensity of the magnetic nanoparticles, $\mathcal{A}$, and magnitude of difference constant c_j is from globally optimizing hyperthermia, as depicted by $\partial \mathcal{A} / \partial c_j$, contribute to optimizing hyperthermia parameters. Inside the tumor, shown in the first integral in (5), again the parameter derivative, $\partial \mathcal{A} / \partial c_j$, and the difference between the theoretical and actual heating intensity contribute to the global heating efficiency.

Computational Solution to Heating Efficiency Optimization Problem

This section outlines the computational procedure carried out to solve the location optimization problem. First, Eccentricity is defined to parameterize the shape of tumors. Next, an algorithm is developed to optimize the four parameters considered in this study: magnetic nanoparticle injection location, the location of each injection, magnetic nanoparticle distribution width, and heating intensity.

Tumor Eccentricity. A common characteristic used to define tumor shapes is eccentricity [19, 20, 21, 22, 23], as defined below in (26),

$$\mathcal{E} = \sqrt{1 - (b/a)^2} \tag{26}$$

where a = major tumor diameter and b = minor tumor diameter. For $\mathcal{E} = 0$ the tumor is spherical, and as $\mathcal{E}$ approaches 1 the tumor is more elliptical. Plotted below in Fig. 2 is the tumor shapes for 7 different $\mathcal{E}$ values.

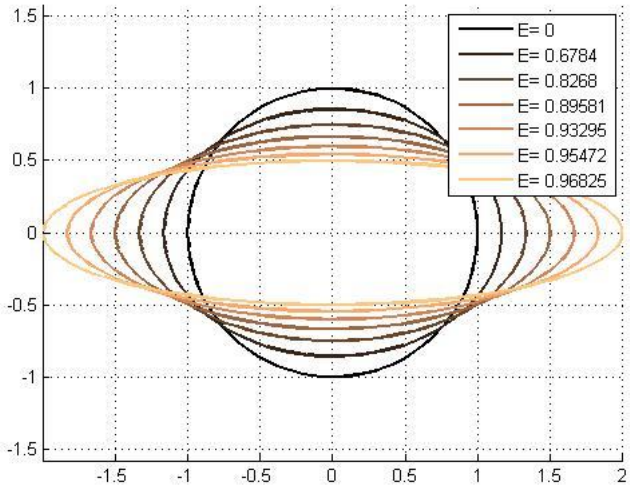

Fig. 2. Plot demonstrating shape of tumors with different values of $\mathcal{E}$

These are the 7 eccentricity values that will be considered here. Note for each $\mathcal{E}$ case a and b are scaled such that tumor area is held constant ($\Omega = \pi$). For each computational study the area of the tumor always equals the area of healthy tissue under consideration ($\Xi = \Omega = \pi$).

Computationally Computing L^2. An algorithm must be developed to computationally calculate L^2 as defined above in (23). An example of the computation is shown in Fig. 3. The theoretical heating function, $\Pi(x,t)$, is introduced, as was shown in Fig. 1.a. Over the entire simulation space the actual heating function, $\mathcal{A}(x,t)$, is then subtracted from $\Pi(x,t)$ and that value is squared, as shown in Fig. 3.b. The simulation area is then numerically integrated. The greater this computed L^2 value is the less efficient the heating treatment is, and inversely if L^2 equals zero the heating profile perfectly matches the optimal magnetic nanoparticle heating profile.

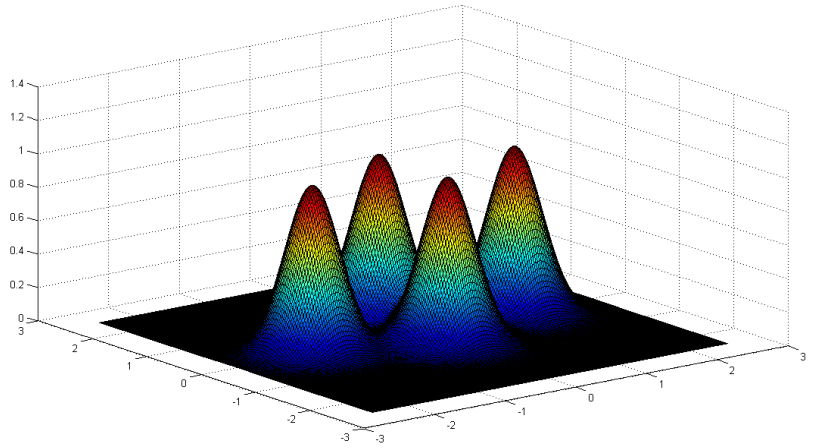

(a)

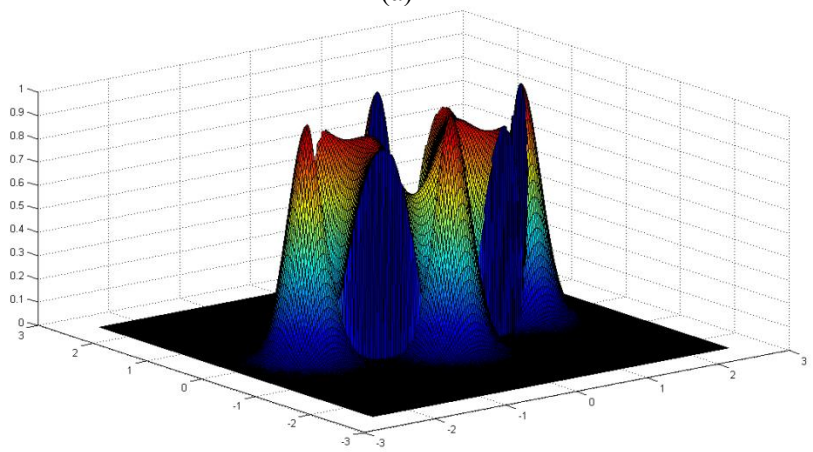

(b)

Fig. 3. Demonstration of L^2-norm calculation. (a) Actual Heating Function, $\mathcal{A}(\mathbf{x}, \mathbf{t})$, for 4 injection sties, injections located at boundary of tumor. (b) Square error map

III. Results and Discussion

This section presents the results, with discussion, on how the parameters including: the number of NP injections, location of NP injection sites, NP heating intensity, and NP heating distribution can be functionalized to optimize magnetic nanoparticle heating profiles inside tumors. The goal in designing heating patterns is decreasing energy leakage into healthy tissue, increasing heating uniformity, and achieving prescribed heating intensities.

Optimizing Number of and Location of NP Injection Sites

The first series of simulations was designed to determine the optimal number and location of NP injection sites. For each $\mathcal{E}$ the number of nanoparticle injection sites varied from 2-20. Injection sites were placed with equal angular spacing, such that 2 injection sites corresponded to $(0, \pi)$, 3 to $(0, 2\pi/3, 4\pi/3)$, etc. Finally, nanoparticle injection sites varied radially starting from the center to all injection sites at the tumor boundary.

The first simulation experiment considered constant nanoparticle heating intensity, A_i = 0.5, constant heating distribution, σ = 0.1, and constant theoretical heating intensity of $\mathcal{H} = 1$. Note, nanoparticle heating intensity has been scaled to the theoretical heating intensity, which means A_i = 0.5 is half of the desired final heating intensity, $\mathcal{H} = 1$. The distribution, σ, is also scaled with respect to the major axis of $\mathcal{E}$ = 0. Therefore, in this case, σ = 0.1 corresponds to 1/10th of the tumor diameter. The results are compiled and plotted in Fig. 4.

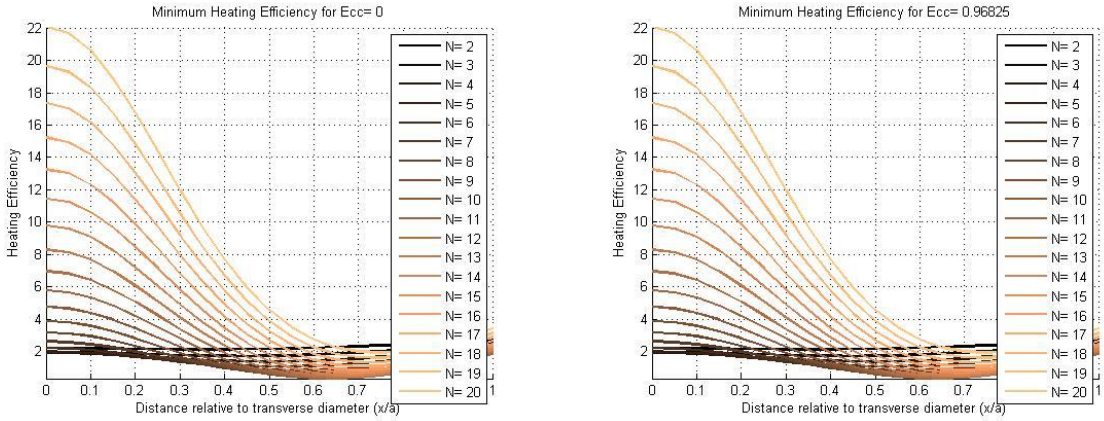

(a)

(b)

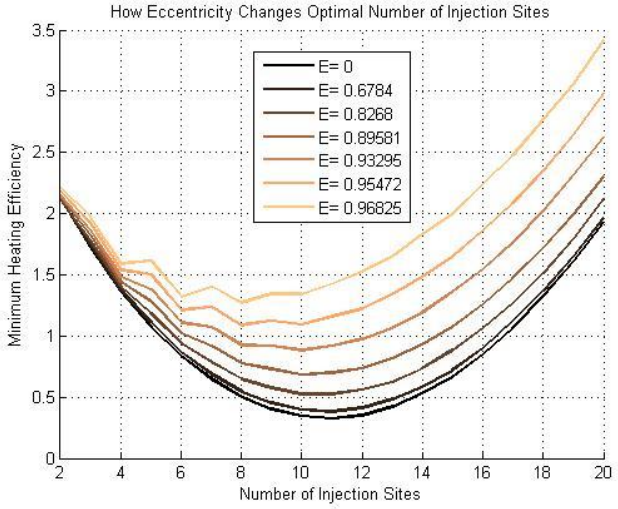

(c)

Fig. 4. Demonstrating the calculation of the optimal number of injection sites and optimal location of injections. (a) Minimum Heating Efficiency dependent on NP injection location for $\mathcal{E} = 0$ and (b) $\mathcal{E} = 0.98625$. (c) Optimal number of injection sites for all $\boldsymbol{\mathcal{E}}$ cases.

Fig. 4.a. is a plot of the L^2 values with increasing radial distance of the NP location sites for the $\mathcal{E} = 0$ case and Fig. 4.b. is a plot of the $\mathcal{E} = 0.96825$. Evid This is because a finite number of IONPs were considered in order to make the simulation more realistic. In the middle of the tumor, or 0.025m on the x-axis of Fig. 3.a, the intravenous diffusion begins to develop another peak of concentration in the center of the tumor. In this case, the IONP count is 5.5 times larger on the edge than the center and only 10 times larger in final temperature. As the local density of IONPs decreases at the edge and diffuses into the enclosed tumor ent in Fig. 4.a, having all the NP injection sites in the center of the tumor is never the best scenario,

especially as the number of injection sites increases. With increasing number of injection sites, the benefit to locating NP injection sites away from the center increases. From these plots a range of transverse diameter values, which is valid across all $\mathcal{E}$ cases, that optimizes the hyperthermia treatment is 0.55-0.65.

Fig. 4.c shows the minimum heating efficiency values for each curve in Fig. 4.a and for each $\mathcal{E}$ case. This graph then shows the minimum heating efficiency possible given an eccentricity and number of injection sites. For each $\mathcal{E}$ case, the optimal number of injection sites ranges between 8-11. These results are important for a hyperthermia practitioner because it provides them an understanding of how to plan a hyperthermia treatment in this limiting case. For this example, if a hyperthermia practitioner was limited to only one type of nanoparticle solution and one needle, these results would be important to guiding where to injection the nanoparticles and how many injections would optimize the treatment.

Optimizing Number of IONP Locations now keeping Heating Input Constant

One parameter not conserved in the previous consideration is the total energy applied to the system, which equals: $\text{Total Energy} = \sum_{i=1}^{N} 2\pi\sigma_i A_i = 2\pi N\sigma A$, if A_i and σ_i equal for each case. In order to keep this parameter constant, the next computational study scales the heating intensity accordingly: $A_i = 1/(2\sigma_i N_i)$. Introducing this scaling keeps energy constant between all cases. The same simulation conducted above is done again, and the results are plotted below in Fig. 5.

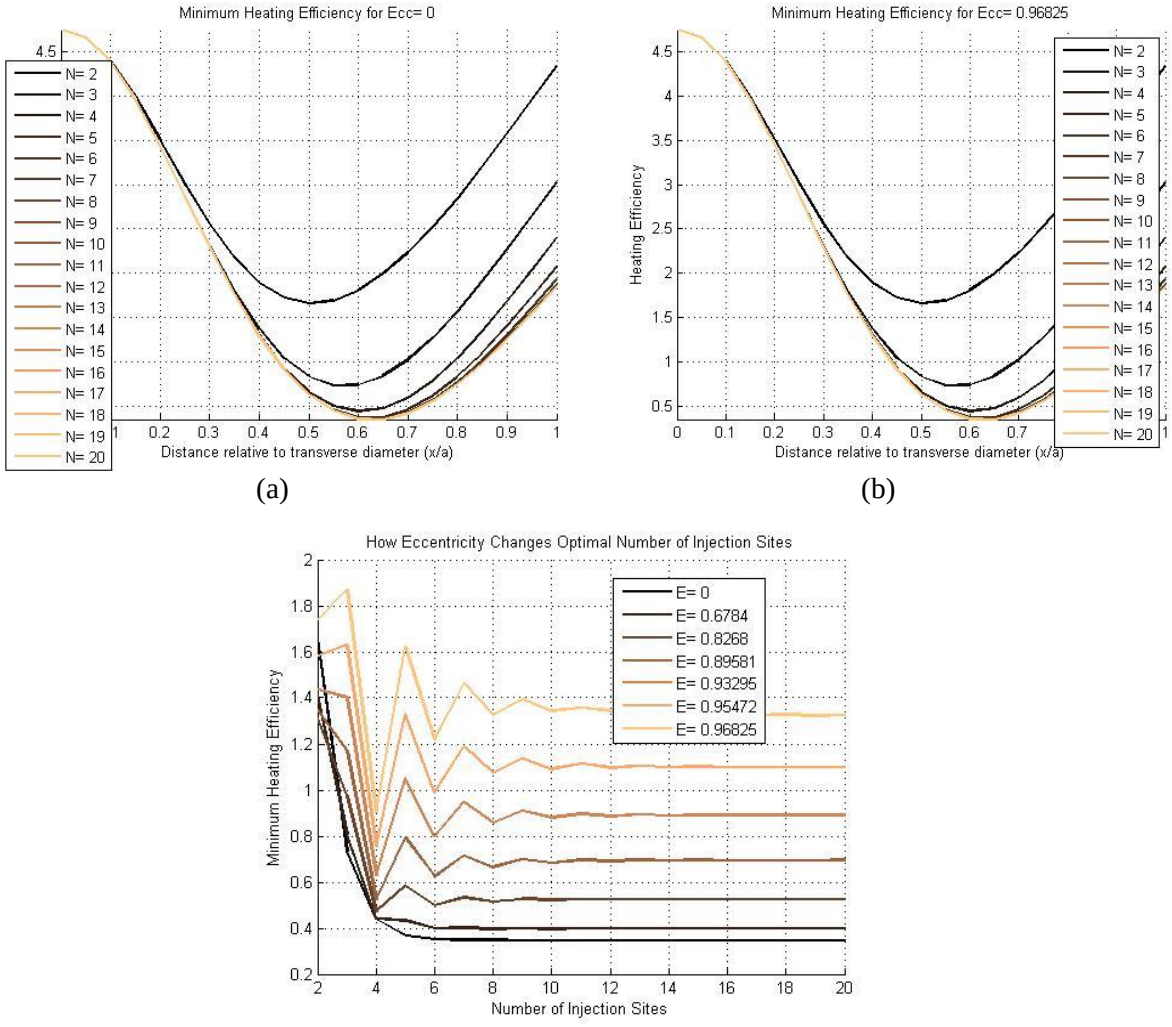

Fig. 5. Determining the optimal number of injection sites and location of injections for the case of constant energy. (a) Minimum Heating Efficiency dependent on NP injection location for $\mathcal{E} = 0$ and (b) $\mathcal{E} = 0.98625$. (c) Optimal number of injection sites for all $\boldsymbol{\mathcal{E}}$.

The same trend is observed in Fig. 5.a. as was observed in Fig. 4.a. The optimal location for all number injection sites again ranged between 0.55-0.65. By changing the location of injection sites, the heating becomes 9 times more efficient than if all injections were placed at the center. Also, notice significant improvements in heating efficiency are observed in Fig. 5.a. and Fig. 5.b between 2 and 3 and 4 injection sites as the line trends toward zero. Then, beyond 4, the figures do not demonstrate improvements in heating efficiency.

To further elucidate how the number of injection sites changes heating efficiency prospects, Fig. 5.c, was generated in the same manner as Fig. 4.c. For each eccentricity factor case, starting at 5-8 injection sites the minimum possible heating efficiency plateaus. Increasing the number of injection sites does not necessarily increase the heating efficiency. Also note in Fig. 5.c, the more spherical a tumor is, the more efficient the tumor treatment is, and in this case heating when $\mathcal{E} = 0$ is 3.5 times more efficient than when $\mathcal{E} = 0.96825$. Also note, in general, an even number of injections is better than an odd number of injections. This is because symmetry allows more the tumor area to be evenly heated. However, after the plateau phenomenon it is not relevant whether the number of injection sites is even or odd.

In summary, after 8 NP injections the heating efficiency is not improved. Furthermore, at a relative transverse distance of 0.5-0.65, given σ = 0.1, the nanoparticle heating distribution is optimized. In later sections the heating distribution will be optimized. However, for the present purposes, it is enough to verify that, in fact, heating does improve when injection sites are varied.

Optimizing Heating Distribution, σ

The heating distribution may, arguably, be the most important parameter to optimize. Thinking hypothetically, one would project that having small distributions with a high number of injection sites would be optimal. However, intuition was not corroborated by the results to follow.

For the first case considers the same parameters as the above simulation and again conserve total energy inputted into the system. For this computational experiment change the heating distribution width from σ = 0.1 to $\sigma = 0.2$. The same figure configuration is plotted below in Fig. 6.

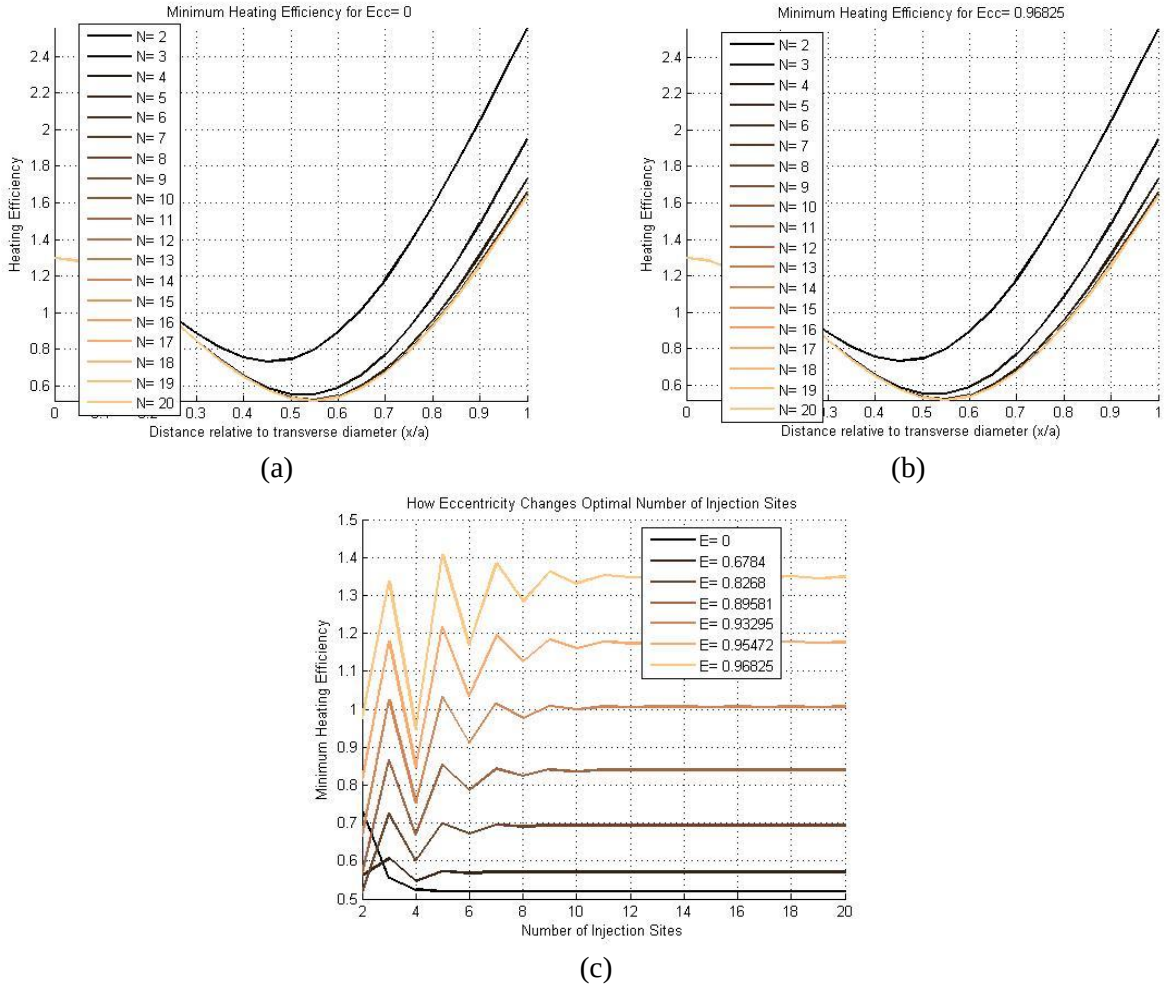

Fig. 6. Determining the optimal number of injection sites and location of injections for the case of constant energy, wide case. σ = 0.2. a) Minimum Heating Efficiency dependent on NP injection location for $\mathcal{E} = 0$ and (b) $\mathcal{E} = 0.98625$. (c) Optimal number of injection sites for all $\mathcal{E}$.

When the distribution is doubled a very different heating efficiency profile is observed in Fig. 6. For example, after the minimum heating efficiency is reached per number of injection sites in Fig. 6.a and 5.b, putting injection sites closer to the boundary increases heating efficiency much more so than for $\sigma = 0.1$. This is because with a wider distribution, heating energy leaks into healthy tissue more immediately than with a narrower distribution. Another observation in the similarity between $\sigma = 0.1$ and $\sigma = 0.2$ is in Fig. 6.c plateauing of heating efficiency occurs still at around 8 NPs.

In the next example, the distribution is halved to $\sigma = 0.05$. The same results are plotted below in Fig. 7. Again, very different heating efficiency profiles are observed. In Fig. 7.a and Fig. 7.b, for example, a smaller increase in heating efficiency happens toward the boundary than observed in Fig. 6.a and Fig. 6.b. Furthermore, in Fig. 7.c, significant improvement in heating efficiency is gained from increasing the number of injection sites; this trend was not observed for the wider heating distribution cases of $\sigma = 0.1$ and $\sigma = 0.2$.

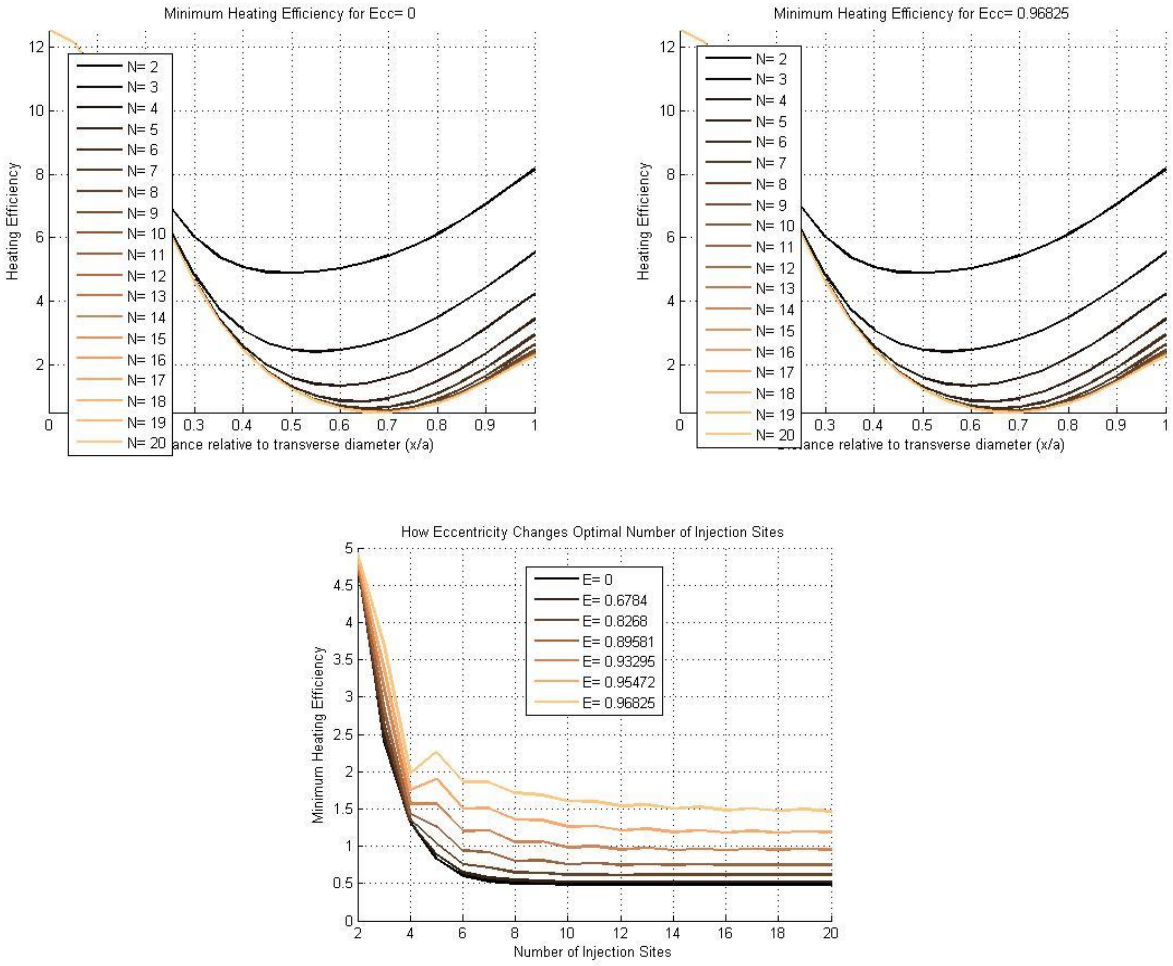

(c)

Fig. 7. Determining the optimal number of injection sites and location of injections for the case of constant energy, narrow case. σ = 0.05. a) Minimum Heating Efficiency dependent on NP injection location for $\mathcal{E} = 0$ and (b) $\mathcal{E} = 0.98625$. (c) Optimal number of injection sites for all $\mathcal{E}$.

The next step is to relate all the heating distribution cases and determine the optimal σ value. Several different σ cases were run as well as different $\mathcal{E}$ values. For each case the plateau heating efficiency was saved and utilized to compare each case. For the sake of this discussion, a lower plateau value corresponds to a more optimal case. The results are summarized in Fig. 8.

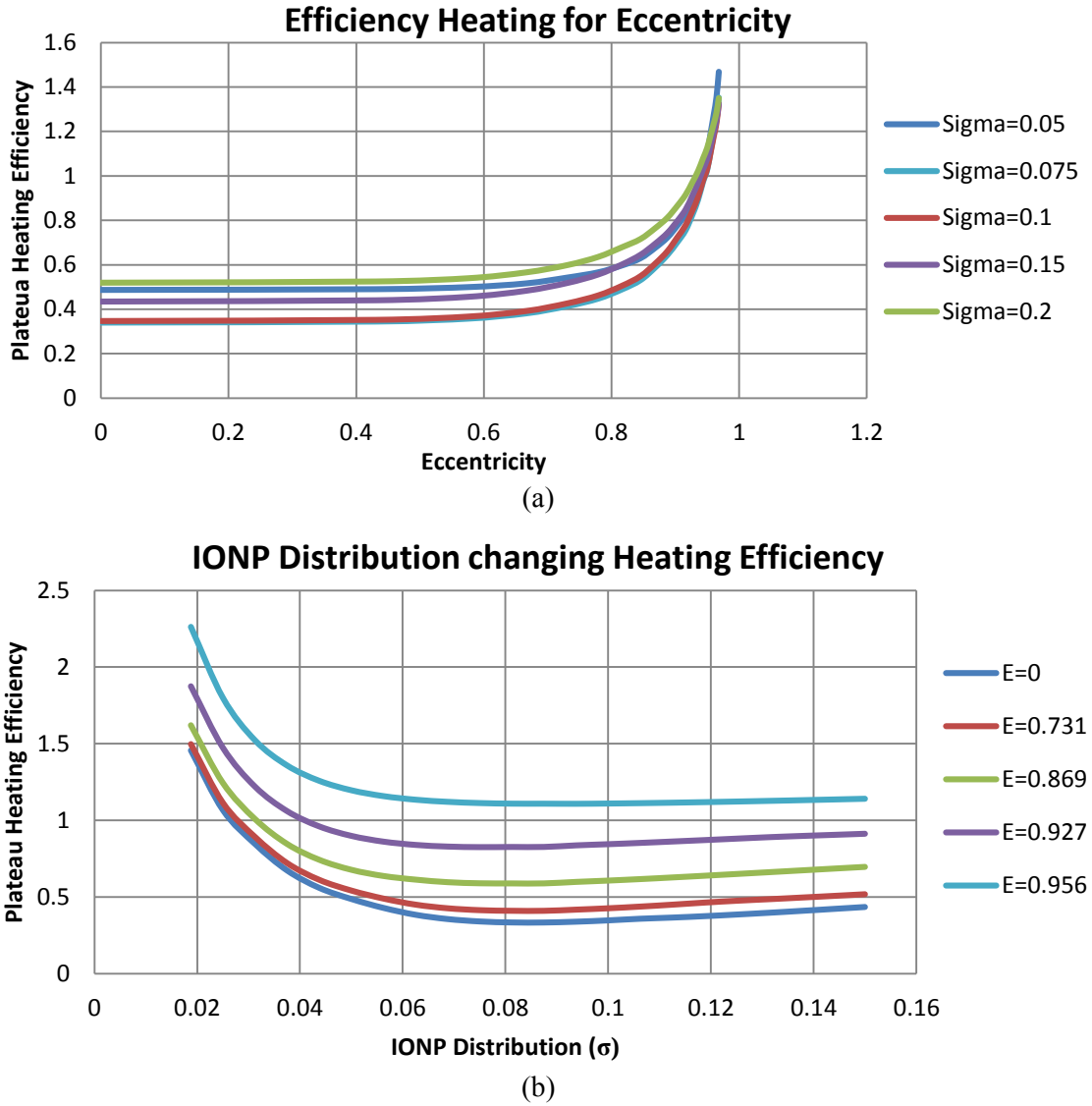

Fig. 8. Understanding how eccentricity factor and NP distribution can be optimized for hyperthermia treatments. (a) Plotting Eccentricity vs. Plateau Heating Efficiency for different distribution values. (b) plotting distribution vs. plateau heating efficiency for different Eccentricity Factor values.

Fig. 8.a. shows how the eccentricity changes the possibility of optimizing hyperthermia treatments. As the tumor converges toward becoming flatter and flatter, the prospects of improving heating efficiency increases exponentially to infinity. Interestingly, in Fig. 8.a. the lowest two heating efficiency lines are for $\sigma = 0.1$ and $\sigma = 0.075$. All other σ cases, both above and below 0.1 and 0.075, a lower heating efficiency cannot be achieved. This is further delineated in Fig. 8.b.

Fig. 8.b. plots the NP distribution spread vs. the plateau heating efficiency for different eccentricity factors. Counter to intuition, decreasing the heating distribution does not decrease the heating efficiency. Rather, if the distribution becomes too low then the hyperthermia treatment becomes exponentially farther away from the desired heating treatment. As the NP distribution increases, as seen in Fig. 8.b, the plateau heating efficiency again increases. This is because the distribution become too wide and heating energy leaks into the healthy tissue. An optimal NP distribution was found for each $\mathcal{E}$ ranging between 0.08-0.09. Therefore, the optimal NP heating distribution for a tumor with any eccentricity factor is between 0.08-0.09 of the transverse diameter.

IV. Conclusions

The objective of this study was to determine the optimal parameters involved in NP heat dissipation hyperthermia treatment. With regards to a cancer treatment, this study provides insight into some of the most basic questions such as how where to inject the NPs in the tumor, how many injections is best, based on the number of injections, and whether a wide or narrow NP distribution or narrow distribution is more effective for the treatment. These questions become difficult to address because they all have the same answer: it depends. Interdependencies between parameters make elucidating generalizations about how to design hyperthermia treatments. Nonetheless, using a computational study this study determines based on the tumor shape how all the parameters can independently thought of.

Eccentricity was used to characterize the tumor shape, which is used in various fields of oncology. Considering different tumor shapes allows the results to consider the geometrical dimension of cancer that many times is neglected.

The first general principle found was where to optimally injection NPs. Between 0.55-0.65 of the relative transverse diameter, scaled such that 0 is the center and 1 is the edge, for all eccentricity factors and in the range of optimal heating intensity and distributions heating efficiency was optimized. This was the location where heating didn't leak into the surrounding healthy tissue and at the same time was roughly uniform around the center of the tumor.

The second general principle found was that after 8 injection sites the heating efficiency did not improve, rather remained constant. 8 injection sites were just as efficient as 15 injection sites. This result demonstrates that a saturation point can be reach in improving heating efficiency by distributing heating energy to different injection sites. This plateau value was sometimes higher or lower than the heating due to 2 or 3 injection sites, depending on the NP distribution. Below 8

injection sites, even numbers of injection sites, 2, 4, and 6, were more advantageous than odd number of injection sites, 3, 5, and 7, because of symmetry.

The third general principle found is that the optimal NP distribution, measured as the standard deviation, to optimize heating is 0.08 of the transverse diameter. At this distribution spread energy in healthy tissue was minimized while energy uniformity inside the tumor was maximized. The corresponding heating intensity is found by scaling based on the desired heat dosage to be applied to the patient. Lastly, all spatial dimensions were nondimensionalized with respect to the major transverse diameter of the tumor. Therefore the results can be scaled based on the size of the tumor.

Based on these principles, a comprehensive hyperthermia treatment plan can be devised to optimize heating efficiency and improve the overall performance. In order to define an optimized treatment scheme, these results show that a practitioner should use 6 injection sites in a symmetric format. The injections should be located just over half the radial distance from the center to the boundary of the tumor. The injection rate of nanoparticles should be such that the final Gaussian width of the distribution is 0.08 the transverse diameter of the tumor. Finally, the heating intensity is dictated by the desired outcome from the hyperthermia treatment practitioner.

For future work, some assumptions can be relaxed that would give insight into further improving hyperthermia efficiency. First, efficiency can be improved if injection sites were allowed to have different heating intensities and distribution spreads. This would allow the treatment to be further tailored specific tumors. Second, allowing injection sites to be nonuniformly distributed around the tumor might allow for greater heating efficiency.

v. References

[1] R. Gilchrist, R. Medal, W. Shorey, R. Hanselman, J. Parrott and C. Taylor, "Selective inductive heating of lymph nodes," *Annals of Surgery,* vol. 146, pp. 596-606, 1957.

[2] H. Matsuki and T. Yanada, "Temperature sensitive amorphous magnetic flakes for intra-tissue hyperthermia," *Materail Science Engineering,* vol. 181, pp. 1366-1368, 1994.

[3] I. Hilger, R. Hergt and W. Kaiser, "Towards breast cancer treatment by magnetic heating," *Journal of Magnetic Materials,* vol. 293, pp. 314-319, 2005.

[4] I. Hilger, W. Andra, R. Hergt, R. Hiergeist, H. Schubert and W. Kaiser, "Electromagnetic heating of breast tumors in interventional radiology: In vitro and in vivo studies in human cadavers and mice," *Radiology,* vol. 218, no. 2, pp. 570-575, 2001.

[5] M. Johannsen, A. Jordan, R. Scholz, M. Koch, M. Lein, S. R. J. Deger, K. Jung and S. Loening, "Evaluation of magnetic fluid hyperthermia in a standard rat model of prostate cancer," *Journal of Endourology,* vol. 18, no. 5, pp. 495-500, 2004.

[6] M. Johannsen, B. Theisen, A. Jordan, K. Taymoorian, U. Gneveckow, N. Waldofner, R. Scholz, M. Koch, M. Lein and K. Jung, "Magnetic fluid hyperthermia (MFH) reduces prostate cancer growth in the orthotopic Dunning R3327 rat model," *Prostate,* vol. 64, pp. 283-292, 2005.

[7] C. Song, J. Chae, E. Choi, T. Hwang, C. Kim, B. Lim and H. Park, "Anti-cancer effect of bio-reductive drug beta-lapachon is enhanced by activating NQO1 with heat shock," *International Journal of Hyperthermia,* vol. 24, no. 2, pp. 161-169, 2008.

[8] D. Kim, D. Nikles, D. Johnson and C. Brazel, "Heat generation of aqueously dispersed CoFe2O4 nanoparticles as heating agents for magnetically activated drug delivery and hyperthermia," *Journal of Magnetism and Magnetic Materials,* vol. 320, no. 19, pp. 2390-2396, 2008.

[9] W. Xu and L. Neckers, "Targeting the Molecular Chaperone Heat Shock Protein 90 Provides a Multifaceted Effect on Diverse Cell Signaling Pathways of Cancer Cells," *Clinical Cancer Research,* vol. 13, no. 6, pp. 1625-1629, 2007.

[10] R. Hergt and W. Andra, "Physical Limits of Hyperthermia using Magnetic Fine Nanoparticles," *IEEE Transactions on Magnetics,* vol. 34, no. 5, pp. 3745-3754, 1998.

[11] R. Rosensweig, "Heating magnetic fluid with alternating magnetic field," *Journal of Magnetic Materials,* vol. 252, pp. 370-374, 2002.

[12] R. Hergt, R. Hiergeist, M. Zeisberger, G. Glockl, W. Weitschies, L. Ramirez, I. Hilger and W. Kaiser, "Enhancement of AC-losses of magnetic nanoparticles for heating applications," *Journal of Magnetic Materials,* vol. 280, pp. 358-368, 2004.

[13] J. Fortin, F. Gazeau and C. Wilhelm, "Intracellular heating of living cells through Neel relaxation of magnetic nanoparticles," *European Biophysics Journal,* vol. 37, no. 2, pp. 223-228, 2008.

[14] C. Koch and A. Winfrey, "FEM Optimization of Energy Density in Tumor by using Time-Dependent Magnetic Nanoparticle Power Dissipation," *IEEE Transactions on Magnetics,* 2014.

[15] M. Salloum, R. Ma, D. Weeks and L. Zhu, "Controlling nanoparticle delivery in

hyperthermia for cancer treatment: Experimental study in agarose gel," *International Journal of Hyperthermia,* vol. 24, no. 4, pp. 337-345, 2008.

[16] M. Salloum, M. R. and L. Zhu, "An in-vivo experimental study of temperature elevations in animal tissue during magnetic nanoparticle hyperthermia," *International Journal of Hyperthermia,* vol. 24, no. 7, pp. 589-601, 2008.

[17] H. Bagaria and D. Johnson, "Transient solution to the bioheat equation and optimization for magnetic fluid hyperthermia treatment," *International Journal of Hyperthermia,* vol. 21, no. 1, pp. 57-75, 2005.

[18] M. Salloum, R. Ma and L. Zhu, "Enhancement in treatment planning for magnetic nanoparticle hyperthermia: Optimization of the heat absorption patter," *International Journal of Hyperthermia,* vol. 25, no. 4, pp. 309-321, 2009.

[19] M. Mazumdar, A. Smith and L. Schwartz, "A statistical simulation study finds discordance between WHO criteria and RECIST guideline," *Journal of Clinical Epidemiology,* vol. 57, no. 4, pp. 358-365, 2004.

[20] L. Schwartz, J. Colville, M. Ginsburg, L. Wang, M. Mazumdar, J. Kalaigian, H. Hricak, D. Ilson and G. Schwartz, "Measuring tumor response and shape changes on CT: esophageal cancer as a paradigm," *Annals of Oncology,* vol. 17, pp. 1018-1023, 2006.

[21] D. Cascio, F. Fauci, R. Magro, G. Raso, R. Bellotti, F. DeCarlo, S. Tangaro, G. DeNunzio, M. Quarta, G. Forni, A. Lauria, E. Fantacci, A. Retico, G. Masala, P. Oliva, S. Bagnasco, S. Cheran and E. Torres, "Mammogram Segmentation by Contour Searching and Mass Lesions Classification with Neural Network," *IEEE Transactions on Nuclear Science,* vol. 53, no. 5, pp. 2827-2833, 2006.

[22] D. Marrinucci, K. Bethel, D. Lazar, J. Fisher, E. Huynh, P. Clark, R. Bruce, J. Nieva and P. Kuhn, "Cytomorphology of Circulating Colorectal Tumor Cells: A Small Case Series," *Journal of Oncology,* vol. 2010, 2010.

[23] E. Zacharaki, S. Wang, S. Chawla, D. Yoo, R. Wolf, E. Melhem and C. Davatzikos, "Classification of brain tumor type and grade using MRI texture and shape in a machine learning scheme," *Magnetic Resonance in Medicine,* vol. 62, no. 9, pp. 1609-1618, 2009.

Chapter 7: Theoretical Analysis of Magnetically Induced Iron Oxide Hyperthermia and Variability due to Aggregation

Koch, Caleb[1]**; Casey, Abigail**[2]**; Winfrey, Leigh**[3]

[1]Engineering Science and Mechanics, Virginia Tech, Blacksburg, VA 24061
[2]Material Science and Engineering, Virginia Tech, Blacksburg, VA 24061
[3]Nuclear Engineering Program, Virginia Tech, Blacksburg, VA 24061

Corresponding Author Email: caleb.koch@vt.edu

Chapter 7 is in preperation for submission to the International Journal for Hyperthermia.

Theoretical Analysis of Magnetically Induced Iron Oxide Hyperthermia and Variability due to Aggregation

Caleb M. Koch; Abigail, H.M. Casey; A. Leigh Winfrey, *Member, IEEE*

***Abstract*— This work develops a new theory to outline the implications aggregation of Iron Oxide Nanoparticle (IONP) has on nanoparticle hyperthermia treatments. Nanoparticle aggregation presents the most difficult constraint on the use of IONPs for use in Hyperthermia treatment. During aggregation, IONP distribution loses its uniformity and this produces inhomogeneous heating distributions, which is undesirable. Furthermore, researchers have not been able to quantify the unpredictability and variability and different severities of aggregation introduces to the hyperthermia treatment. In a 3D model, parameters were developed to define a 95% confidence interval of the expected thermal dosage tumor regions will receive during treatment. Six different regions of the tumor studied to determine how the different tumor regions are affected by aggregation. Found in this study, the boundary of the tumor is more susceptible to heating variability due to aggregation vs. the center of the tumor.**

In an extreme case of aggregation, the thermal dosage received at the edge of a tumor ranged from 1-10% of total energy inputted into system. However, as aggregation decreased the variability decreased and the upper and lower range of expected thermal dosage converged. Several IONP diameter and concentration scenarios were considered, and for all cases the theory shows that when the number of aggregates approaches a critical value and heating unpredictability of a tumor region grows exponentially. The aggregation theory presented in this study gives outlines for hyperthermia practitioners for understanding aggregation and when aggregation becomes unsafe for a patient.

***Index Terms*— Hyperthermia; Iron Oxide Nanoparticles; Aggregation**

I. Introduction

Iron Oxide Nanoparticles (IONP) and their multi-functionality have progressed the field of medicine in several ways. The first application IONPs were used for was imaging. By externally applying an approximately 3 Tesla and a 1-3MHz alternating magnetic field IONPs relax the oscillatory magnetic-moment energy in the form of light. Researchers have built detectors to capture this light, and coined this technology as MRI. In the field of medicine, MRI is used routinely to take non-invasive yet in vivo images of internal tissues [1, 2]. Secondly, IONPs function in the traditional manner, i.e. we think about iron being attracted to static magnetic fields. In the same way scientists have conjugated IONPs to chemotherapeutics and used static magnetic fields to increase its accumulation in the tumor [3, 4].

The third application is using IONPs to induce tumor hyperthermia. Decreasing the MRI magnetic fields to about 0.2 Tesla and 500kHz alternating results in the relaxation energy being released in the form of heat rather than light, a process also known as Néel relaxation [5, 6]. Scientists have worked for the past 30 years to fine-tune this heat release mechanism to achieve target-specific cancer treatments.

One of the natural yet difficult problems to deal with in IONP hyperthermia is aggregation. Magnetic fields of opposite polarity attract. Each IONP is a single magnetic dipole domain. From stochastic thermal perturbations these single domains from local IONPs will fluctuate in a manner that results in IONPs becoming attracted to each other, which leads to aggregating. Nanoparticles that were originally 2nm can build into aggregates of diameters from 20nm to 3microns [20]. In order to cope with this problem chemists have designed IONP fabrication methods to coat iron oxide with polymeric coatings to keep magnetic domains from getting too close and aggregating. Chan in 1993 [21] used lengthy polymer chains to keep IONPs from aggregating. However, he observed that any deficiencies resulted in aggregation, given that aggregates have intensified magnetic field attractions, which enhances the problem. More recently, Yallup and et al. [22] were interested in reducing the effects of aggregation. After IONPs were constructed they put them under hyperthermia conditions, allowed IONPs to aggregate, then centrifuged them to get the larger aggregates out, and siphoned off the good IONPs. Even by undergoing that process the system aggregation still occurred.

The IONP construct is not the only variable in aggregation. Lundqvist in 2008 [23] and Safi in 2010 [24] noticed that when citric acid molecules and poly(acrytic acid) polymer coatings around iron oxide and cerium oxide nanoparticles when serum proteins was present aggregation occurred tenfold from the original hydrodynamic diameter.

C. K. Koch is with the Engineering Science and Mechanics Department at Virginia Tech, Blacksburg, VA 24060 USA (e-mail: caleb.koch@vt.edu).

A. H. M. Casey is with the Chemical Engineering Department at Virginia Tech, Blacksburg, VA, 24060 USA (ahm29@vt.edu)

A. L. Winfrey is with the Nuclear Engineering Department at Virginia Tech, Blacksburg, VA 24060 USA (e-mail: leigh.winfrey@vt.edu).

Recently, Sadhukha in 2014 [25] studied what resulted if aggregation could be used despite the inhomogeneous temperature distributions. They were not able to quantify the unpredictability aggregation introduced to the system and proceeded with the hyperthermia treatment.

This study presents a new theory that first provides a framework for understanding nanoparticle aggregation, and applies the theory to quantify the unpredictability and variability for different severities of aggregation. A 95% confidence interval of expected heat dosage is defined for different tumor regions. These tumor regions are then related to their susceptibility to aggregation. Furthermore, as predicted by the theory, a critical aggregation value exists for nanoparticle diameter and concentration such that beyond that degree of aggregation variability grows exponentially. The results are discussed in application to hyperthermia practitioners the theory's implications for developing the feasibility of hyperthermia as a cancer treatment.

II. Methods

The initial equation utilized to develop the framework for the theoretical analysis is the general Heat Conduction Equation, shown in (27),

$$\frac{1}{\alpha}\frac{\partial}{\partial t}T\left(\vec{x},t\right)-\nabla^2 T\left(\vec{x},t\right)=H_{\mathrm{NP}}\left(\vec{x},t\right) \tag{27}$$

where $\alpha=\frac{k}{\rho c}$, k is the thermal conductivity of tissue (W/m^{0}C), ρ is the density of the tissue (kg/m^3), c is the specific heat of tissue (J/kg^{0}C), $T(\vec{x},t)$ is the temperature, and $H_{\mathrm{NP}}(\vec{x},t)$ is heating due to IONP power dissipation (W/m^3). The general method for developing a Finite Element Model (FEM) is multiplying the equation with an arbitrary weight function $\omega\left(\vec{x}\right)$, discretizing the simulation domain, and integrating over the area of each element, Ω^e. From this process (27) becomes

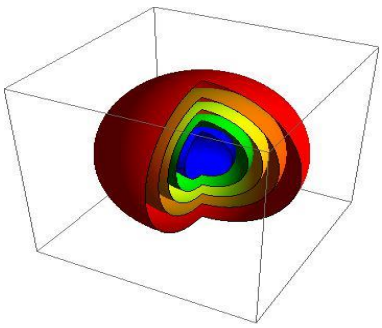

Figure 1. Different regions of the tumor that were compared to study how aggregation affects the unpredictability of hyperthermia treatments.

$$\int_{\Omega^e}\left(\omega\left(\frac{1}{\alpha}\frac{\partial T}{\partial t}-H_{\mathrm{NP}}\right)+\nabla\omega\cdot\nabla T\right)dx\,dy-\oint_{\Gamma^e}\omega\left(\vec{n}\cdot\nabla T\right)ds=0 \tag{28}$$

where Γ^e is the boundary of each element and $\vec{n}$ equals the vector on the boundary. Newton's Law of Cooling is utilized as the boundary condition, shown below in (29),

$$k\left(\vec{n}\cdot\nabla T\right)+\beta(T-T_0)=0 \tag{29}$$

where β is the convective constant and T_0 is the initial temperature. Because the first term of (29) matches with the boundary integral integrand of (28) we make the appropriate substitution, which produces (30).

$$\int_{\Omega^e}\left(\omega\left(\frac{1}{\alpha}\frac{\partial T}{\partial t}-H_{\mathrm{NP}}\right)+\nabla\omega\cdot\nabla T\right)dx\,dy+\frac{\beta}{k}\oint_{\Gamma^e}\omega(T-T_0)\,ds=0 \tag{30}$$

Above in (30) is the general term of the FEM that can be utilized to solve for temperature distribution of any simulation space and with arbitrary fineness of mesh.

The term in (30) that will be considered in the theoretical discussion of this study is the heating due to a finite number of IONPs, shown in (5) and written in fuller terms below.

$$H_{\mathrm{NP}}^{\mho}\left(\vec{x},t\right)=\sum_{i=1}^{j}\int_{\mho}\mathrm{NP}_i\left(\vec{x},t\right)\omega\left(\vec{x}\right)d\vec{x} \tag{31}$$

This term includes the information necessary for understanding how the aggregation of IONPs introduced variability and unpredictability to the system. The proceeding discussion focuses on developing a method for relating the concentration of IONPs and aggregation to increased risk for hyperthermia patients.

III. Results and Discussion

The discussion includes a theoretical development of a probability function that describes IONP distribution in a region based off of general diffusion starting from the center of the tumor, representing direct injection of IOPNs. After a spatial probability function is built for discretized IONPs, the function is related to thermal dosage for arbitrarily defined regions. Next, understanding the range of expected thermal dosage provides a means for relating aggregation of IONPs to variability and determining the aggregation that results in critical variability, which we define as unsafe and unpredictable hyperthermia behavior.

Derivation of Heat Dissipation from Finite Nanoparticles

The $H_{\mathrm{NP}}\left(\vec{x},t\right)$ term from (31) is the term that will be analyzed here. In this term is the spatial distribution, temporal development of the IONPs thermal effect on healthy versus cancerous tissue.

In order to further understand the implications of this term the distribution of nanoparticles in a system must be discretized. By not considering the location and size of each nanoparticle one loses effects due to variation. Considering the size and location of nanoparticles is especially important when nanoparticles aggregate. In this situation the total number of nanoparticles, or IONP aggregates, greatly affect the unpredictability of temperature distribution.

To develop a theoretical understanding of the variability of temperature distribution based on aggregation, we consider the probability of the x-value of the i^{th} nanoparticle's position, P_{x_i}, shown below in (32),

$$P_{x_i}(x_i,x_0,\sigma_x)=\frac{1}{\sigma_x\sqrt{2\pi}}\mathrm{Exp}\left(-\left(\frac{(x-x_0)^2}{2{\sigma_x}^2}\right)\right) \tag{32}$$

where x_0= the center of the Gaussian Distribution and σ_x= the standard deviation of distribution. It follows that in 3D the probability an IONP will have a particular location that equals (33).

$$P\left(P_{x_i}\cap P_{y_i}\cap P_{z_i}\right)= \frac{1}{\sigma_x\sigma_y\sigma_z(2\pi)^{3/2}}\mathrm{Exp}[-(\frac{(x-x_0)^2}{2{\sigma_x}^2}+\frac{(y-y_0)^2}{2{\sigma_y}^2}+\frac{(z-z_0)^2}{2{\sigma_z}^2})] \tag{33}$$

It is important to note that $\int_{\mathbb{R}}P(P_{x_i}\cap P_{y_i}\cap P_{z_i})\,d\vec{x}=1$, for a nanoparticle has to have a (x,y,z) position in the domain of the system. The $P(P_{x_i}\cap P_{y_i}\cap P_{z_i})$ function can be used to build the $H_{\mathrm{NP}}(\vec{x},t)$ function.

Define a three dimensional region $\mho=\{(\xi,\eta,\zeta)\rightarrow[x_1,x_2]\times[y_1,y_2]\times[z_1,z_2]\}$. The probability of a nanoparticle being in the region $\mho$ equals

$$\begin{aligned}P(\mho)&=P\left(P_\xi\cap P_\eta\cap P_\zeta\right)\\&=\frac{1}{\sigma_x\sigma_y\sigma_z(2\pi)^{3/2}}\int_{z_1}^{z_2}\int_{y_1}^{y_2}\int_{x_1}^{x_2}\left(\mathrm{Exp}\left(-\left(\frac{x^2}{2{\sigma_x}^2}+\frac{y^2}{2{\sigma_y}^2}+\frac{z^2}{2{\sigma_z}^2}\right)\right)\right)dx\,dy\,dz\end{aligned} \tag{34}$$

Carrying out the integral in (34), the probability of the i^{th} particle occurring in the region $\mho$ equals

$$P_i(\mho)=P_i\left(P_\xi\cap P_\eta\cap P_\zeta\right)=\frac{1}{8}\left(\mathrm{Erf}\left[\frac{x_2}{\sigma_x\sqrt{2}}\right]-\mathrm{Erf}\left[\frac{x_1}{\sigma_x\sqrt{2}}\right]\right)\left(\mathrm{Erf}\left[\frac{y_2}{\sigma_x\sqrt{2}}\right]-\mathrm{Erf}\left[\frac{y_1}{\sigma_x\sqrt{2}}\right]\right)\left(\mathrm{Erf}\left[\frac{z_2}{\sigma_x\sqrt{2}}\right]-\mathrm{Erf}\left[\frac{z_1}{\sigma_x\sqrt{2}}\right]\right) \tag{35}$$

where $\mathrm{Erf}(\cdot)$ is the error function.

The next step in the discussion is moving from considering any i^{th} IONP aggregate and expanding to considering the probability of m numberof IONP aggregates out of a total n in the system. Making the step of discussing m aggregates will allow for the global phenomenon of aggregation and its varying degrees of unpredictability to be quantified. Thus, again considering the arbitrary region $\mho$, the probability of m IONP aggregates out of a total n occurring in $\mho$ is shown below in (36),

$$\begin{aligned}P_\mho^*(m,n,P_\mho)&=C_m^n[P_\mho]^m[1-P_\mho]^{n-m}\\&=\frac{n!}{m!\,(n-m)!}[P_\mho]^m[1-P_\mho]^{n-m}\end{aligned} \tag{36}$$

where $P_\xi=\frac{1}{2}(\mathrm{Erf}\left[\frac{x_2}{\sigma_x\sqrt{2}}\right]-\mathrm{Erf}\left[\frac{x_1}{\sigma_x\sqrt{2}}\right])$ and C_m^n is the combinations symbol.

Equation (36) is an analytical expression that quantifies the variability of heating dosage due to aggregation. However, the order of magnitude of quantity of IONPs in the system and the resulting factorial calculations makes (36) an equation not implementable computationally. Therefore, introduce Sterling's factorial approximation, shown below in (37).

$$\begin{aligned}\ln(n!)&=n\ln(n)-n+\mathcal{O}(\ln(n))\\n!&\sim\sqrt{2\pi n}\left(\frac{n}{e}\right)^n\end{aligned} \tag{37}$$

In the regime of n values discussed in this study the order of error, $\mathcal{O}(\ln(n))$, is minimal. Using (37) to approximate (36) the final equation can be written below in

$$\begin{aligned}&P_\mho^*(n,m,P_\mho)\\&=\sqrt{\frac{n}{2\pi m(n-m)}}\left(\left(\frac{n(1-P_\mho)}{n-m}\right)^n\left(\frac{(n-m)P_\mho}{m(1-P_\mho)}\right)^m\right)\end{aligned} \tag{38}$$

Above in (38) is the analytical expression to determine the number of expected aggregates in an arbitrarily defined tumor region $\mho$. This equation is written generally so that Gaussian profiles are not the only type of profiles within the scope of possible calculations. For example, if multiple injection sites are used for hyperthermia treatments then $P_i(\mho)$ from (35) can be modified to account for the superimposed Gaussian profiles.

B. Expected Probability Plots of IONP Aggregates

The next step is to delve into the implications and predictive power of (38). Begin with the assumption that the tumor is a 3D symmetric spherical tumor. Furthermore, assume IONPs were injected in the center of the tumor. It is valid to model

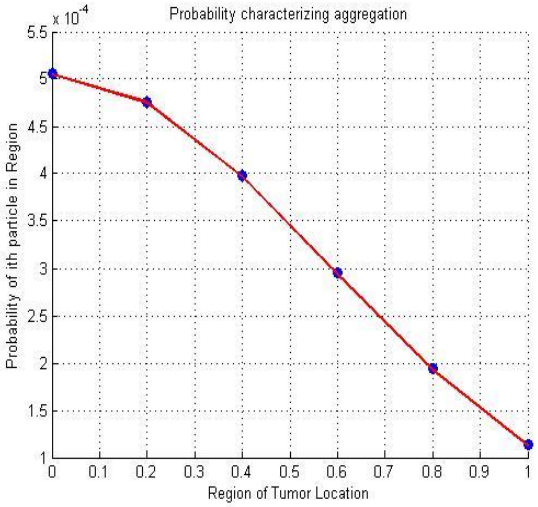

Figure 2. Probability of any i^{th} IONP being located $\pm 0.1\ \sigma_{x,y,z}$ from the center point. Each point represents a region of the tumor under consideration for this study.

the IONP distribution as a Gaussian function, which was experimentally verified by Salloum et al. [7]. Furthermore, assume the distribution is spread is such that the healty tissue-tumor boundary and the $1\sigma_{x,y,z}$ Gaussian distribution line coincide.

One of the variables of interest for this study is how different tumor regions respond to aggregation and the variability aggregation introduces. Therefore, define tumor

regions with width $0.2\sigma_{x,y,z}$ of the Gaussian distribution. Because of the assumption of Gaussian IONP distributions coinciding with the tumor boundary, the (-0.1,0.1), short for ($-0.1\sigma_{x,y,z}$,$0.1\sigma_{x,y,z}$) region represents the center of the tumor and (0.9,1.1) represents the boundary between tumorous and healthy tissue. Below in Figure 1 is the tumor is shown with the different slices representing the different regions considered. In the actual study only a 3D rectangular section was considered rather than the entirety of the spherical slice.

Equation (35) from the discussion above tells the

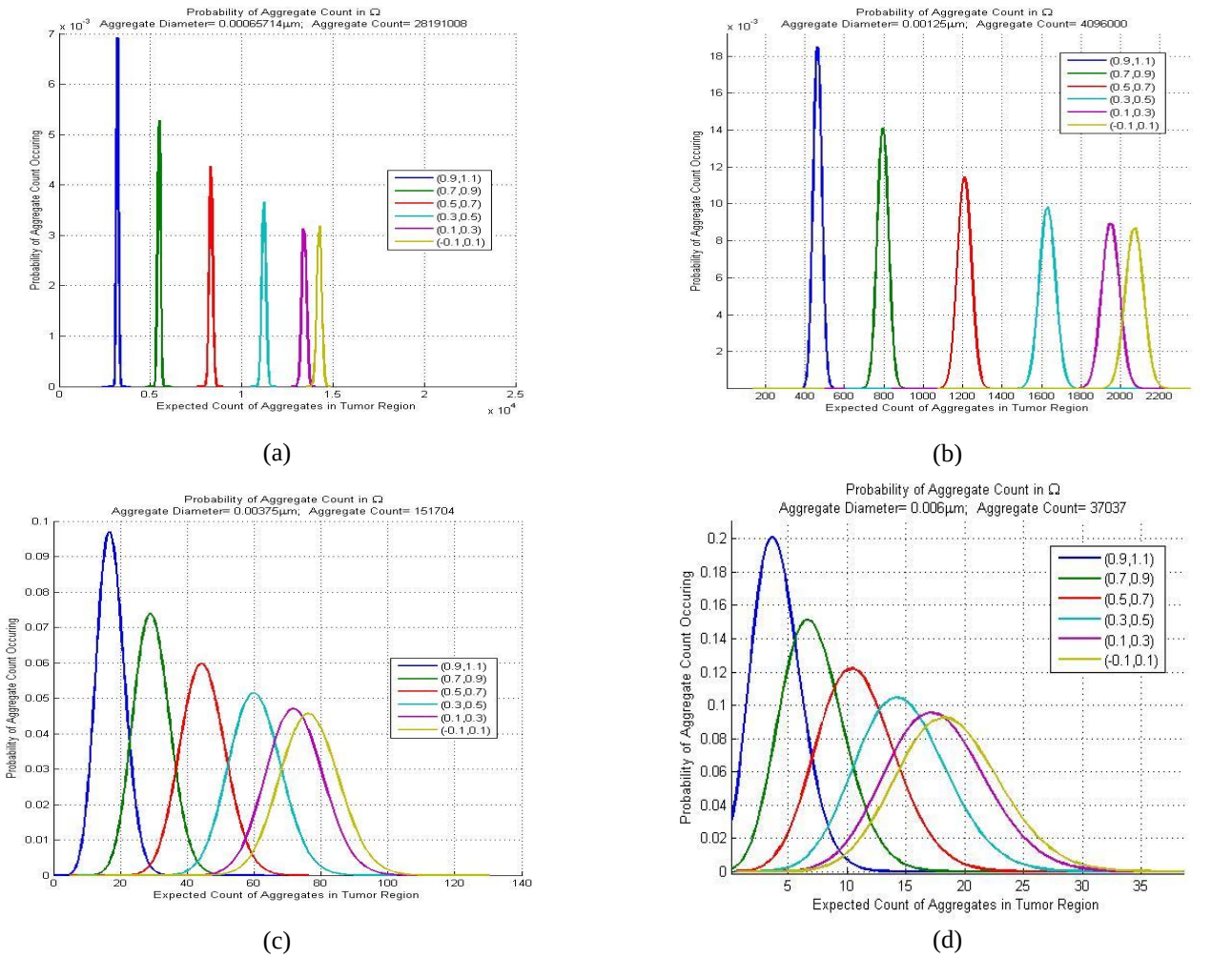

(a) (b)

(c) (d)

Figure 3. Expected aggregate counts for different aggregation severities. (a) diameter = 0.6nm (b) diameter = 1.25nm (c) diameter = 3.75nm (d) diameter = 6nm

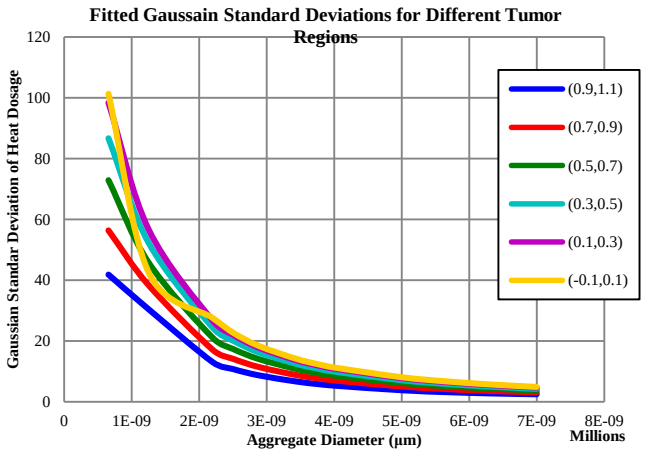

(a)

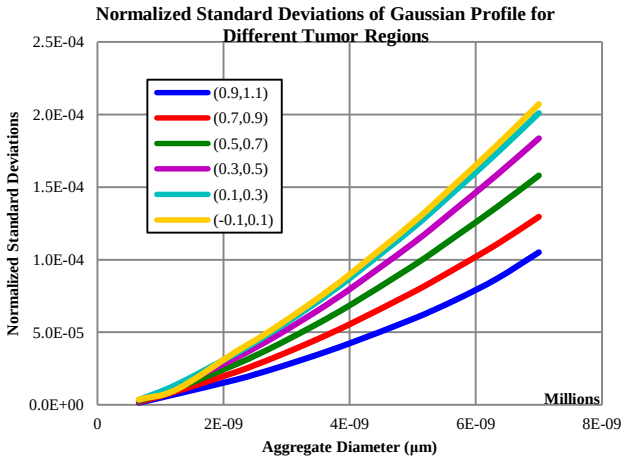

(b)

Figure 4. Standard Deviation of fitted Gaussian profiles plotted against aggregate diameter. (a) Non-normalized standard deviation. (b) normalized standard deviation.

probability of any i^{th} IONP aggregate occurring in the different specified regions. Shown below in *Figure 2* the probability is plotted for each tumor region, where the blue dot represents the center of the tumor region while it extends $\pm 0.1\,\sigma_{x,y,z}$ in each of the three dimensions. The trend in *Figure 2* follows a Gaussian profile, which results from the influence of the initial premise that IONPs and its aggregates are distributed in a Gaussian profile.

C. Relationship between IONP Probability function and Heating Function

Following from the derivation discussion, the next step is to explicate the predicting power and consequences of (38).

Begin by considering a case that initially 10 billion IONPs were injected into a tumor that has the same distribution characteristics as specified above. Conservation of IONP volume is held when considering all aggregate cases. This means that the number of aggregates and the diameter of the aggregate are scaled so that the total volume of aggregates is always equal. For four different aggregates cases: 0.6nm, 1.25nm, 3.75nm, and 6nm the probability of m aggregates occurring in the six different defined tumor regions out of a total available n is plotted below in Figure 4.

In Figure 3 going from (a) to (d) the diameter of the aggregates increases, and consequently the number of available aggregates decreases. The total aggregate count and aggregate diameter are shown at the top of the each plot. Though the peaks in *Figure 3* have the widest range of possible aggregates, with respect to the total available aggregates the peaks are narrower when compared to the more extreme cases of aggregation. Moving to cases (b), (c), and (d) as the severity of aggregation increase the peaks become wider and wider, with respect to the number of available number of aggregates. This begins to demonstrate the increased variability aggregation introduces to hyperthermia: as aggregation increase, the expected aggregate count becomes more unpredictable, as normalized to the total available aggregates

In Figure 3, each peak can be fitted to a Gaussian profile with a correlation factor of 0.985 or above. Form the fitted Gaussian profile the standard deviation characterizes the width of the peaks, i.e. the variability introduced by the different degrees of aggregation. Standard deviations are compiled for different aggregate diameter cases and plotted below in Figure 4.a for the non-normalized standard deviation and Figure 4.b normalized to the total number of available aggregates.

Figure 4.a, by neglecting the number of available aggregates, does not elucidate the variability of aggregation. However, by normalizing to n, Figure 4.b demonstrates the profile of unpredictability due to aggregation. As the aggregate diameter increase, the width of the fitted Gaussian profile exponentially increases. This trend is true for all tumor regions with the only difference being the rate of increased variability. The center of the tumor's, (-0.1, 0.1), normalized range of expected aggregates grows at a faster rate than any other region. This means the center of the tumor is more susceptible to aggregation tan other regions. The boundary of the tumor, region (0.9, 1.1), is the least susceptible to aggregation, for the width of the expected aggregate count peak grows at the smallest rate.

The expected aggregate count also sheds light on the variability of heating dosage applied to region $\mho$. The total heating of an element with domain $\mho$ due to n number of IONPS can be written as shown below in (39),

$$H_{\text{NP}}^{\mho}(\vec{x},t) = \sum_{i=1}^{n} \int_{\mho} \text{NP}_i(\vec{x},t)\omega(\vec{x})\, d\vec{x} \tag{39}$$

where $\text{NP}_i(\vec{x},t)$ provides the heating amplitude and spatial location of each i^{th} IONP. If an IONP is not in the domain of $\mho$ then it will not contribute to the $H_{\text{NP}}^{\mho}$ function. If the

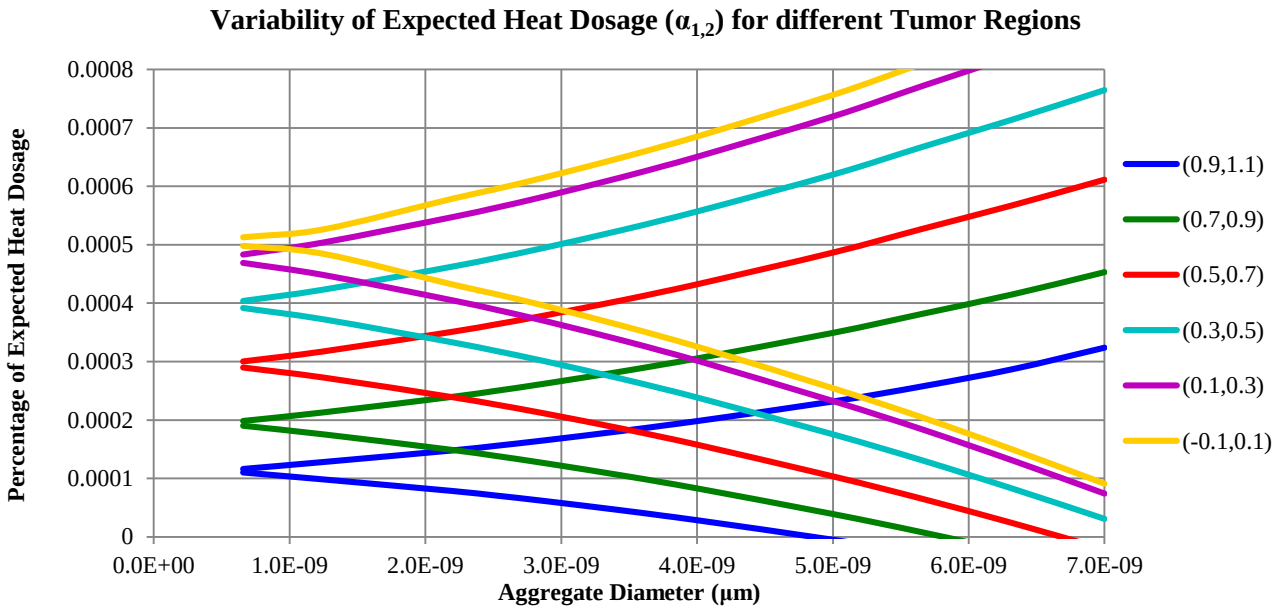

Figure 5. 95% confidence intervals of expected heat dosage to region $\mho$ for different tumor regions.

assumption is made that IONPs do not experience net motion during the duration of magnetic treatment then the time-dependent amplitude of heating can be separated from the spatial location of the IONP, which is explicitly shown in (40).

$$\mathrm{NP}_i\left(\vec{x},t\right) = A(t)S_i\left(\vec{x}\right) \tag{40}$$

Note that $A(t)$ does not have an i^{th} index because of the assumption that the applied magnetic field is uniform in the region of consideration, therefore the contribution of energy for each i^{th} IONP is equal.

One of the benefits to fitting the peaks in *Figure 3* to Gaussian profiles with a high correlation factor is a confidence interval can be defined for the expected number of aggregates in region $\mho$. Therefore, define j as the true number of IONPs in the region of $\mho$. As stated above, j can be written with 95% certainty between the range of $j \epsilon [\alpha_1, \alpha_2]$. The heating function can therefore be written as shown below in (41).

$$H_{\mathrm{NP}}^{\mho}\left(\vec{x},t\right) = A(t)\sum_{i=1}^{\mathrm{j}\epsilon[\alpha_1,\alpha_2]}\int_{\mho} S_i(\vec{x})\omega(\vec{x})\,d\vec{x} \tag{41}$$

Equation (41) provides a method to relate the number of IONPs in the system to the expected variation of heating, which correlates to the variation of temperature.

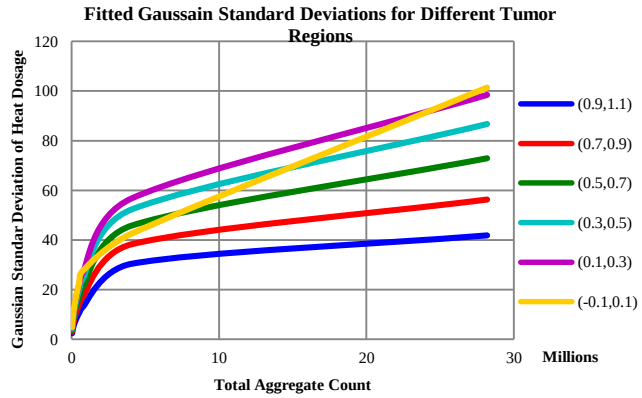

(a)

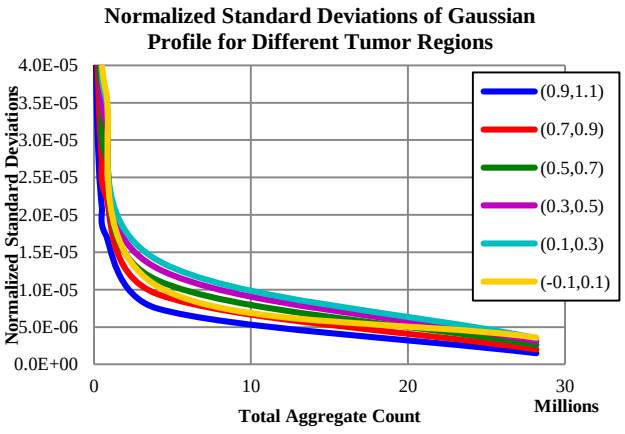

(b)

Figure 6. Standard Deviations of fitted Gaussian profiles to aggregate counts plotted against total aggregate count. (a) non-normalized standard deviation. (b) normalized standard deviation.

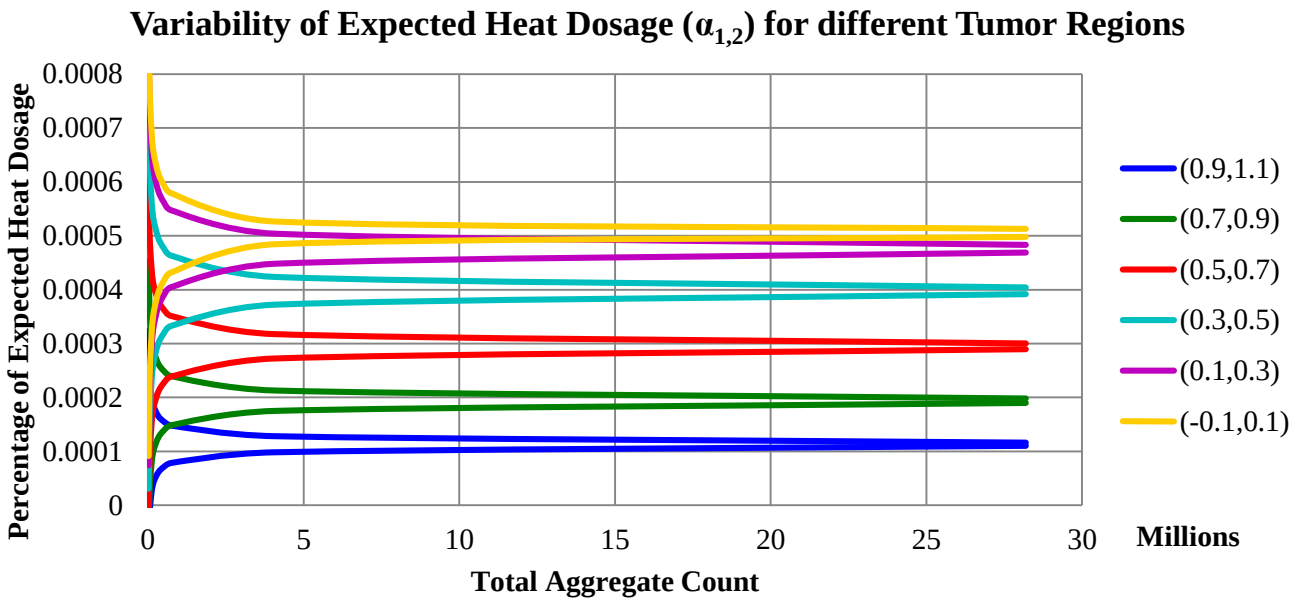

Figure 7. Expected heat dosage based on the total available aggregate count with a 99% confidence interval.

To further consider how aggregation relates to applied heat dosage assume that the region $\mho$ is sufficiently small such that the spatial contribution of heating for each IONP is independent of its location in $\mho$. Therefore (41) may be simplified to

$$H_{\mathrm{NP}}^{\mho}\left(\vec{x},t\right) = A(t)P_{\xi}^{*}(n,j)P_{\eta}^{*}(n,j)P_{\zeta}^{*}(n,j)V_{\mathrm{NP}}\int_{\mho}\omega\left(\vec{x}\right)d\vec{x} \tag{42}$$

where V_{NP}= the volume of a single IONP. Each aggregate contributed a portion of the total heat dosage applied to the system. Therefore, normalizing the aggregate's applied heat dosage to tumor region $\mho$ by the total heat dosage applied to the tumor region we posit that a 95% confidence interval can be defined for the expected heat dosage. For the 9 different regions considered in this study the results are plotted below in Figure 5.

For each color corresponding to different tumor regions, the space between the same color is the 95% confidence interval of expected heat dosage applied to region $\mho$. Moving right on the x-axis of Figure 5, increasing the aggregate diameter is equivalent to increasing the severity of aggregation. As the severity of aggregation increases the 95% confidence interval exponentially increases, a trend observed previously in Figure 4.b.

Observing the results plotted against aggregate diameter does not fully reveal the emergent unpredictability aggregation introduces to hyperthermia treatments. To further elucidate the consequences of aggregation, plot the non-normalized and normalized standard deviation against total aggregate count, which is shown below in Figure 6. Furthermore, the 95% confidence interval of expected heat dosage applied to tumor region $\mho$ is plotted below in Figure 7.

Shown in Figure 6, a stark shift in tumor heating occurs at roughly 4 million IONPs. Previous to that shift, even with small degrees of aggregation expected heat dosage was a narrow profile, as observed in Figure 7. However, after a critical point, aggregation results in an unpredictable heat dosage that grows at an unprecedented rate.

Using this theoretical assessment an understanding can be developed concerning the variability of hyperthermia for certain areas of tumorous regions due to aggregation. From knowing the variability of heat dosage at important areas the safety of the patient can be better considered.

IV. Conclusions

This work presents a new theory that provides a framework of understanding nanoparticle hyperthermia and the implications this phenomenon has for hyperthermia cancer treatments. Aggregation is a prominent problem in arguing the feasibility of nanoparticle hyperthermia, and the unpredictability aggregation introduces to the system has yet to be quantified. The new aggregation theory defines a 95% confidence interval of expected heat dosage for arbitrary tumor regions. For hyperthermia practitioners this allows them to know based on real-time diameter measures of nanoparticle aggregates the expected heat dosage. A feature inherent to nanoparticle diameter and concentration is at a critical aggregate diameter the variability of expected heat dosage increases exponentially. Beyond this critical aggregate diameter hyperthermia is too unpredictable and the treatment is unsafe for the patient.

In observing aggregate diameter increase, this study considered only beginning stages of aggregation. An initial diameter of 2nm was considered up to 12.5nm of aggregate diameter, and an initial diameter of 10nm was considered up

to 60nm. A critical aggregate diameter was highlighted as a defining feature of the changing physics of aggregation. Beyond 12.5nm and 60nm the expected heating profiles lose their Gaussian peaks and transform into other nonlinear profiles. Future work would include a rigorous analysis of these different expected heat dosage profiles and elucidating the implications regimes of greater aggregation has on hyperthermia treatments.

Other future studies would include including a sensitivity analysis for understanding how initial diameter and concentration change the critical aggregation diameter. Furthermore, this theory allows one to understand how different nanoparticle distribution profiles from multiple injection sites could mitigate the effects of aggregation.

V. References

[1] J. Bulte and D. Kraitchman, "Iron Oxide MR Contrast Agents for Molecular and Cellular Imaging.," *NMR in Biomedicine,* vol. 17, 2004.

[2] R. Weissleder, A. Bogdanov, E. Neuwelt and M. Papisov, "Long-Circulating Iron Oxides for MR Imaging," *Advanced Drug Delivery Reviews,* vol. 16, no. 2, pp. 321-334, 1995.

[3] T. Yoon, J. Kim, B. Kim, K. Yu, M. Cho and J. Lee, "Multifunctional Nanoparticles Possessing a "Magnetic Motor Effect" for Drug or Gene Delivery," *Angewandte Chemie,* vol. 117, no. 7, pp. 1092-1095, 2005.

[4] V. Kalambur, B. Han, B. Hammer, T. Shield and J. Bischof, "In vitro characterization of movement, heating, and visualization of magnetic nanoparticles for biomedical applications," *Nanotechnology,* vol. 16, no. 1221, 2005.

[5] R. Hergt, S. Dutz and M. Zeisberger, "Validity limits of the Neel relaxation model of magnetic nanoparticles for hyperthermia," *Nanotechnology,* vol. 21, no. 1, 2010.

[6] R. Hergt and W. Andra, "Physical Limits of Hyperthermia using Magnetic Fine Nanoparticles," *IEEE Transactions on Magnetics,* vol. 34, no. 5, pp. 3745-3754, 1998.

[7] M. Baalousha, "Aggregation and disaggregation of iron oxide nanoparticles: Influence of particle concentration, ph and natural organic matter," *Science of the Total Environment,* vol. 407, no. 6, pp. 2093-2101, 2009.

[8] D. Chan, D. Kirpotin and P. Bunn, "Synthesis and evaluation of colloidal magnetic iron oxides for the site-specific radiofrequency-induced hyperthermia of cancer," *Journal of Magnetism and Magnetic Materials,* vol. 122, pp. 374-378, 1993.

[9] M. Yallapu, S. Othman, E. Curtis, G. Gupta, M. Jaggi and S. Chauhan, "Multi-functional magnetic nanoparticles for magnetic resonance imaging and cancer therapy," *Biomaterials,* vol. 32, pp. 1890-1905, 2011.

[10] M. Lundqvist, J. Stigler, G. Elia, I. Lynch, T. Cedervall and K. Dawson, "Nanoparticle Size and Surface Properties Determine the Protein Corona with Possible Implications for Biological Impacts," *PNAS,* vol. 105, no. 38, pp. 14265-14270, 2008.

[11] M. Safi, H. Sarrouj, N. Mignet and J. Berret, "Interactions between sub- 10- nm Iron and Cerium Oxide Nanoparticles and 3T3 Fibroblasts: the Role of the Coating and Aggregation State," *Nanotechnology,* vol. 21, 2010.

[12] T. Sadhukha, T. Wiedmann and J. Panyam, "Enhancing Therapeutic Efficacy through Designed Aggregation of Nanoparticles," *Biomaterials,* vol. 35, pp. 7860-7869, 2014.

[13] M. Salloum, R. Ma, D. Weeks and L. Zhu, "Controlling nanoparticle delivery in hyperthermia for cancer treatment: Experimental study in agarose gel," *International Journal of Hyperthermia,* vol. 24, no. 4, pp. 337-345, 2008.

Chapter 8: Conclusions

Koch, Caleb[1]

[1]Engineering Science and Mechanics, Virginia Tech, Blacksburg, VA 24061

Corresponding Author Email: caleb.koch@vt.edu

This research focused on improving nanoparticle hyperthermia from many different perspectives. Each study within this work contributes to the field of nanoparticle hyperthermia by optimizing different factors of hyperthermia, discussing new distribution profiles, or introducing new theories. While assumptions are made in each study in order to ensure the problem was solvable, the resulting general principles derived are useful for understanding IONP hyperthermia and developing treatments.

The first study contributes to optimizing hyperthermia by relaxing the assumption of constant heat dissipation and demonstrates the advantage of allowing IONPs to dissipate heat at varying intensities. The applied magnetic fields dictate the heating intensity of nanoparticles. Therefore, as outlined in this study, doctors can increase the target-specificity of IONP heat treatments by using magnetic fields to change heating intensities of IONPs during the treatment. First, the higher the heating intensity the more the energy density is contained inside the tumor rather than leaking to healthy tissue. Second, putting heating intensity at the end of the treatment time improves target-specificity. Lastly, the duration of maximum IONP heating intensity is not as important as the magnitude of the IONP heating.

The second study contributes to the field of hyperthermia by demonstrating magnetic fields can be used to change IONP heating intensity during the treatment to control tumor and healthy tissue temperatures. Optimal temperature profiles are obtained in the previous study. This takes the next step by maintaining the temperature profile through time by changing the IONP heating intensity. Furthermore, this study contributes by outlining cost-benefits of different IONP heating intensities. For a more benign tumor, if metastasis is a concern, slower heating intensities may be beneficial. For a more volatile tumor, if the objective is to quickly

eliminate the tumor, higher heating intensities are necessary. This study shows that after a certain heating intensity, treatment time does not benefit by further increasing IONP heating intensity. Therefore, with respect to treatment time, it is not worth overheating a patient.

The third study contributes to hyperthermia treatments by discussing the consequences of introducing IONPs to a tumor via capillary diffusion. This type of IONP distribution has not been discussed in the field of hyperthermia; only direct injection distributions have been considered. Capillary diffusion has the advantage, vs. direct injection, of introducing energy to the tumor boundary. Alone introducing IONPs through capillaries is not sufficient for hyperthermia treatment. However, combined with direct injection the temperature distribution is made more homogenous throughout the tumor.

In the previous three studies a Finite Element (FE) model was used to solve for the temperature profiles. However, a few assumptions were made that might change the results of each study. First, the density of the tumor was considered homogenous when in reality the density is higher in the center and converges to the density of normal tissue. Second, temperature-dependent blood perfusion cooling was neglected. The two assumptions would change the temperature profile shapes of the previous three studies. However, the general principles of using magnetic fields to optimize hyperthermia, control hyperthermia, and capillary diffusion distributions do not change.

The fourth study contributes to the field of hyperthermia by optimizing four non-time domain parameters: the number of IONP injections, the location of each injection, the IONP distribution spread of each injection, and the heating intensity. Multiple injections are able to obtain a more homogenous temperature distribution than a single injection in the center. If

multiple injections are used, then should be injected in a symmetric manner at 0.55-0.65 the distance between the center and boundary of the tumor. An IONP distribution of 0.08x the tumor diameter is optimal for obtaining a homogenous temperature distribution. An even number of injection sites is better than odd because of symmetry. Finally, after 6 injection sites increasing the number of injection sites does not increase the homogeneity or specificity of applied heat dosage.

A few assumptions were made that if relaxed might further improve hyperthermia. First, the study assumed each injection site had the same distribution width and heating intensity. In reality, these parameters are allowed to change based on different IONP fluid characteristics. Second, injecting IONPs in an asymmetric profile was not considered. Asymmetry might offer prospects of further improving hyperthermia.

The fifth study contributes to the field of hyperthermia by introducing the first theory quantifying the variability aggregation introduces to temperature. This theory has direct implications for experiments and hyperthermia doctors. First, the results provide a quantifiable manner of how aggregation will affect the temperature distribution inside tumors. From MRI the diameter of IONPs, or their aggregates, can be obtained in real-time. This study then determines based on the aggregate diameter whether aggregation will fail or not affect the hyperthermia treatment. A small amount of aggregation does not result in an unpredictable temperature profile. Below a critical aggregate diameter aggregation does not affect the system. However, a certain diameter the system will be dominated by aggregation variability. Before a hyperthermia treatment is started doctors should know this critical aggregate diameter.